Observational Methods for the Study of Debris Disks: Gemini Planet Imager and Herschel Space Observatory

by

Zachary Harrison Draper
B.Sc., University of Washington, 2012

A Thesis Submitted in Partial Fulfillment of the
Requirements for the Degree of

MASTER OF SCIENCE

in the Department of Physics and Astronomy

Observational Methods for the Study of Debris Disks: Gemini Planet Imager and Herschel Space Observatory

by

Zachary Harrison Draper
B.Sc., University of Washington, 2012

Supervisory Committee

Dr. B. Matthews, Co-Supervisor
(Department of Physics and Astronomy)

Dr. K. Venn, Co-Supervisor
(Department of Physics and Astronomy)

Dr. F. Herwig, Departmental Member
(Department of Physics and Astronomy)

Supervisory Committee

Dr. B. Matthews, Co-Supervisor
(Department of Physics and Astronomy)

Dr. K. Venn, Co-Supervisor
(Department of Physics and Astronomy)

Dr. F. Herwig, Departmental Member
(Department of Physics and Astronomy)

ABSTRACT

There are many observational methods for studying debris disks because of constraints imposed on observing their predominately infrared wavelength emission close to the host star. Two methods which are discussed here are ground-based high contrast imaging and space-based far-IR emission. The Gemini Planet Imager (GPI) is a high contrast near-IR instrument designed to directly image planets and debris disks around other stars by suppressing star light to bring out faint sources nearby. Because debris disks are intrinsically polarized, polarimetry offers a useful way to enhance the scattered light from them while suppressing the diffracted, unpolarized noise. I discuss the characterization of GPI's microlens point spread function (PSF) in polarization mode to try to improve the quality of the processed data cubes. I also develop an improved flux extraction method which takes advantage of an empirically derived high-resolution PSF for both spectral and polarization modes. To address the instrumental effects of flexure, which affect data quality, I develop methods to counteract the effect by using the science images themselves without having to take additional calibrations. By reducing the number of calibrations, the Gemini Planet Imager Exoplanet Survey (GPIES) can stand to gain ∼66 hours of additional on-sky time, which can lead to the discovery of more exoplanetary systems. The *Herschel Space Observatory* offers another method for observing debris disks which is ideally

suited to measure the peak dust emission in the far-IR. Through a careful analysis, we look at 100/160 μm excess emission around λ Boo stars, to differentiate whether the emission is from a debris disk or a bowshock with the interstellar medium. It has been proposed that the stars' unusual surface abundances are due to external accretion of gas from those sources. We find that the 3/8 stars observed are well resolved debris disks and the remaining 5/8 were inconsistent with bowshocks. To provide a causal explanation of the phenomenon based on what we now know of their debris disks, I explore Poynting-Robertson (PR) drag as a mechanism for secondary accretion via a debris disk. However, I find that the accretion rates are too low to cause the surface abundance anomaly. Further study into the debris disks in relation to stellar abundances and surfaces are required to rule out or explain the λ Boo phenomenon through external accretion.

Contents

List of Tables

List of Figures

Co-Authorship

The following are collaborators who contributed to the contents of this thesis not otherwise on my supervisory committee.

Christian Marois for example IDL code for reduction techniques of GPI data in Chapter 2.

Patrick Ingraham and Jean-Baptiste Ruffio for the derivation of GPI's high-resolution microlens PSF used in Chapter 2.

Schylur Wolff and Marshall Perrin for the derivations of the wavelength calibrations for GPI data cubes used in Chapter 2.

The GPI Team for work assembling and characterizing the instrument and data reduction pipeline.

Grant Kennedy and Bruce Sibthorpe for reduction of Herschel data and analysis of results in Chapter 3.

Herschel Instrumentation Teams and Support Crews for building, launching, and characterizing of the instrument.

ACKNOWLEDGEMENTS

I would like to thank:

Brenda Matthews for always being supportive of me in my various veins of research and for whom I would not be here otherwise.

Kim Venn for her ideas and help in expanding the λ Boo research.

Christian Marois for his help in understanding GPI data analysis and IDL code writing.

Grant Kennedy for his always quick and reliable help on Herschel data analysis.

Charli Sakari for reading and providing helpful comments on my thesis, as well as for finding the "that's what she said" and "taken out of context" lines.

Hannah Broekhoven-Fiene for providing incite on debris disk analysis with Herschel and for organizing the celebration (or commiseration) post-defense.

Trystyn Berg, Chelsea Spengler, Steve Mairs, and Mike Chen for being a friendly cohort outside of work in the face of the trials and tribulations that is UVic.

...

What's right is what's left if you do everything else wrong. - Robin Williams

For anyone who cares to read this.

Chapter 1

Introduction

First, you must create the Universe. Through various details, you arrive at a galaxy where baryonic matter is gravitationally bound and forms an environment adept at creating stars. In the life cycle of a star, the beginning state is for gas and dust within the Galaxy to condense predominately through gravitational collapse. Other mechanisms could rely on supernova shock fronts or magnetic coupling, but through whatever mechanism the proto-stars are condensed out of cold clouds of molecular gas and dust. Through the loss of angular momentum, gas and dust are accreted onto a growing core through a circumstellar disk. As fusion begins, the now stellar core begins to cease accretion and the star enters its Main Sequence (hydrogen-burning) lifetime. During this time the circumstellar disk undergoes a transitional state where photodissociation from the star evaporates the inner disk. The circumstellar environment begins to change rapidly during this time whereby most of the material is dissipated.

In the meantime, interesting things begin to happen within the disk itself. Dust begins to settle in the midplane of the disk and condense further into larger and larger grains. Through planet formation mechanisms (gravitational instability, magneto-resonate instability, turbulence, pebble accretion), which are not yet completely understood, the density in parts of the disk is rapidly increased to overcome the "1-meter problem"[1] (Dominik et al., 2007). Dense seeds from which the planets form are created in this transitional time period. As the inner hole grows in the disk, gaps are also

[1] A fundamental problem in planet formation. Small grains are bound by Van der Waal's forces, while large bodies are gravitationally bound. At 1 meter, collisions begin to overcome Van der Waal's bound clumps before gravity can effectively hold matter together to form massive bodies. Thus planet formation would cease at 1 meter if another mechanism didn't coagulate the dust before it breaks apart.

formed in the accretion disk farther out where gas giant planets sweep clear a path in the disk. This may be common around the frost lines where ice-compounds are able to condense from the gas onto dust grains. The once small seeds of condensed dust and ice congeal with surrounding matter until they reach a critical limit of 10 earth masses where run-away gas accretion forms massive planets, such as Jupiter and Saturn. Yet, not all of those seeds go on to form planets, but rather make up the dwarf planets, asteroids, and comets we see today.

1.1 Debris Disks

As the planets are formed, radiation pressure[2] and PR-drag[3] deplete the gas and dust until they are accreted onto the star or blown out on hyperbolic orbits, leaving planets and planetesimals (∼10-1000 km bodies) left over. On average this takes about ∼10 Myr for the planetary system to transition from a proto-star with an accretion disk to a system with a star, planets, and debris disks (Haisch et al., 2001; Hernández et al., 2007). As an example, the TW Hydrae Association, which is known to be ∼8 Myr old, has both protoplanetary and debris disks around its stars (Matthews et al., 2014). One of the defining characteristics of a star with a debris disk is that the fractional luminosity, defined as the luminosity of the disk divided by the luminosity of the star, is at least 100 times fainter than its equivalent protoplanetary system when nuclear fusion first began (Matthews et al., 2014). In the case of the solar system, the dust levels reach a fractional luminosity (f) of $\sim 10^{-7}$ for the Edgeworth-Kuiper Belt (EKB) (Vitense et al., 2012). The specific formation history plays a key role in the ultimate architecture of a specific planetary-disk system but generally there are hot, warm, and/or cold dust components. They are often interspersed with planets, whereby the dust is typically confined to a ring-like structure where it is dynamically stable from planetary interactions (see Figure 1.1). One of the principal methods for characterizing these systems is to measure the flux at a variety of wavelengths to look for an "excess" emission which is above the expected flux of the star (i.e. photospheric excess, see Figure 1.2). In fact, the first debris disks discoveries were via IR excesses from the InfraRed Astronomical Satellite (IRAS); these were the now famous Vega, β Pic, and Fomalhaut systems.

[2]Momentum imparted by photons from the star on dust grains.

[3]Poynting-Robertson Drag: Dust preferentially encountering radiation pressure in front of a dust grain's orbital path causes loss of orbital angular momentum.

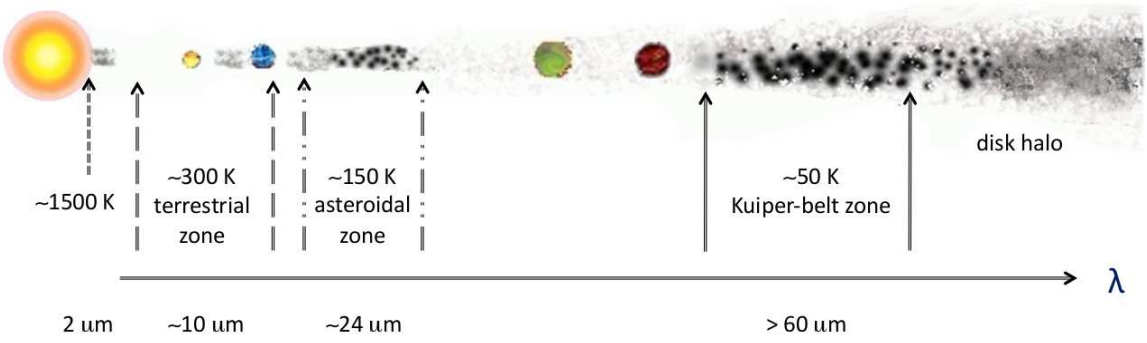

Figure 1.1 A schematic of a planetary/debris disk system. The range of temperatures for dust at different locations is given, interspersed with planets which clear gaps in the system. The result is often ring-like debris disks. On the bottom is the wavelength range of observations which are sensitive to that particular location of dust. They span from the near-IR, at 2 μm, to the far-IR and sub-mm at >60 μm. (Figure Credit K. Su)

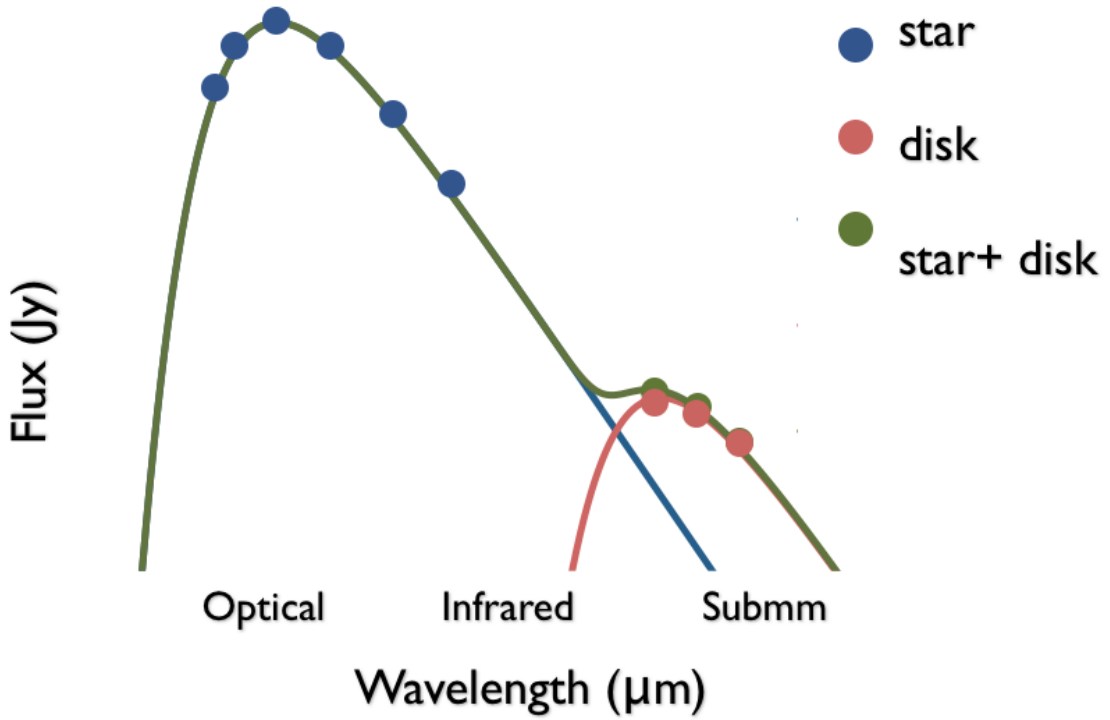

Figure 1.2 An example spectral energy distribution (SED) illustrating the range of wavelengths that can be observed and which contribute the most to the star versus the disk. The emission for the disk is commonly referred to as a photospheric excess, since it is above the expected SED of its host star. (Broekhoven-Fiene, 2012) (Figure Credit H. Broekhoven-Fiene)

1.1.1 Stirring

The same processes which clear out the protoplanetary disk, like PR drag and radiation pressure, will continue to deplete dust in a debris disk by as much as $f \propto t_{age}^{-1}$ (Wyatt et al., 2007b) in fractional luminosity. The continual creation of dust is therefore necessary to explain observations of debris disks around stars out to $\sim$1 Gyr or more in age. This is typically modeled as a collisional cascade where large bodies are continually ground down into smaller dust grains (Matthews et al., 2014).

In order to excite the debris disk, various stirring mechanisms are proposed to cause collisions which produce dust. Pre-stirring is applicable to young debris disks where turbulence from the protoplanetary phase leads to collisions. Delayed-stirring can occur via stellar flybys from neighbouring stars disrupting the disk. Also, the delayed formation of 1000 km sized planetesimals in the outer disk can cause self stirring at ages such as 100 Myrs. Planetary stirring from gas giants can also occur at later ages as they gradually, or suddenly, disrupt the disk. This is likely what happened with our solar system, where Jupiter and Saturn achieved a resonant orbit through inward migration and then rapidly migrate outward to disrupt the pre-EKB disk (Gomes et al., 2005).

1.1.2 Planets

There have been various studies done on the correlation of debris disks with exoplanets. Studies of protoplanetary disks have shown that disk mass and metallicity[4] should result in a positive correlation with disk luminosity and planets (Wyatt et al. (2007a), Bryden et al., in prep). Running counter to this are numerical simulations of planets and debris disks showing massive planets to be more likely to dynamically clear out debris resulting in an anti-correlation of debris disks and giant planets (Raymond et al., 2012). The formation of terrestrial mass planets and the presence of debris disks however was found to have a positive correlation. Observations have shown that high stellar metallicity is correlated with gas giant planets (Fischer & Valenti, 2005). There are now clear trends with far-IR excess emission and planet detections, which are predominately gas giant planets (See Figure 1.3). If you further break down the detections with *Herschel* by planetary mass, it's found that in those systems with only low mass planets ($< 30\ M_{\oplus}$), they are more likely to have debris

[4]Any element which is not H or He makes up roughly 1% of baryonic matter and is colloquially called a "metal" by astronomers.

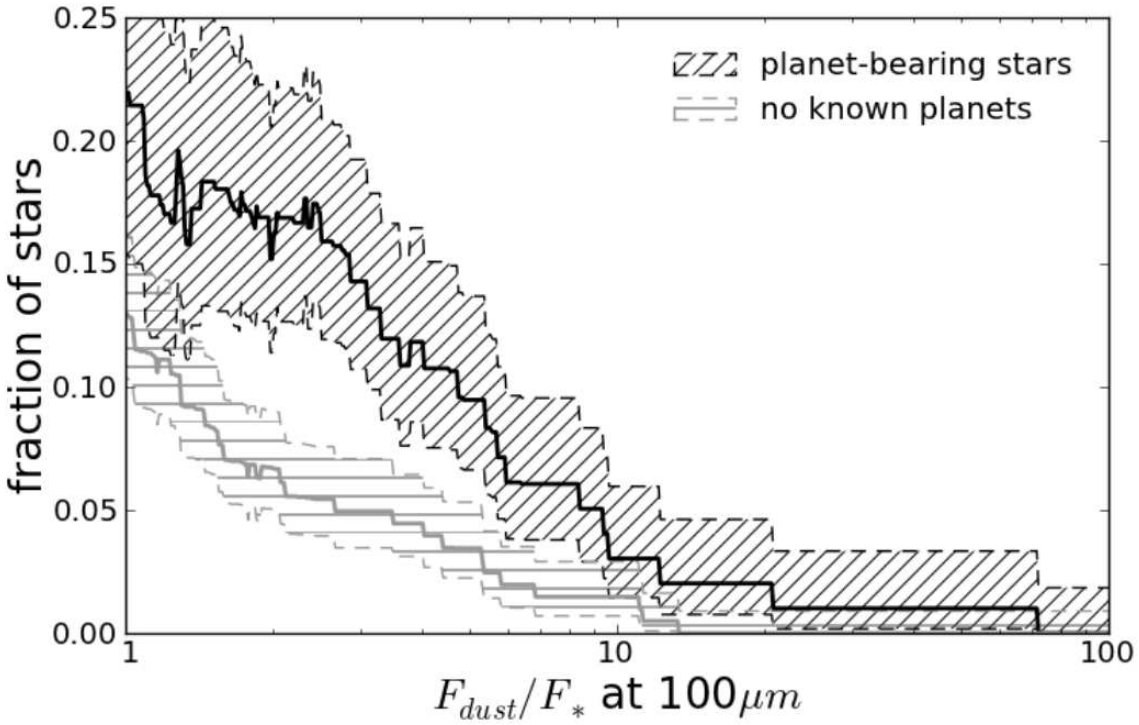

Figure 1.3 The fraction of stars vs 100 μm emission from debris disk stars. Top curve is stars with known planets, bottom is stars with no known planets. This illustrates a trend for higher levels of dust around stars hosting planets which suggests significant co-evolution (Matthews et al., 2014). (Figure Credit G. Bryden)

disks than higher mass systems (Marshall et al., 2014). It is still unclear if this is due to planetary stirring or the intrinsic prevalence of debris disks. It is therefore important to think about the planetary system as a whole with planets, debris disks, and star existing as a co-evolving system. Surveys such as the Gemini Planet Imager Exoplanet Survey (GPIES) will be important for putting observational constraints on these models as they will be able to directly image both planets and debris disks in a statistical manner from a larger overlapping sample size (see Chapter 2).

1.1.3 Metallicity

If there is a positive correlation with the presence of gas giants and stellar metallicity and an anti-correlation between gas giants and debris disks then one might expect to find a low stellar metallicity trend with debris disks. *Spitzer* IR surveys have yet to find such a trend (Greaves et al., 2006; Beichman et al., 2006). Furthermore, it may be that low metallicity protoplanetary disks don't form planetesimals as readily, which are needed to collisionally generate debris disks at later ages (Wyatt et al., 2007a). In this case, there may be a deficiency of disks around low metallicity stars (Maldonado et al., 2012). However, the λ Boo phenomenon discussed in Chapter 3 may be a special case where a debris disk versus stellar metallicity trend is due to post formation, secondary gas accretion rather than intrinsic stellar metallicity. Secondary accretion is a scenario where the metal deficiency of the star is not due to its primordial formation from a low metallicity ISM cloud, but is instead due to post-formation gas accretion from the debris disk. This again argues for planetary systems to be treated as co-evolved systems which can have causal links between the disks, planets, and star.

1.1.4 Gas

Typically debris disks are extremely depleted in gas because any material not locked up in large solid bodies does not survive the dissipative processes at the end of the protoplanetary disk phase. However there are a few exceptions. The stars 49 Ceti, HD 21997, and β Pic have been observed to have gas in their disks (Hughes et al. (2008),Moór et al. (2011),Dent et al. (2014)). 49 Ceti is thought to be too old (at $\sim$40 Myr) for the gas to be left over from the protoplanetary phase and must have been created recently from collisions of planetesimals within the debris disk (Zuckerman & Song, 2012). For 49 Ceti and HD 21997 it is also been suggested that the gas

production is recent given that emission from CO is found, since it should deplete within hundred year timescales due to photodissociation (Moór et al., 2011). In the case of β Pic the resolved imaging of a CO gas clumped in one region of the disk is highly suggestive of a recent large impact (Dent et al., 2014). It is therefore possible that gas can be produced and accreted onto a star at much later ages. The gas content in debris disks is not well constrained as there could still be up to 10 $M_{\oplus}$ of unobserved gas within debris disks which have been surveyed and not violate upper limits placed by observations (Hillenbrand et al., 2008). This is important when we look at λ Boo stars in Chapter 3, as secondary accretion from a debris disk will imprint a metal deficient abundance pattern with solar-level C, N, O and S in the stellar atmospheres (Venn & Lambert, 1990; Waters et al., 1992). This abundance pattern can distinguish an intrinsically metal poor star from one that has experienced secondary accretion.

1.2 Observational Methods

The study of debris disks offers unique challenges, which have led to a diverse set of observational methods to answer the scientific questions we have to pursue. In particular debris disk observations have required a full use of a photon's known parameters: 1) The amount of energy, which translates to the choice in observed wavelength to find excess dust and gas emission from the disk; 2) The polarization of the photon, which means the photon has a preferred orientation given scattering of light off of the dust grains within the disk; 3) As well as the photon's phase, which when used in interferometry has unmatched angular resolving power.

1.2.1 High Contrast Imaging

The primary goal of high contrast imaging is to suppress star light while trying to directly image faint objects nearby, such as planets and debris disks. The measure of contrast is the ratio of light from the central star to the background level around the star. The principal method is to directly block the star through the optics via a chronograph. A lyot-stop chronograph is one which has a spot in the centre with a ring around it in order to suppress diffraction rings caused by a finite aperture (see Figure 1.4). Similarly, apodizing[5] the lenses can reduce diffraction of light to create

[5]Decreasing the transparency as a function of radius from the centre of the lens optics.

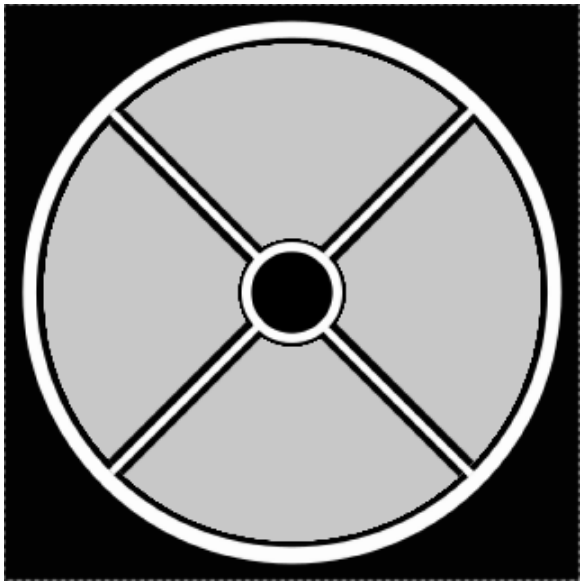

Figure 1.4 Image showing the simulated pupil of the Gemini Planet Imager (GPI): Chronograph is at the centre; arms matching Gemini-South Observatory's secondary mirror structural arms; and lyot stop around the edge are in black. The grey areas are where light is allowed to pass through. This is the first and primary way to suppress the star light to increase contrast in the image. (Savransky et al., 2013) (Figure Credit D. Savransky)

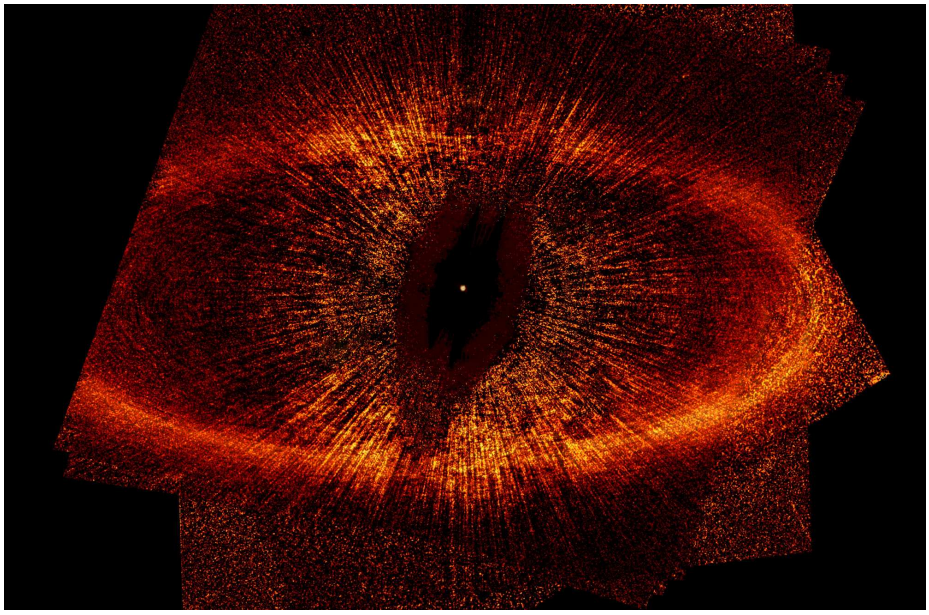

Figure 1.5 The debris disk around Fomalhaut imaged by *Hubble* after changing roll angle and PSF subtraction (Kalas et al., 2005). (Figure Credit P. Kalas)

a narrower PSF, or point spread function. The PSF is unique to every instrument and is a measure of how the light of a point source is dispersed by the optics. The size of the instrument's PSF is the primary limiting factor of resolution on an imaging instrument. In high contrast imaging the primary wavelength regime is in the optical/near-IR for space-based observations (*Hubble*, see Figure 1.5), or infrared for ground-based observations (GPI, SPHERE, NACO, HiCIAO). This is largely due to the limitations in current technology. We currently only have *Hubble* available with a chronograph in space, which operates in the optical regime. On the ground, adaptive optics technology to defeat the effects of atmospheric turbulence works best in the infrared.

Even carefully designed instruments will have a limit to the degree of magnitude contrast they can observe. We then rely on more advanced data reduction methods which increase the image contrast to detect faint sources. The primary methodology is to differentiate the signal from the noise source of the telescope's speckles and diffracted PSF shape on the field-of-view (FOV). The first method is to do PSF subtraction. In this method, a star, presumed to not have companions and of similar type to the target star, is observed under the same conditions and subtracted from the target to remove the stellar emission and leave behind the faint sources. This is

a common method which works for both debris disks and planets.

Other methods work well on point sources (i.e. planets) but not diffuse sources like debris disks. Angular differential imaging (ADI) is a technique in which multiple images are taken while the FOV rotates with parallactic angle from rising and setting of objects in the sky to leave a constant PSF but a moving astrophysical source (Marois et al., 2006). In space this can be done by changing the roll angle of the spacecraft. Subtracting the median of the images and stacking the results rotated for the angle shift removes star light and builds up signal from a planet. Spectral differential imaging (SDI) requires the use of an integral field spectrograph (IFS) to look at the change of light as a function of wavelength. Diffracted light of a star will expand radially within the field with increasing wavelength. The diffracted light can then be differentiated from the faint sources by a known scaling factor with wavelength. Since the faint planet signal will change position in the field with wavelength after scaling the PSF speckles to retain the same position, the faint sources can be separated from the noise (Marois et al., 2014). Furthermore, modeling the spectra of a planet can allow detecting trace signatures of a uniquely planetary spectrum on top of the stellar spectrum in the diffracted light (Marois et al., 2014). The result of this processing can be seen in Figure 1.6, where GPI observed β Pic and resolved the planet β Pic b while suppressing speckles.

Debris disks stand apart from stars and planets in that they are strongly polarized due to scattering off of the dust grains. Stars on the other hand are largely unpolarized because the emission from their surface results in a roughly equally dispersed range of polarization angles. Planets can be a source of polarized light as well but are often below current detection thresholds. Polarization differential imaging (PDI) is a method by which light is passed through a Wollaston prism which disperses the light based upon the orientation of the electric field vector of a photon. By changing the orientation of the Wollaston prism, the polarization of the source light can be determined (Perrin et al., 2014). The result is nulling of the central starlight and diffraction speckles while imaging the debris disk itself. An example of this can be seen in recent GPI data of HR 4796A in Figure 1.7.

All of these data reduction techniques rely on high quality datacubes which are the interpretation of the light on the detector. Therefore it is important to have an optimal flux extraction algorithm that can be trusted before executing these reduction steps. Stability of the stellar PSF is required for these reduction methods and is also dependent upon instrument flexure which can change during the observing sequence.

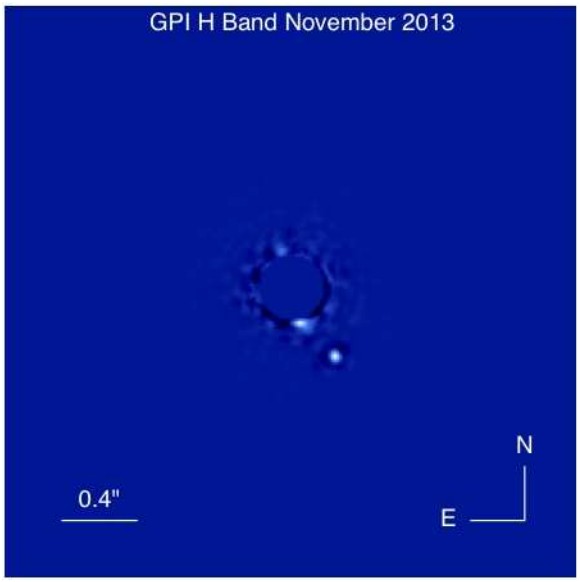

Figure 1.6 Directly imaged planet β Pic b with GPI after processing the data through ADI and SDI techniques. (Figure Credit C. Marois)

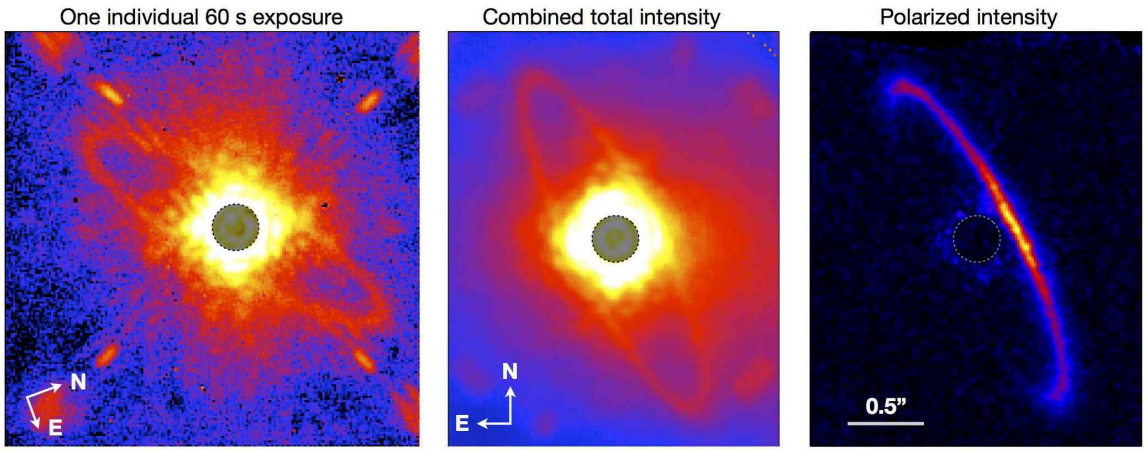

Figure 1.7 Directly imaged debris disk from the ground with GPI of HR 4796A from Perrin et al. (2014). A raw image is on the left. After processing several raw images, the total intensity of the disk can be seen in the centre. On the right is the polarized intensity image which results in higher contrast and speckle suppression to show the disk after PDI has been applied. (Figure Credit M. Perrin and M. Fitzgerald)

This is the primary motivation for the improvements to the data pipeline in Chapter 2.

Gemini Planet Imager Exoplanet Survey

The design motivation behind the instrument is to conduct a direct imaging survey for exoplanets and debris disks (Matthews et al., 2014). GPI will be able to image a new parameter space by having such high contrast in the near-IR within 0.1” to 1.4” around the target star. This instrumental improvement allows us to answer fundamental scientific questions into planet formation mechanisms. By directly imaging the planet, its composition and effective temperature can be directly measured. These measurements can’t be made with indirect planet detection methods such as transits and radial velocity. When this is applied to a large sample, the fundamental planet formation mechanisms can be differentiated from one another.

Planet formation mechanisms typically fall into two categories, “hot” start and “cold” start, which as the name suggests means planets can start out with different temperatures (Spiegel & Burrows, 2012). “Hot” star models are typically caused by disk instabilities where by the mass accretion rate is so fast that it is unable to dissipate heat efficiently. “Cold” start models, like core accretion, are where the

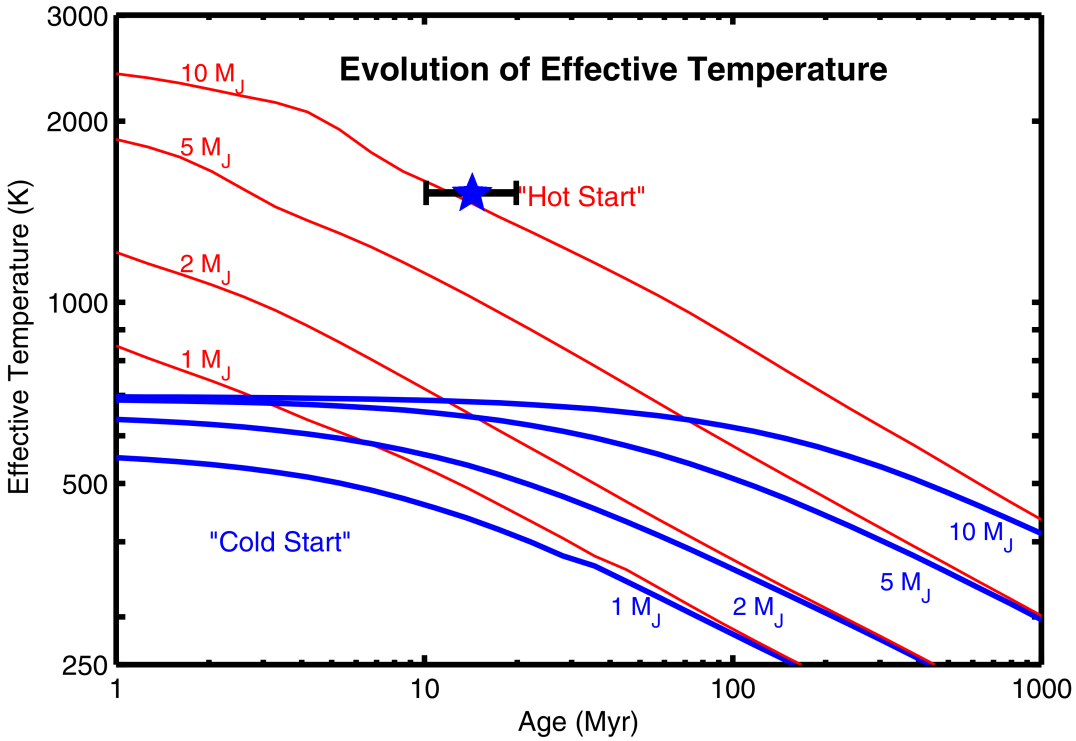

Figure 1.8 The figure above is from Figure 5 of Spiegel & Burrows (2012) showing example cooling tracks of a planet temperature with age ranging from 1 to 10 Jupiter masses (M_J). Red lines show "hot" star planets, blue lines show "cold" start planets. Observations of β Pic b are plotted on top of the model tracks as the blue star. It was found to have an effective temperature of 1650 ± 50 K and an age of 10-20 Myr (Chilcote et al., 2014). This puts β Pic b in the "hot" start regime.

mechanism of accretion is slower. Slower accretion rates allow heat to dissipate and leads to colder planets of similar mass to "hot" start models. If you compare the planet's temperature with the age of the star you can differentiate whether planets are formed from either mechanism. As an example you can see Figure 1.8 where GPI first light data shows β Pic b was likely formed through a "hot" start mechanism.

1.2.2 Far-IR/Sub-mm Emission

Since debris disks' peak emission is predominately in the Far-IR from 60 to 160 μm, this is the best wavelength region to search for "excess" emission. There is a recent lineage of IR/sub-mm instruments which have been sent to space to get above the atmosphere. Starting with *IRAS*, to *Infrared Space Observatory* (ISO), to *Spitzer*

Space Telescope (hereafter *Spitzer*), to *Akari*, to *Herschel Space Observatory* (hereafter *Herschel*) to the *Wide-field Infrared Survey Explorer* (WISE), from the 1980's to present. Other space based missions such as the *SPace telescope for Infrared Cosmology and Astronomy* (SPICA), are also planned to continue the observations which can only be achieved in space. The problem from the ground is that the atmosphere is not uniformly transparent to light of all wavelengths; instead, ground-based telescopes are limited to "atmospheric windows" where only some of the light penetrates the atmosphere. At some wavelengths, this necessitates observing from very high elevations and/or very dry sites (e.g. Mauna Kea, Atacama Desert). For example the earth's atmosphere is transparent to optical light, however most of the IR and sub-mm are opaque due to water vapor. While space missions allow access to other wavelengths, the downside of such facilities is that they often have lifetimes of just a few years because they run out of coolant to keep the detectors cold and are inaccessible to servicing. *Herschel's* Photodetecting Array Camera and Spectrometer (PACS) bolometers (a sensor which changes electrical resistance as a function of temperature) required cooling the instrument to a few tenths of a degree above absolute zero to be sensitive to the incident radiation.

In the future however, massive international projects such as the ground-based Atacama Large Millimetre/submillimetre Array (ALMA) will be a major contributor to the field of sub-mm astronomy because of its increased sensitivity and angular resolution from interferometry. In the sub-mm ($>200\mu$m), you also have ability to trace dust and gas within the same systems. Often continuum emission is measured to find blackbody radiation from dust content within disks. With spectrometers, measurements can also be made to detect molecular gas such as CO, HCN, and HCHO. Correlating the gas emission lines with dust continuum emission allows us to learn more about the evolution and kinematics of a system. Often gas and dust are spatially correlated but sometimes they originate from different regions. Based on the Doppler shift of the lines, 3-dimensional information can be gained by assuming Keplerian orbits (Dent et al., 2014). As an example see Figure 1.9, where the continuum and gas are both observed by ALMA. In this case, β Pic has gas emission which is asymmetric compared to the dust emission due to a recent collision of planetary bodies.

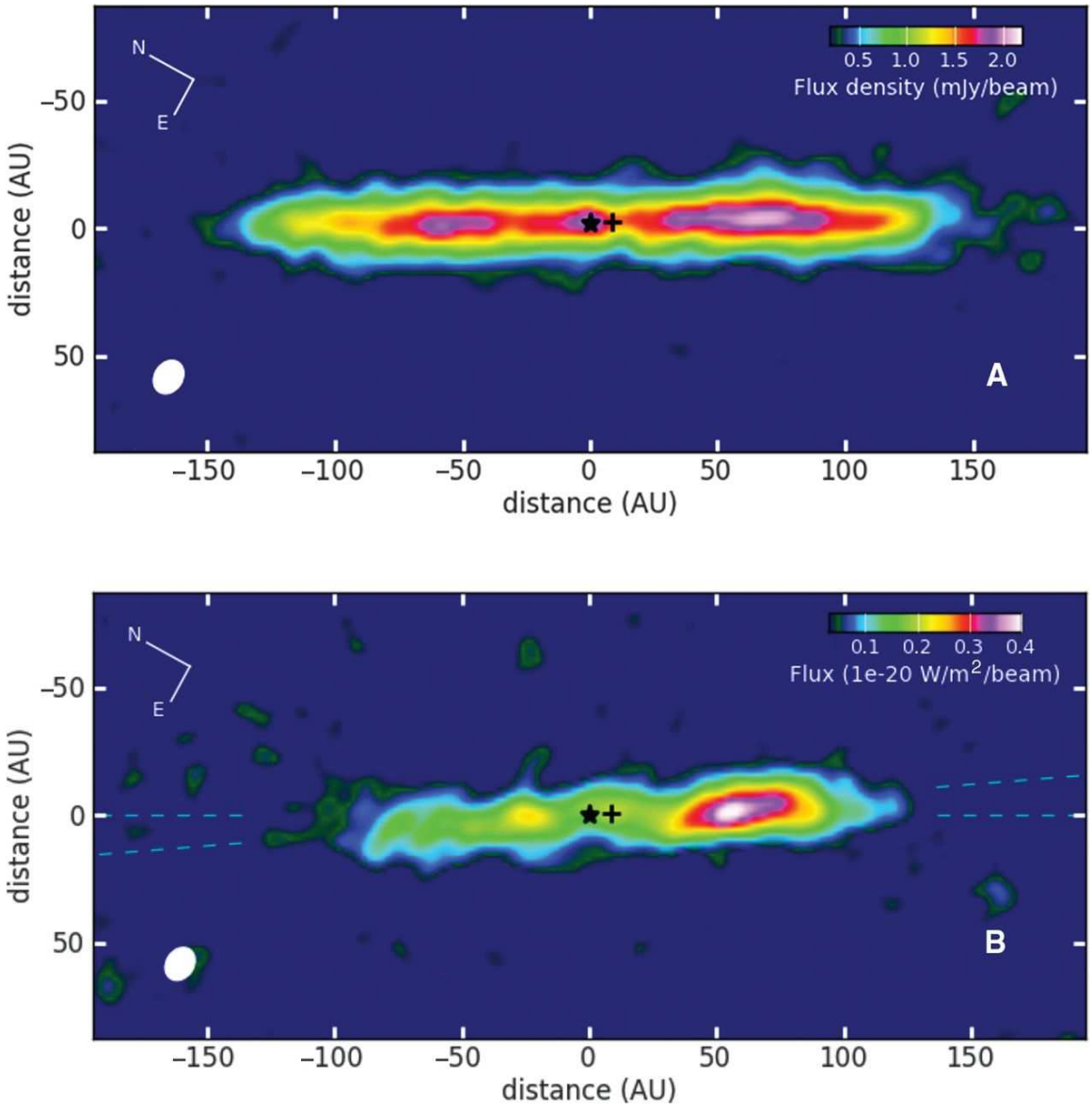

Figure 1.9 *Top:* Continuum emission of dust around β Pic. *Bottom:* CO emission line map. Both observations were taken by ALMA. There is a clear asymmetry in both where the high amount of gas is likely from a large, recent collision of planetary bodies in the debris disk. The black star denotes the location of the star, while the black cross represents the location of β Pic b at the time the system was observed based on astrometry from direct imaging. The dotted lines indicate the inclinations of the outer and inner disk. (Dent et al., 2014) (Figure Credit W. Dent)

1.3 Agenda

An outline of this thesis is as follows:

In Chapter 2: The Gemini Planet Imager: Improvements to the IFS Data Reduction, I discuss analysis and improvements into the GPI data reduction pipeline intended to improve the scientific impact of the GPI exoplanet survey. Current data reduction methods of the IFS do not provide the optimum the observable contrast and therefore reduce the discovery space of new exoplanetary systems. I also develop a software based approach to solve an engineering problem, where flexure in the instrument causes a shift in the incident light from where the data reduction pipeline expects.

In Chapter 3: Insights on the λ Boo Phenomenon Through *Herschel*, I analyze the *Herschel* observations of 8 λ Boo stars in order to gain insight into the mechanism which creates this class of stars. The Far-IR and sub-mm excess has been thought to be the cause of the unusual surface abundances through gas accretion. Analysis of the excesses reveals the emission is likely from a debris disk rather then an ISM bowshocks. Based upon this, PR-drag is investigated as a possible mechanism for gas delivery and found to be orders of magnitude inefficient at transporting volatiles from the debris disk to the star. Therefore, if the λ Boo phenomenon is caused by external accretion, some other mechanism must be used to cause the secondary accretion of gas.

In Chapter 4: Conclusions, I summarize the impact and results of the analysis in Chapters 2 and 3. Also, I explore the future questions to be answered from this work.

Table 1.1 Table of Jargon
List of acronyms, symbols, or terms that are commonly used throughout this work with their definitions.

Term/Symbol	Definition
$\oplus$	Units Relative to Earth
$\odot$	Units Relative to the Sun
μm	Micrometre or Micron
Akari	Japanese Infrared Satellite (ASTRO-F)
AU	Astronomical Unit
EKB	Edgeworth-Kuiper Belt
far-IR	Long wavelength end of the Infrared, (200μn$<\lambda<200\mu$n)
FWHM	Full-width half-maximum
GPI	Gemini Planet Imager
GPIES	Gemini Planet Imager Exoplanet Survey
HiCIAO	High Contrast Instrument for the Subaru next generation Adaptive Optics
HWHM	Half-width half-maximum
IDL	Interactive Data Language
IFS	Integral Field Spectrograph
ISM	Interstellar Medium
JCMT	James Clerk Maxwell Telescope
Jy	Jansky, Unit of Flux Density [10^{26} W s m^{-2}]
mJy	milli-Jansky
NACO	Nasmyth Adaptive Optics System (NAOS) + Near-Infrared Imager and Spectrograph (CONICA)
near-IR	Short wavelength end of the Infrared, (0.9μn$<\lambda<5\mu$n)
PACS	Photodetecting Array Camera and Spectrometer
PSF	Point Spread Function
SED	Spectral Energy Distribution
SPHERE	Spectro-Polarimetric High-contrast Exoplanet Research
Spitzer	NASA Spitzer Infrared Space Telescope
sub-mm	Submillimetre wavelength, ($>200\mu$n)
V-band	Johson-Cousins photometric band at 0.6 μn
WISE	Wide-field Infrared Survey Explorer
Y-band	Johson-Cousins photometric band at 1.05 μn

Chapter 2

The Gemini Planet Imager: Improvements to IFS Data Reduction.

The Gemini Planet Imager (GPI) is an extreme[1] adaptive optics instrument designed to image exoplanets, debris disks, and solar system objects in the NIR. The instrument is currently located on the Gemini South Observatory in Cerro Pachón. Following the commissioning of GPI, an exoplanet survey will be conducted of young nearby stars. The younger the star, the brighter the planet will be from gravitational contraction. The closer the star, the easier it is to resolve a planet. This instrument is a significant step forward because its angular resolution allows for a discovery space which is consistent with the typical locations of planets at ∼10s of AU. Previous direct imagers only imaged binary stars and "super-jupiters" because typical planets were too close or faint relative to the star to detect (Nielsen et al., 2013). It also is a step forward due to the IFS or integral field spectrograph which allows for the characterization of the exoplanet atmosphere to look for molecular bands such as CO_2 and Methane (Macintosh et al., 2014). By determining the rate of incidence of directly imaged planets it is possible to differentiate between cold start and hot start models of planet formation. Some models predict planets should be much brighter or dimmer as a function of age. Given a statistical sample large enough, one could

[1] AO systems are often characterized by Strehl ratio, from 0 to 1, as the ratio of observed PSF peak to the maximum achievable peak intensity for the telescope. Extreme-AO systems achieve a strehl ratio of ∼0.9 by directly observing a natural guide star, where as wide FOV laser guide star AO systems typically have much lower strehl.

validate either of the competing sets of planet formation models. Furthermore, the chemical composition of their atmospheres can lead to more accurate modeling of planets and how their composition varies with separation from the star.

The instrument is capable of closing the AO loop on Y-band ($\sim$0.9 μm) 9th magnitude targets under modest weather conditions and subsequently imaging a 2.7×2.7 arcsecond field of view (FOV) around the target. In most cases the target is a planetary and/or disk hosting star, but it is possible as well to image solar system objects such as Titan or Pallas. Under most conditions the central target is too bright to be imaged and requires a chronographic mask to block the light within 0.1 arcseconds in radius at the center of the FOV. The primary science subsystem is an integral field spectrograph which is based on a lenslet array design in order to disperse light into microspectra and polarization spots onto the detector. As shown in Figures 2.1 and 2.2, these dispersed light images are then analyzed by data reduction algorithms to interpret a datacube (Chilcote et al., 2012; Larkin et al., 2014).

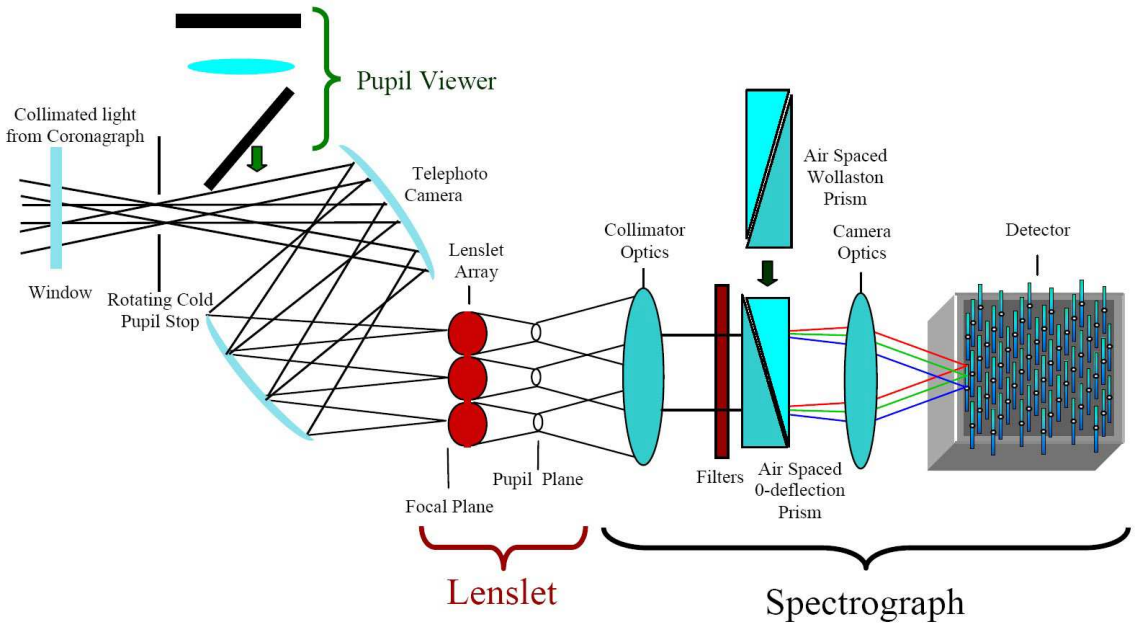

Figure 2.1 A schematic illustrating the light path in GPI's IFS. The light enters from the chronograph in the upper left and is folded and focused onto the lenslet array. The light from the lenslet array is collimated and passes through either the refracting prism or Wollaston prism depending on the observing mode. Y, J, H, K1 & K2 band filters can then be used to isolate specific wavelength ranges in both modes. The microspectra or spots are then collected on the hybrid-CMOS (Complementary Metal-Oxide-Semiconductor) detector (Chilcote et al., 2012; Larkin et al., 2014).

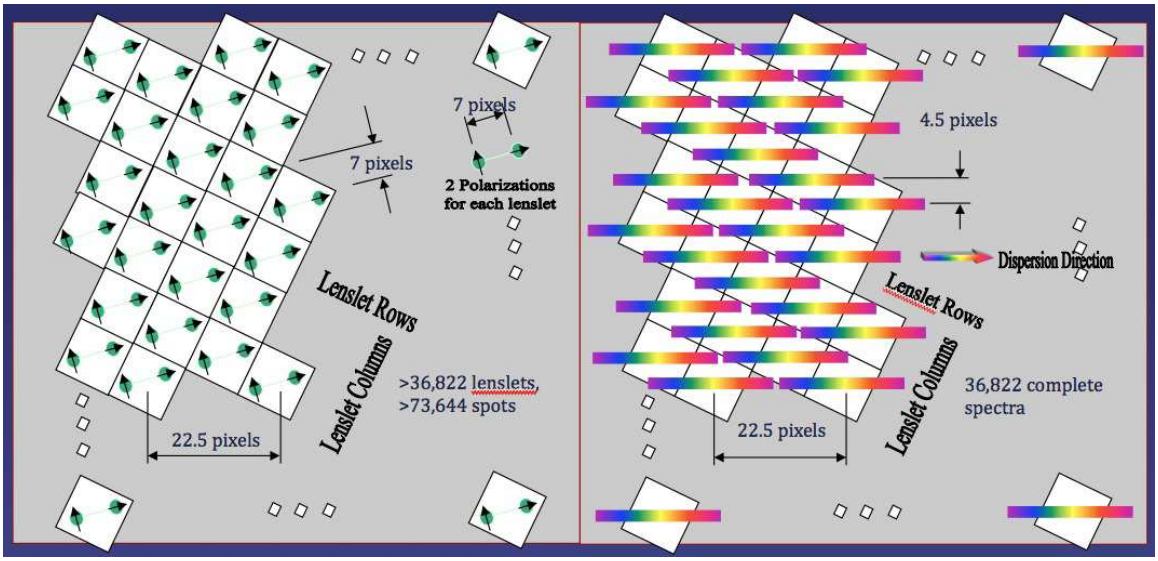

Figure 2.2 The light from the telescope is brought to a focus at the lenslet array. The light within a given microlenslet is then focused into a spot which can be dispersed by a Wollaston prism for polarization mode (left) or refracting prism for spectral mode (right) (Chilcote et al., 2012; Larkin et al., 2014).

The microspectra are critically sampled on the detector (except in the Y-band where they are undersampled due to its shorter wavelength) by the lenslet array and offer low resolution spectroscopy across the FOV, creating a datacube of images at varying wavelengths. The FWHM or line spread function of a single lenslet is $\sim$1.2 pixels (Ingraham et al., 2014b). An arc lamp is used to determine the location of these microspectra and establish the wavelength solution on the detector. In quicklook algorithms of the GPI pipeline, rectangular apertures are centred along the spectra and used to determine the flux (Perrin et al., 2014; Maire et al., 2010). Unfortunately, due to non-repeatable flexure in the instrument, the position of the microspectra may be offset from the expected position determined by the wavelength calibration taken at a different orientation during observations. This causes reduced signal-to-noise, inaccurate wavelength calibrations, and contamination of flux into neighbouring lenslets.

The GPI data reduction pipeline currently uses a rectangular aperture method which is not an optimal estimator of the flux, because it does not weight the signal in each pixel correctly. The rectangle method also introduces systematic noise effects where a "checkerboard" pattern within cube slices appears. This is attributed to the fact that, due to the regular spacing of the lenslet array, the spectra may fall in either the centre or at the edge of a pixel while the extraction is centred only on whole pixels. This creates an aliasing effect, or an alternating pattern of increased and decreased flux between lenslets of the data cube. In addition, bad pixels can lead to pixelization in the data cube at different slices which then requires interpolation across wavelength.

An additional noise source is induced by vibrations from the cyrocoolers, which are noticeable in short exposures as a standing wave pattern in the detector (see Figure 2.3). This noise contamination on the detector is referred to as microphonic noise (at 60 Hz and harmonics) and can be reasonably modeled and decorrelated with the least squares approach to provide a more accurate datacube extraction.

To resolve these issues a more sophisticated approach of PSF extraction is needed both to optimally extract the flux from the detector and to adjust for flexure between the wavelength calibration and the science images. High-resolution PSFs are generated using the Anderson and King method which uses under-sampled point sources in combination (Anderson & King, 2000; Ingraham et al., 2014b). The wavelength calibrations are used as a starting point, but additional offsets to account for the flexure induced since the calibration was made can be added (Wolff et al., 2014). The

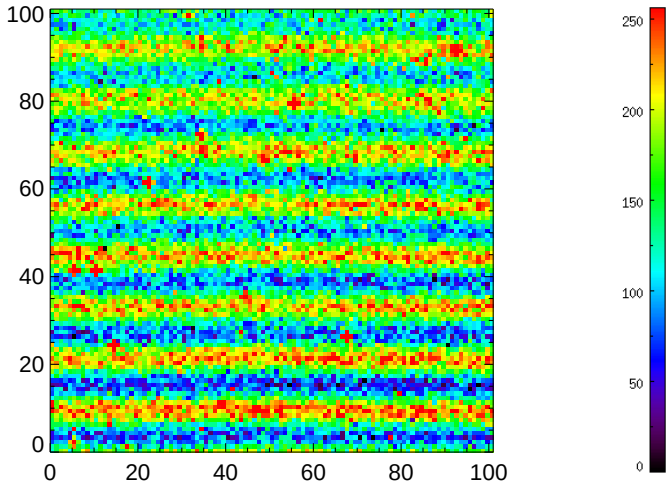

Figure 2.3 Sub-section of the detector taken from a dark exposure showing the standing wave pattern induced by the vibrations in GPI. The x-y axes are in pixels and the image is linearly scaled to minimum and maximum values to enhance the wave pattern. This constitutes a noise contribution which can be modeled and removed during the extraction process.

flux is then extracted using an inversion method to measure flux as a function of wavelength and minimize contamination from neighbouring spectra and noise sources (outlined in Section 2.2). The flexure offset is found either through an iterative solver or a modeling and cross-correlation routine (outlined in Section 2.3).

2.1 Analysis of Lenslet PSF and Polarization Mode Distortions

In order to use PSF fitting to optimally extract the flux from the detector we must first know the PSF of the lenslets. What makes this problem difficult is that the microlenslet PSF is critically sampled which means its shape is indeterminate with centering position. In order for a PSF shape to be known, it must be resolved by multiple pixels to interpret its precise subpixel location. Through statistical treatment of individual PSFs, with different sub-pixel centring, we can reveal the true PSF. I therefore strive to analyze the properties of the polarization mode spots to create a library of PSFs to use in extraction of both polarization mode and spectral mode. Each 'spot' is the illumination of the detector through a single lenslet and should theoretically represent the microlenslet PSF.

The image used for this test was a flat-field taken on December 12th, 2012 with the telescope simulator at Santa Cruz. The incident light is made spatially uniform in brightness via an integrating sphere and depolarized before entering GPI's pupil. The data were extracted to an IDL formatted variable via GPItv[2]. No dark subtraction or flat fielding was performed on the image as reduction steps. Darks are a minor improvement due to the high signal-to-noise. Flat fielding of the detector is not available (at the time of this study) and relies on the method of spot extraction being tested here. Some of the flat fielding from large scale diffuse light will be removed in the PSF fitting process shown here, which is more traditionally done at the detector.

[2]Viewing tool for GPI data

2.1.1 Spots Analysis

PSF Comparison

The image is read into IDL along with a catalog of points where the spots are located (see Figure 2.4). The spot coordinates were determined by running FIND, a star finding routine in the NASA's IDL Astronomy Users' library. Manual adjustment was made in DS9 to add/remove spurious detections. We ignored spots within 10 pixels of the edge of the detector. Each spot is checked again by running the CNTRD routine to refine the initial coordinates. CNTRD looks for peaks within an extended box of 3 pixels from the FWHM of the initial peak. This step may be unnecessary given a better coordinate map.

From the refined coordinates, a 7x7 pixel section is centred on the spot coordinates and fit with the MPFIT2DPEAKS routine. Since peaks were typically ∼7.5 pixels apart, a 7x7 grid was sufficient to extract a single spot. The original image is copied and then continually modified by subtracting the model from the data, for each peak on the detector, to generate a residual.

MPFIT2DPEAKS offers Gaussian, Moffat, and Lorentzian fitting options. For reference, the equations and their parameters are seen below. The rotational parameter was added with the keyword '/tilt' to adjust for distorted PSFs. It can also compute the residual sum of squares (RSS) value of the model to the data. Each of these profiles is tested for the best fit in this study.

Gaussian:

$$F(x,y) = F_o + Ae^{-0.5*u} \tag{2.1}$$

Lorentzian:

$$F(x,y) = F_o + A/(u+1) \tag{2.2}$$

Moffat:

$$F(x,y) = F_o + A/(u+1)^{\beta} \tag{2.3}$$

Common Functions:

$$u(x,y) = \left(\frac{(R_x - x_c)}{\sigma_x}\right)^2 + \left(\frac{(R_y - y_c)}{\sigma_y}\right)^2 \tag{2.4}$$

$$R_x = x\cos(\theta) - y\sin(\theta) \tag{2.5}$$

$$R_x = x\sin(\theta) + y\cos(\theta) \tag{2.6}$$

The constant offset parameter, F_0, in this case represents the large scale flat field variations from diffuse noise. The centroid's amplitude is given by A. The centroid's coordinates are given by x_c and y_c. The rotational parameter is θ, which modifies the rotated frame x and y to R_x and R_y. The σ_x and σ_y parameters are either the square root of the Gaussian variance or the half-width half-max for the Moffat and Lorentzian. The Moffat exponent, β, modifies the slope of the 'wings' of a Lorentzian profile. The flux of the spot would be given as the integral of the fitted function over the bounded xy coordinates.

2D Parameter Images

The fitting parameters for each individual spot are compiled. They include the centroid (x,y) position, peak value, the half-width half-maximum (HWHM) of the major and minor axis, a constant level offset, and rotation angle. In the case of a Moffat profile, β is also included.

All images were processed in a similar way by converting xy-detector positions to lenslet coordinates. Since the microlens grid is rotated by $\sim$22.5° with respect to the detector, the images are as they would look in the focal plane of the microlenslet array. Imaging in this reference frame minimizes blurring from interpolating rotated pixels. The conversion is not trivial and involves a scanning routine that starts at an edge and picks out spots in a row or column, hopping over bad lenslets if necessary. The routine accounted for the non-linear, pincushion distortion of the spots by making step-adjusted linear hops at each point.

The eccentricity was calculated with the HWHM parameters (σ_x, σ_y) following the standard equation below.

$$e = \sqrt{1 - \frac{F_1^2}{F_2^2}} \tag{2.7}$$

where F_1 and F_2 are the semi-major and semi-minor axes respectively. The determination for which of the model parameters is the right axis is determined by the ratio being less than 1. Essentially, the major axis is determined according to whether $F_1 > F_2$.

The rotational parameter is converted from radians to degrees. The model fitting only has orientations from $0 - 180°$, since an inverted ellipse from $180 - 360°$ is the same as $0 - 180°$ with the minor and major axes swapped. The function fitting doesn't have a standard way of keeping the rotational parameter fixed to the semi-major or minor axis, but it can be subsequently determined after the fitting by finding which axis is larger and adjusting for proper rotation.

2.1.2 Results of PSF Fits

PSF Comparison

For brevity, a 500x500 section of the image is used to test a residual map. Typically this takes 5 minutes on a single processor. Extrapolating to a full image would take approximately 80 minutes. Code parallelizing or using a template PSF fit will prove to be useful at this step in future development for data reduction at the observatory or massive re-analyses of archived data.

The resulting statistics run on the residual images can be seen in Table 2.1. On a spot-by-spot basis, the Moffat profile was better than a Gaussian for 58% of the 7x7 grids based on a lower RSS value (See Equation 2.8 where D is the data and F is the model function). A residual image of the initial and post-Moffat spot removal can be seen in Figures 2.4 and 2.5. The Lorentzian had the worst residual standard deviation and won't be considered further.

$$RSS = \sum (D(x, y) - F(x, y))^2 \tag{2.8}$$

Stat	Original	Gaussian	Moffat	Lorentzian
Mean	796.41	65.99	65.72	63.66
Median	110.00	5.66	9.62	67.00
Std. Dev.	1885.07	538.74	538.31	591.14
RSS	N/A	7.394×10^{10}	7.382×10^{10}	8.873×10^{10}

Table 2.1 Statistics on the sub-sectioned images of the detector before and after extraction. Units are in detector counts. The Lorentzian is much worse given the high median value. Ideally the counts post-processing should be near zero with a low standard deviation and low RSS.

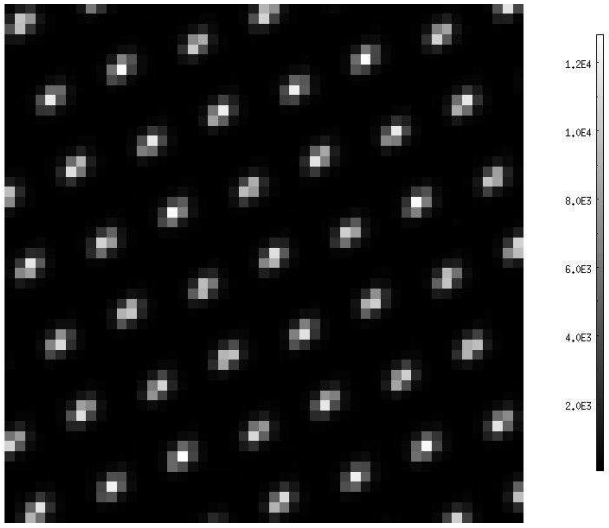

Figure 2.4 51x51 pixel sub-section of the detector in its original state. Units are in detector counts. The 'spots' can be seen with high signal and poorly sampled pixelation.

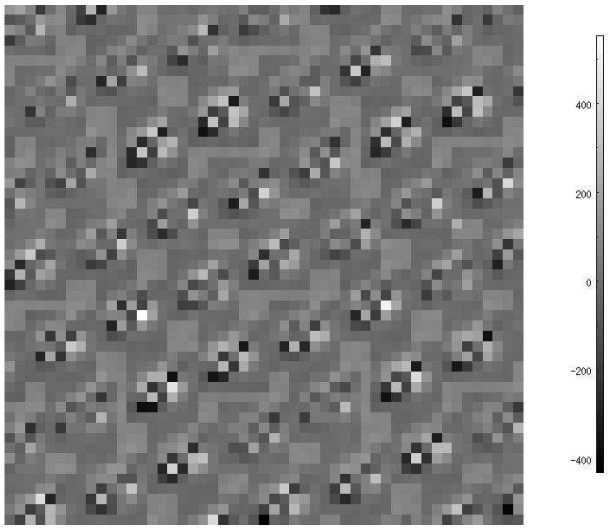

Figure 2.5 Same region as Figure 2.4 with spot subtraction using a Moffat profile. Units are in detector counts. Residual structure from the spots is still apparent but the residual intensity is consistent with the background noise. The structure left over is aligned with the chromatic dispersion inherent to the polarization mode of GPI.

Stat	Original	Gaussian	Moffat
Mean	860.045	24.67	24.21
Median	131.500	-6.50	2.88
Std. Dev.	2078.43	243.14	238.19
RSS	N/A	2.505×10^{11}	2.403×10^{11}

Table 2.2 Statistics on the full image before and after extraction. Units are in detector counts.

Full Image Residuals

The full residual image was made for the Gaussian and Moffat profiles since they were the most closely matched fits to the microlens PSF. The statistics of the full image residuals can be seen in Table 2.2. The Moffat profile extracts a slightly better result than the Gaussian due to a lower absolute mean, median, and standard deviation. Given a Moffat profile has 7 free parameters versus 6 in a Gaussian fit, it is not clear if this is significant result or an inevitable effect from more degrees of freedom. The number of fits where a Moffat profile is preferred over a Gaussian increases to 70 % based on a lower residual sum of squares.

The overall offset parameter produces a rough microlens flat fielded image which shows the light reflection commonly referred to as the curvy-w, upside down seagull, or "mustache" seen in Figure 2.6. Technically it is called an optical caustic. This is caused by a misalignment of the optical axis of GPI's AO system with respect to the IFS when it is flood illuminated by the telescope simulator. The result of the eccentricity parameter can be seen in Figure 2.7. The eccentricity traces the chromatic dispersion in the spots which increases towards the edges. The spots are mostly monochromatic in a central blue valley. The rotational angle can be seen in Figure 2.8. It is radially symmetric such that the spots are dispersed in a radial direction centred slightly off axis, to the upper left, of the detector. The Moffat exponent has some structure on the image suggesting it is accounting for some distortion across the detector. Overall, the Moffat exponent (see Figure 2.9) has a median value of 9.8 but grows rapidly towards the edges. You can also see the ghostly edges of the "mustache" feature from the level offset image of Figure 2.6.

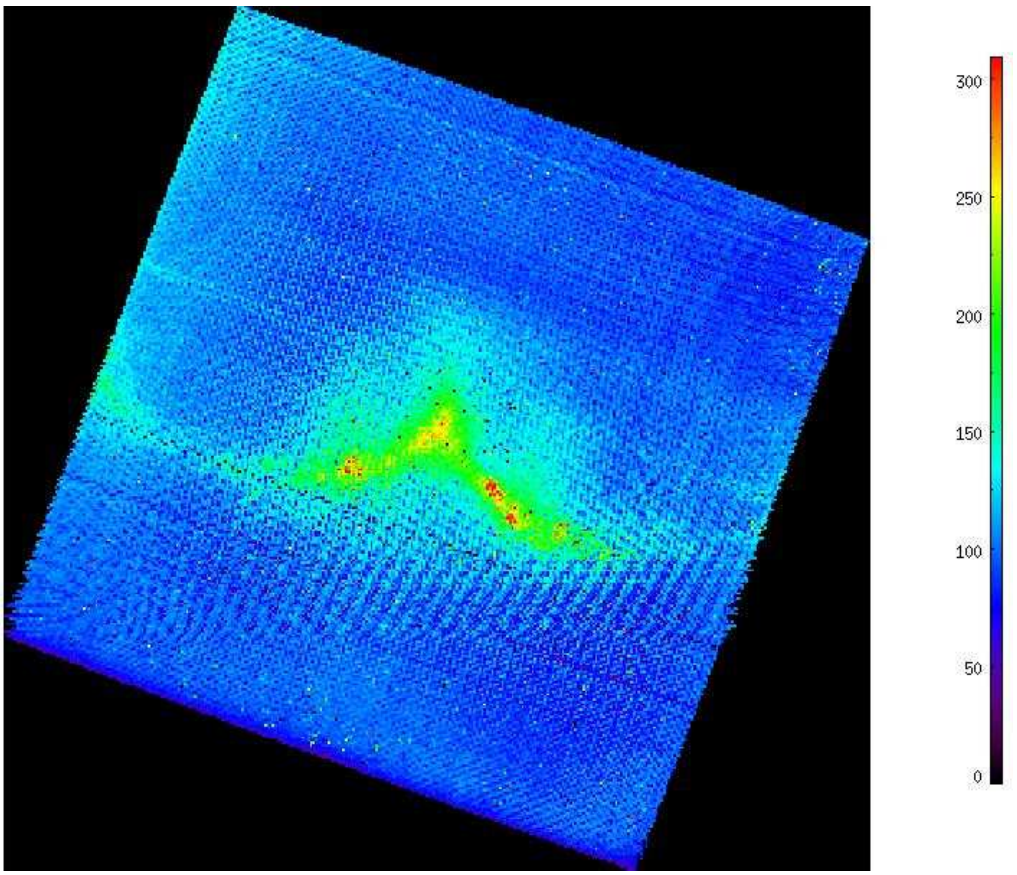

Figure 2.6 The overall offset constant, F_0, from the fits gives the background "mustache" feature from stray light. The image is now in the reference frame of the mircolenslet array, where each pixel is the parameter determined by fitting the pol-spot. This is equivalent to a flat field image in lenslet space.

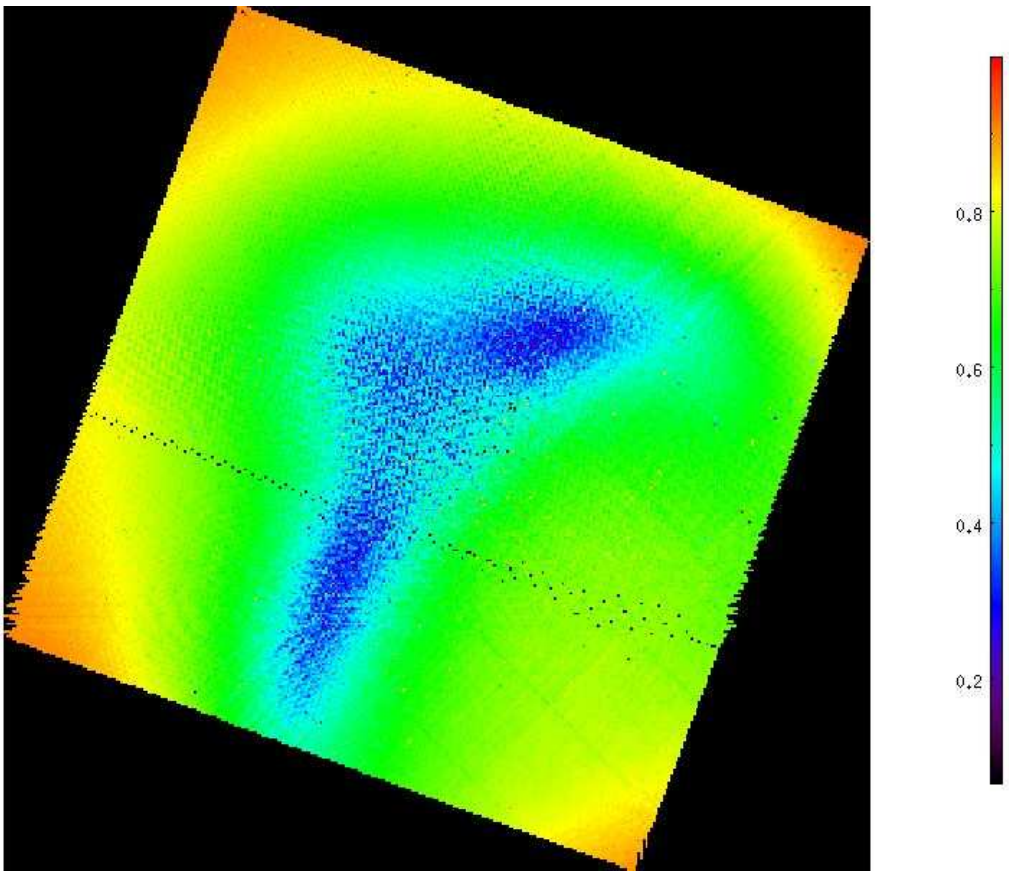

Figure 2.7 The eccentricity parameter, e, from a Moffat fit in microlens coordinates. It spans nearly the full range of 0 to 1 with more eccentricity at the edges. The image is in the lenslet array reference frame.

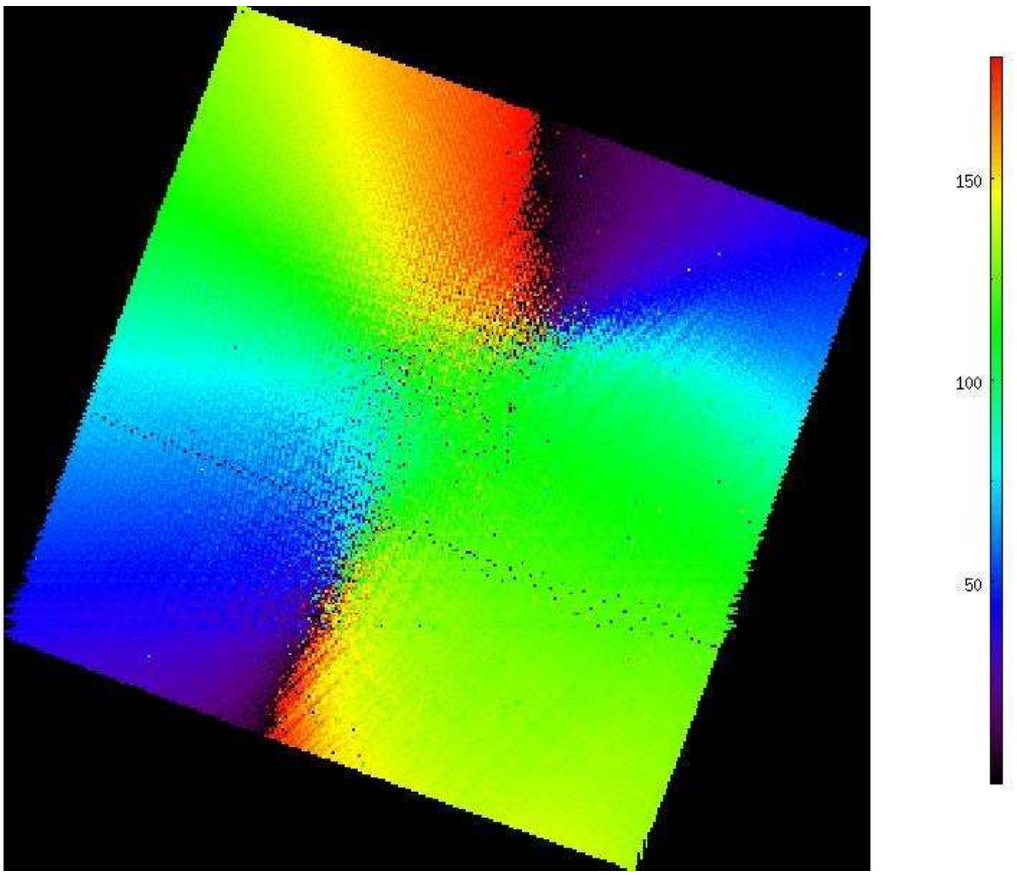

Figure 2.8 The rotational angle, θ, of a Moffat fit in micro-lens coordinates. The full rotation of 0-360° can still be seen as it crosses the 4 quadrants. The image is in the lenslet array reference frame.

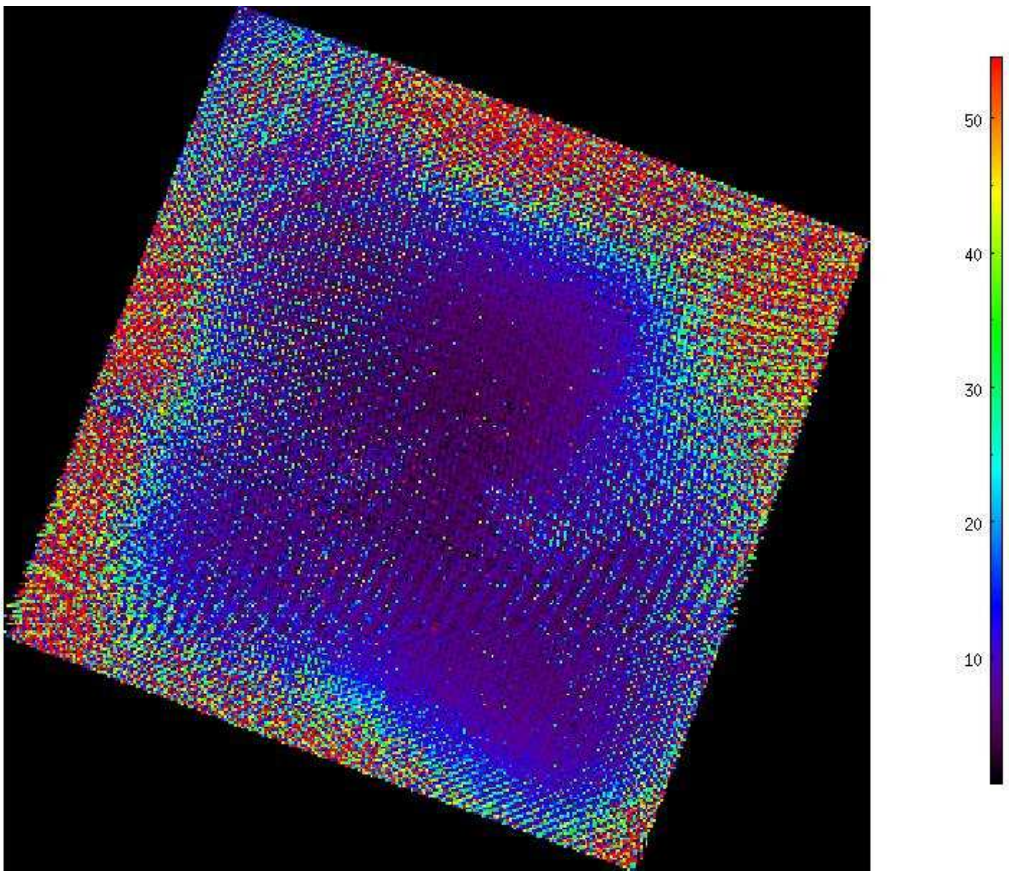

Figure 2.9 Moffat parameter, β, in micro-lens coordinates. The parameter is mostly small and uniform in the centre but larger towards the SW and NE corners in particular. It appears to be strongly correlated with the chess board pattern from subpixel positioning. The parameter appears to have a saddle-like structure. The image is in the lenslet array reference frame.

2.1.3 Template PSF

A template PSF can be generated by using the Moffat parameters as estimates for the profile shape within the detector. Using a weighted scoring function several spots can be combined by median or weighted mean to generate a template PSF which can be used to fit a spot on a science image, after being generated from a flat-field image. The score (S) is then computed such that subpixel position (x_{sub} = the modulous of x_c to 1), eccentricity, rotational angle, and Moffat exponent differences are weighted by a constant:

$$S = Ax_{sub} + By_{sub} + Ce + D\frac{\theta}{180} + E\beta \tag{2.9}$$

The minimum S values correspond to other spots which closely resemble the test spot. Then a selected number of spots with the lowest S value were combined to create a template PSF which could be used to fit any spot like it on another image. As a comparison, the Moffat profile is individually fit and compared with the residual of using a template PSF.

It was found that the median was the best way to combine the images (compared to a weighted average) by comparing the lowest residual. Also the C and D coefficients need to be a factor of 2-4 higher than the subpixel position suggesting the chromatic dispersion is a dominant contibutor to the PSF compared to the subpixel positioning. While the residual of the individual fit is comparable to the template PSF, it is not improving the quality of extraction since it never creates a lower standard deviation residual than individual fitting. A maximum of 30 spots can be used before the increased dispersion in parameters exceeds the benefit of combining spots. By combining spots the hope is to limit the effects of pixel-to-pixel response. Structure in large spikes in the centre of the spots can still be seen. The distribution of subpixel positions also shows a distinct bias in the y-axis, such that they cannot be used as a library for spectral mode PSFs, which can have any subpixel position. This is due to the fact that spectral mode has light dispersed over many pixels while the polarization mode has fixed intervals where spots are located.

2.1.4 Results of PSF Function Comparison

The Moffat profile is a better fit for the PSF modeling but it does not provide a drastic improvement as residual structure is still present. Ultimately, this means the resolution of the PSF is more constraining than the noise in the detector. Also the true microlens PSF is the deconvolution of the spots with spectropolarimetry which is non-uniform in the FOV. What is more intriguing is the structure of the parameters on the detector. The PSFs are so unique that very few can be simultaneously combined to improve the accuracy of the PSF. Other techniques will have to be considered for determining the PSF such as narrow band dispersed spectra. In that case, the light will be distributed over more subpixel positions to interpret the high resolution PSF. Polarization mode extraction would be aided by either having lenslet dependent micro-PSFs or treating them as spectra rather than spots, to minimize sensitivity variations across the FOV.

2.1.5 Probability Distributions of Model PSFs

To be more statistically robust in determining whether the microlenslet PSF is Gaussian or Moffat, I employed various statistical tests. Using the RSS as a test statistic, the goodness of fit with a model PSF (F) was tested for Moffat, Gaussian, and Lorentzian to the data (D) on all spots within the image (see Equation 2.8). The distributions correspond to the probability that each model fits the PSF and the degree of fit that was achieved.

A reasonable cutoff in RSS (to separate an hypothesis acceptance and rejection region) between the Moffat and Lorentzian profiles can be seen around 2 to 4 in Figure 2.10. Since it follows that the lowest residual is likely the best fit model, the region below the cutoff is the acceptance region and that above is the rejection region.

$$\alpha = \int_{t_{cut}}^{\infty} \mathrm{PDF}_{\mathrm{moffat}} \mathrm{dRSS} \tag{2.10}$$

$$1 - \beta = \int_{t_{cut}}^{\infty} \mathrm{PDF}_{\mathrm{lorentzian}} \mathrm{dRSS} \tag{2.11}$$

The following establishes the null hypothesis that the Moffat profile is the cor-

rect PSF, where α is the probability of a Type-I error, or false rejection of the null hypothesis, and β is the probability of a Type-II error, or false acceptance of the null hypothesis. When α and β are small the null hypothesis is given more credence. Plotted as a cumulative distribution (Figure 2.10), the discrete data can be simplified for reading off the above integrals. For an $\alpha = 0.05$ (95 % confidence interval of the null hypothesis), the t_{cut} is 2.5 RSS. The corresponding β for 2.5 RSS from the cumulative distribution of the Lorentzian is 0.001%. Therefore, for a random spot on the detector given various distortions to the PSF, it is more likely to be modeled by a Moffat than a Lorentzian with high confidence.

If this is repeated for a Gaussian instead of a Lorentzian, the results are less definitive. The same confidence for accepting the Moffat profile (95%) will give a $\beta = 93$ %. The distributions are so well matched that to accept one model and reject the other with any confidence will likely be a false acceptance; that is to say they are nearly equally probable as an appropriate PSF model. It may also be the case that the test

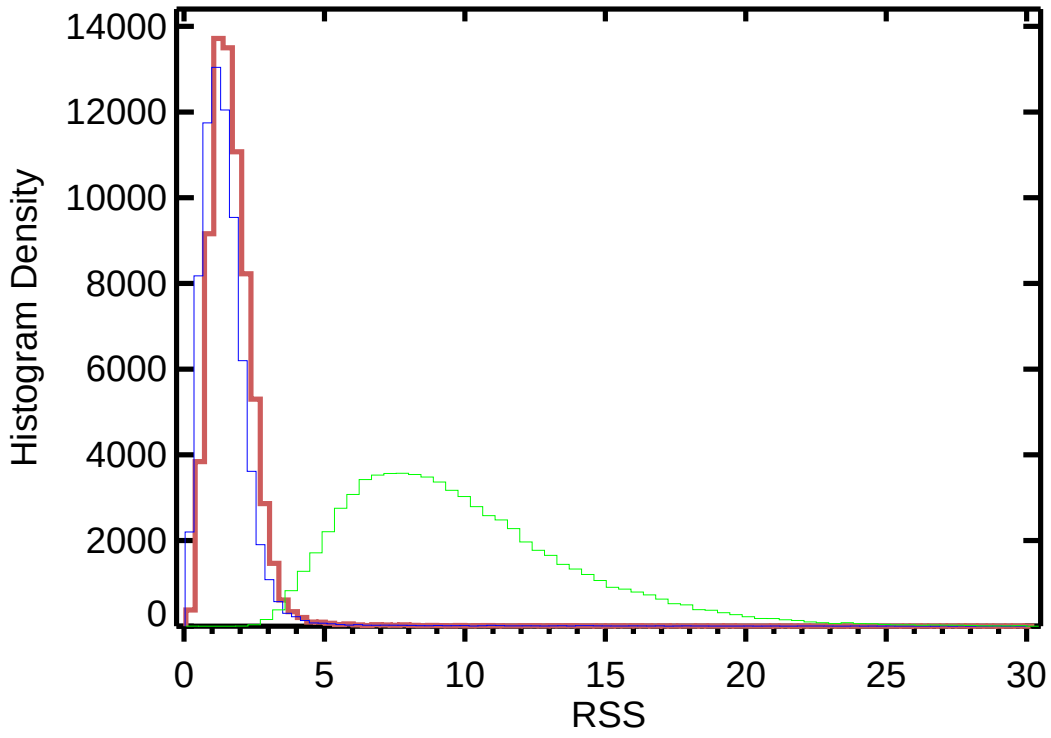

Figure 2.10 Histogram plot of PSF RSS for the model fits, Moffat (blue), Gaussian (red), and Lorentzian (green).

statistic is not capable of differentiating the models.

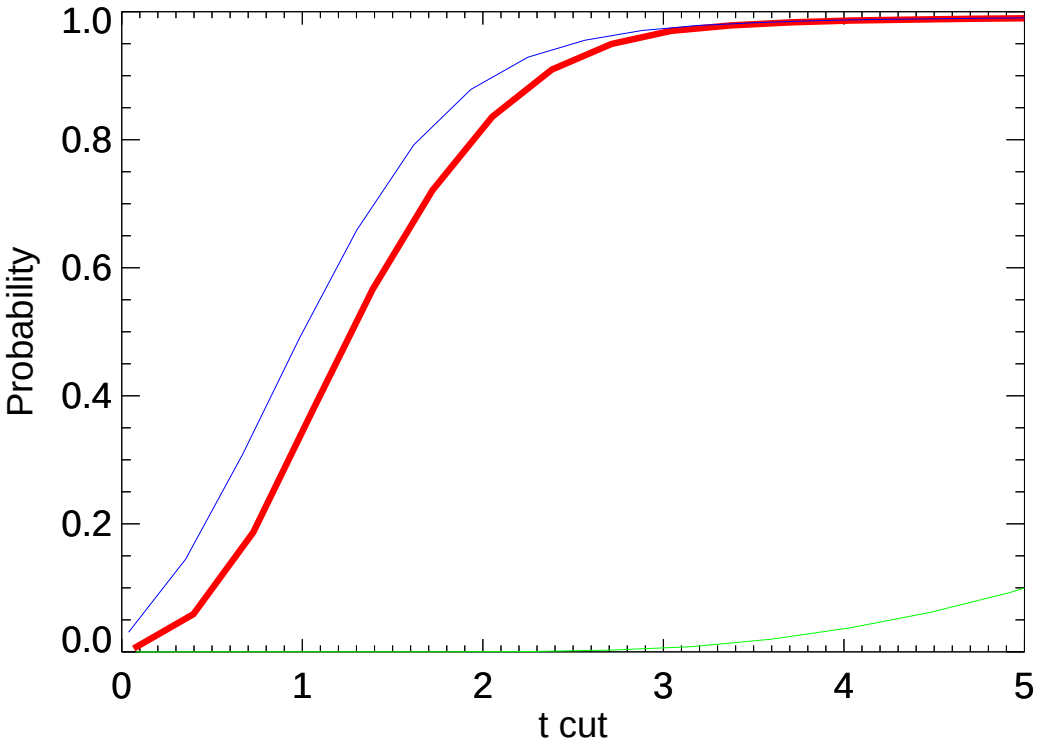

Figure 2.11 Cumulative distribution plot of PSF RSS for the model fits, Moffat (blue), Gaussian (red), and Lorentzian (green). The binned data from the cumulative distribution is used to make discrete integral as a function of the change in RSS.

2.1.6 Kolmogov-Smirnoff (KS) Test

The KS test is a way to determine if two cumulative distributions are significantly different (Conover, 1980). Applying the test to the Gaussian and Moffat profiles give a null result that shows the two profiles cannot be differentiated as separate distributions with any significant confidence.

$$KS_{crit} = Sup\big(RSS_{\text{moff}} - RSS_{\text{gaus}}\big) \tag{2.12}$$

Essentially, the maximum value between the two cumulative distributions is com-

pared to a KS distribution table of a given sample size to test its significance. In this case, the KS statistic was 0.037 with a > 0.99, p-value meaning there is no significantly different underlying distribution. A p-value of 0.05 would indicate a 95 % confidence that the underlying distributions are the same. If they were, it would give credence to one PSF providing a better fit than the other. This result supports the idea they are essentially equivalent at getting a maximal extraction of the PSF.

2.1.7 F-Test

Since the Lorentzian and Moffat functions are nested, an F-test can be applied to determine if an additional parameter can produce a significantly better fit than a simple model (Moffat exponent fixed) (Conover, 1980). Since the Gaussian and a Moffat are of different functional forms (i.e "non-nested"), the F-test unfortunately cannot be applied to test the change in fit.

$$F = \frac{\frac{RSS_1 - RSS_2}{p_2 - p_1}}{\frac{RSS_2}{n - p2}} \tag{2.13}$$

where p is the number of parameters in a given model and models 1 and 2 are chosen such that $p_2 > p_1$.

In this case, the change in parameters $p_2 - p_1 = 1$ and the number of data points is 7x7, or $n = 49$. The F statistic is computed and compared with the F-distribution to determine the confidence level of the additional parameter. For all spots it is found to be > 0.99 in favour of the additional Moffat parameter.

2.2 Least-Square Inversion Flux Extraction Alogirthm

To improve on the aperture-based method for flux extraction, I utilize the known lenslet PSF and wavelength calibration to extract the flux on the polarization spots or along the microspectra to generate the datacubes. The template PSFs from Section 2.1 from the polarization mode, are not used as they are an insufficient representation of the microlens PSF. This is a fundamental step for converting light on the detector into scientifically relevant data from a lenslet based integral-field spectrograph. This

process can cause large systematic noise and uncertainty, so its optimization is crucial to the data quality.

2.2.1 Reference Images

In order to run the flux extraction process, we first need to generate reference images for the signal and noise components of the detector images which we can adequately model. The reference images serve as the model parameters for fitting the detector image. A subsection of the detector image is selected around the microspectra of interest and includes immediate neighbours which may overlap. Correction for the microphonics requires processing the science image of interest, outlined in the following section. The PSF images for signal extraction of the spectra and polarization spots require calibration images which are determined by methods described by other articles in the Gemini Planet Imager Observational Calibrations series: Ingraham et al. (2014b); Wolff et al. (2014).

Microphonics

In order to isolate microphonic noise, a 64x64 pixel subsection of the CCD detector is selected from within a single amplifier band. The section is median-filtered to remove the signal contribution to the image. A 2D Fourier transform is used to select the frequencies of the microphonics pattern closest to the frequency of vibration. Since the microphonics are predominately in the vertical direction, only vertical frequency components are used. This is confirmed by the 2D Fourier power spectrum. Then several images are made by generating sine and cosine images with those frequencies which have the highest power from the Fourier transform. This approach is an alternative to the destriping algorithm (see Ingraham et al. (2014a)) in the GPI pipeline because the least square extraction algorithm (see section 2.2.2) allows for coherent noise contributions to be modeled and decorrelated from the signal simultaneously.

High-Resolution PSF

A high-resolution model for the microlenslet PSF is derived using a method developed originally for *HST* WFPC2 by Anderson and King (Anderson & King, 2000; Ingraham et al., 2014b). The empirical model of the PSF is generated using arc lamp spectra from GPI at various sub-pixel positions (see Figure 2.12a) (Ingraham et al., 2014b). For each sub-image, a high-resolution PSF is selected and then interpolated by a

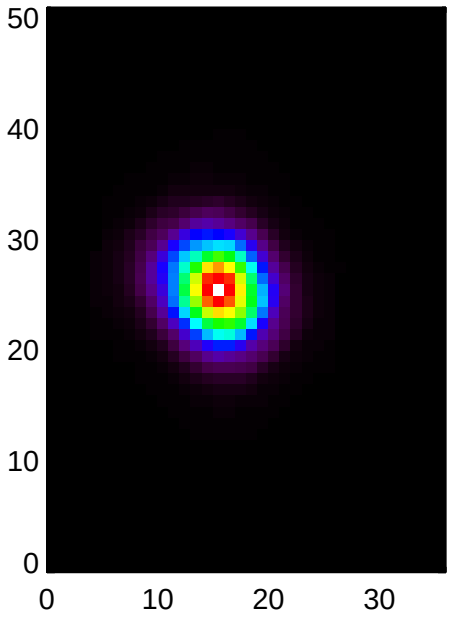

(a) High Resolution Empirical PSF

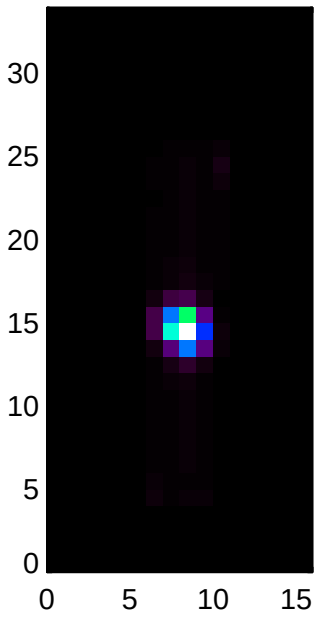

(b) Detector Resolution PSF

Figure 2.12 **(a)** High resolution PSF generated using the method from Ingraham et al. (2014b) with emission line spectra. **(b)** PSF binned to detector resolution and positioned on microspectrum within a subset image using a GPI wavelength calibration. This is a reference image for a single wavelength on the central microspectrum.

bilinear method to a sub-pixel position and grid appropriate to the subset image (see Figure 2.12b).

The sub-pixel position at which to place the reference PSF image within the spectra is determined from the wavelength calibration generated by emission lamp spectra (Wolff et al., 2014). The PSFs are separated by the resolution limit of ∼2 pixels to preserve the stability of the matrix inversion, so that no two reference images are too extremely correlated. Such a correlation would cause oscillating positive and negative solutions. PSFs are placed on the spectra of interest as well as the neighbouring spectra. This is done to remove contamination from neighboring lenslets within the image. For example, near the edges of the detector in all infrared bands, spectra are tilted at increasingly large angles due to the properties of the refractive optics within the IFS and start to blend with neighbouring spectra. In the K-bands[3], a section down the middle of the detector has spectra touching end to end from each lenslet, which affect the ends of the datacube. Extracting these spectra simultaneously allows them to be decorrelated, producing a cleaner data cube than the rectangular aperture algorithm (see Figures 2.16 and 2.17).

In polarization mode, light from each lenslet is split into two orthogonal polarization states via a Wollaston prism (Maire et al., 2010). The spots are sufficiently separated and uncorrelated with other spots. This means they only require a single PSF for flux extraction. High resolution versions of the polarization mode spots are made separately using unpolarized flat field images with the same algorithm used for spectral mode. Due to chromatic aberrations, polarization mode lenslet PSFs are sufficiently different from spectral mode PSFs to warrant the use of different PSFs between the two modes. This is more clearly shown in Section 2.1

2.2.2 Inversion Algorithm

The algorithm for flux extraction follows a linear algebra approach. The least-squares solution is found using a basis set formed from a system of known reference images. The basis set can then be used to model the data image being fit. Similar applications were used in other astronomical image processing pipelines for PSF subtraction (Lafrenière et al., 2007; Marois et al., 2010). This approach involves the inversion of a correlation matrix of the reference images in order to determine each individual

[3]GPI has two filters to cover the K-band referred to as K1 & K2. This is due to the fact that the spectra would completely overlap if the wavelength range was not cutoff by a filter.

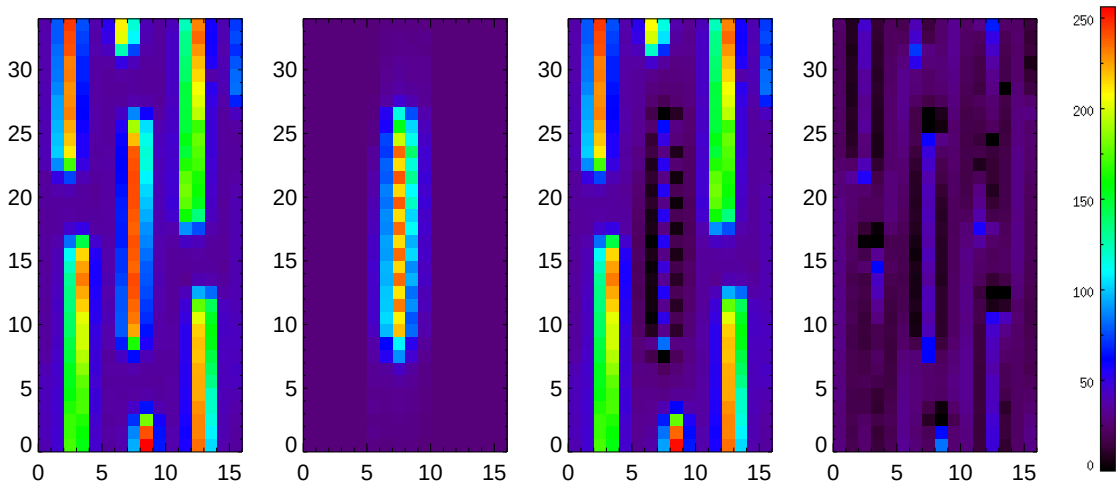

(a) Data (b) Extracted Flux (c) Extracted Residual (d) Modeled Residual

Figure 2.13 Spectral extraction using least squares PSF method. The x and y axes are in pixels and share a linear color scale derived from the minimum and maximum counts in the original detector image. **(a)**: Subsection of the raw detector image centred on a microspectrum. **(b)**: Reconstructed spectrum based on the PSFs used to extract the flux. **(c)**: Residual for the detector image minus the extracted spectrum. Note that the oscillating pattern in the y-direction is due to the resolution limit, which prevents continuous spacing between PSFs for the inversion method. This necessitates subpixel dithering to complete the interpolation of flux between each PSF in the final GPI datacube. **(d)**: A full residual using the spectrum gained from dithering the extraction, modeling the detector at 0.1 pixel PSF separation, and subtracting from the data.

reference image's contribution to the data image.

Using the formalism of least squares, we define D to be the data image and M to be the model image which is fit to the data.

$$RSS = (D - M)^2 \tag{2.14}$$

The model image is the product of a set of reference images (outlined in the previous section) and a coefficient vector equivalent to the flux within a given PSF or relative power in a noise image (i.e. microphonics). We define the basis set of reference images as $A_k = \{R_0, ..., R_k\}$ and the coefficient vector as $\vec{f_k}$.

$$RSS = (D - \sum_k \vec{f_k} A_k)^2 \tag{2.15}$$

Taking the derivative and setting it to zero we find the least square estimator of the vector $\vec{f_k}$, where A_j is an identical set to A_k.

$$\frac{\partial RSS}{\partial \vec{f_k}} = 2 \sum_j A_j (D - \sum_k \vec{f_k} A_k) = 0 \tag{2.16}$$

$$\sum_j A_j D = \sum_j A_j \sum_k \vec{f_k} A_k \tag{2.17}$$

Rearranging and simplifying terms we get Equation 2.19, where $\mathbf{C}$ is a correlation matrix of the reference images with themselves and $\vec{v}$ is a vector of the flux from each reference multiplied by the data image.

$$\left(\sum_j A_j D \right) = \left(\sum_j A_j \sum_k A_k \right) \times \vec{f_k} \tag{2.18}$$

$$\vec{v} = \mathbf{C} \times \vec{f_k} \tag{2.19}$$

First, the correlation matrix ($\mathbf{C}$) is generated by taking the set of reference images, R_0 through R_k, and element-wise multiplying[4] with an identical set of reference images, R_0 through R_j, where j and k are the reference image numbers. The product of the two images is element-wise summed to get the relative degree of correlation between the two reference images (see Equation 2.20). The result is a square matrix

[4]The mathematical symbol of an element-wise multiplication is ($\circ$), where elements of corresponding indexes in a matrix are multiplied to result in a matrix of the same size as the input matrices.

where each element of the correlation matrix (c_{jk}) is the sum of the product of reference image number j with image number k. Each reference PSF image is normalized to a constant before multiplication to give equal weight between PSFs. This results in a square matrix whose size depends on the number of reference images required for the subset data image.

$$\mathbf{C} = \begin{bmatrix} c_{00} & \cdots & c_{j0} \\ \vdots & \ddots & \vdots \\ c_{0k} & \cdots & c_{jk} \end{bmatrix} ; \text{where } c_{\mathrm{jk}} = \sum(\mathrm{R_j} \circ \mathrm{R_k}) \tag{2.20}$$

Secondly, each reference image is then multiplied with the subset data image (D) and summed to yield a vector of the detector counts within each reference image.

$$\vec{v} = \begin{bmatrix} v_0 \\ \vdots \\ v_k \end{bmatrix} ; \text{where } \tilde{\mathrm{v}}_{\mathrm{k}} = \sum(\mathrm{D} \circ \mathrm{R_k}) \tag{2.21}$$

The third step is to invert the correlation matrix through standard Gaussian elimination with IDL INVERT and solve for $\vec{f_k}$. Non-negative matrix inversions were also tested. They allowed the PSFs to be more closely spaced but increased the computation time and still required a dithering approach to provide a more complete interpolation of the underlying spectrum. PSFs which are sufficiently spaced do not tend to reach negative values, which are considered unreal systematic noise as the detector should only have positive flux contributions. Singular-value decomposition matrix inversion was also tested but again provided no substantial improvement over the simpler method. The inverse correlation matrix is multiplied by the flux vector to get the reference image coefficients within a least squares minimum residual (see Figure 2.13). For reference images of a PSF the coefficient is equivalent to the monochromatic flux at the wavelength determined by the wavelength calibration.

$$\vec{f_k} = \mathbf{C}^{-1} \times \vec{v} \tag{2.22}$$

This process is repeated after shifting the PSF locations by two thirds of a resolution limit (2 pixels) to either side of the accepted wavelength calibration along the dispersion axis to build up flux contributions at other wavelength values. A GPI cube is then interpolated at a uniform wavelength separation at each lenslet of the array.

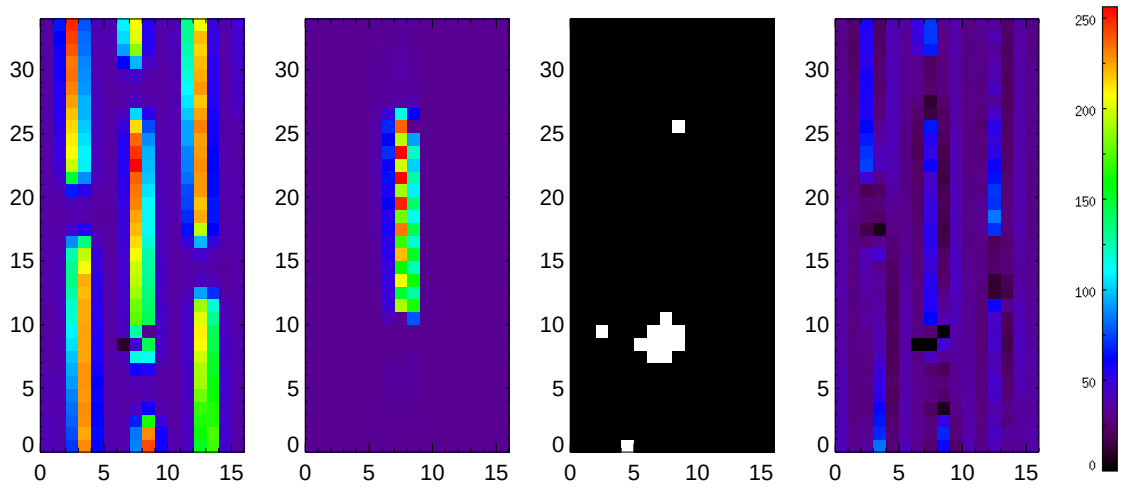

(a) Data (b) Extracted Flux (c) Bad Pixel Mask (d) Modeled Residual

Figure 2.14 Another spectral extraction showing bad pixel masking. The x and y axes are in pixels and linearly scaled to the same maximum and minimum values. **(a)**: Raw Detector subset image, **(b)**: Extracted spectrum, **(c)**: Bad pixel mask applied to weight the extraction. Note the gap in the extracted spectrum image requires interpolating across the gap in the spectrum as a function of wavelength. **(d)**: The full residual after spectral interpolation.

2.2.3 Bad Pixel Masking

It is also an option to isolate bad pixels during the flux extraction process. Bad pixels are identified through an accumulation of dark images using methods outlined in Ingraham et al. (2014a). Once the reference images are made, the bad pixels within an extracted subset image are set to zero through element-wise multiplication of the bad pixel mask (B). This is done before the correlation matrix ($\mathbf{C}$) and flux vector ($\vec{v}$) are calculated so that they replace the reference image (R) and do not contribute to the extracted flux value during the least squares algorithm (see Figure 2.14):

$$R_{masked} = R \circ B. \tag{2.23}$$

2.3 Solving the Flexure Offset Problem

The intrinsic design choice of having GPI be mounted at the Cassegrain focus implies there will always be some measure of flexure because the instrument cannot be perfectly stiff due to engineering limitations. I therefore developed two approaches to bootstrap the flux extraction to solve for the flexure offset using the data itself.

2.3.1 Flexure Offsets

GPI is mounted at the Cassegrain focus at Gemini South and therefore experiences a varying gravity vector during an observing sequence. Flexure between the lenslet array and the detector causes the light to move upwards of 2 pixels in any given direction on the hybrid CMOS detector (Perrin et al., 2014). The result is that an earlier wavelength solution taken with the telescope at a different elevation cannot be directly applied. In order to adapt to flexure during observations, we employ two methods to find the optimal signal extraction: iterative wavelength calibration offsets and 2D cross-correlation. Primarily the concern is to find a global offset; however there are FOV effects which require localized offsets for each lenslet (Wolff et al., 2014). The iterative solver can find offsets for each lenslet or take a global average while the cross correlation method finds only the global offset. Both of these approaches work in two different coordinate regimes, detector xy-shifts and dispersion coordinates of angle, perpendicular, and parallel shifts. This is due to degeneracies discussed in the

following sections.

Iterative Solver

Using the IDL AMOEBA downhill simplex method, the wavelength calibration is given three variable offset parameters to find the minimum residual. The 'perpendicular shift' is an offset to sidestep the spectra into place. The 'angle' parameter adjusts the angle of the dispersion axis. Finally, the 'parallel shift' adjusts the position along the spectra. The biggest problem with this method is that the offset along the dispersion axis is not well constrained without spectral information because the extraction algorithm can find a minimum residual with some PSFs falling outside the spectrum. While shifting the extraction, PSFs are free to "slide" off the end of the band such that one PSF at the end of the wavelength range extracts detector noise, especially in low signal-to-noise regime. Effectively, the minimum residual does not represent the wavelength solution of the light accurately. Another option which is implemented is to perform a two parameter offset in xy-detector coordinates; but because the y-axis is predominately the dispersion axis, there is a similar problem. This is partially mitigated by using spectra on the edge of the detector which have different dispersion angles, such that they are not completely vertical.

Another problem arising with this method is that it requires solving for the reference images and inversion algorithm ∼10-20 times for a 2 pixel range of offsets at a 0.1 pixel convergence. This drastically increases the computation time over using a single extraction with a global offset. Furthermore, if the minimum residual is not constrained to a common value, the wavelength solution will vary across the FOV such that flux at one end of the image is from a different wavelength of light than the other side.

2D Cross-Correlation

Another method which is used to determine the flexure is to cross-correlate a modeled spectra image (M) with the detector image (D) (Figure 2.15). First the extraction algorithm is run to compute a rough spectrum for a large subset image, which is either the observing target star flux or sky background. The extracted spectrum is used to forward model the data (see Figure 2.15b) to provide an image for cross-correlation.

The correlation matrix ($\mathbf{C}$) is built using the data and the model image given a grid of subpixel offsets through Fourier transforms seen in Equations 2.24 and 2.25. The peak correlation is selected using the maximum total value. The offsets produced in subpixel detector xy-coordinates (dx, dy) can then be used to re-extract the spectrum and iterate the forward modeling and cross-correlation until a convergence in shifts results in a minimal residual (see Figure 2.15c). The entire routine takes less than 5 calls with a 2 pixel range search, which narrows with each iteration, and at a defined ~ 0.05 subpixel offset convergence.

$$\mathbf{C} = \begin{bmatrix} c(-dx,-dy) & \cdots & c(-dx,dy) \\ \vdots & \ddots & \vdots \\ c(dx,-dy) & \cdots & c(dx,dy) \end{bmatrix} ; \text{where } c(\mathrm{dx},\mathrm{dy}) = \sum(\mathrm{D} \circ \mathrm{M}_{\mathrm{shift}}) \quad (2.24)$$

$$M_{shift}(x+dx, y+dy) = \mathcal{F}^{-1}(e^{-2\pi i(u*dx+v*dy)}\mathcal{F}(M(x,y),u,v)) \quad (2.25)$$

The benefit of this method is that fewer calls to the extraction algorithm are needed, but more computation is spent on generating the model image for the 2D cross-correlation. In practice, this method takes much less time then the iterative solver: on the order of 3 minutes on a single processor rather than 40 minutes on 15 processors. The dispersion offset (predominately detector y-axis offsets with angle $\approx 0^{\circ}$) is better constrained in this method because the shape of the spectra plays a role in the derived offsets. This is in part due to modeling the edge of the detector where the spectra have been distorted to have a non-zero dispersion angle. Having spectra at different angles results in a more constrained cross-correlation when used in combination, rather than having a completely repeated, uniform shape. The cross-correlation can also be run in 1D as a perpendicular shift by combining detector xy-offsets at a fixed angle and converges reliably for large offsets. This does not, however, represent the full flexure offset as flexure will also cause a shift along the dispersion axis.

In the case of the polarization mode, the spots are easier to match given they are single PSF sources. Typically, one to two iterations of modeling and cross correlating are sufficient to find the offsets to subpixel accuracy. Also, the y-offsets are no more indeterminate then the x-offset due to their point-like nature.

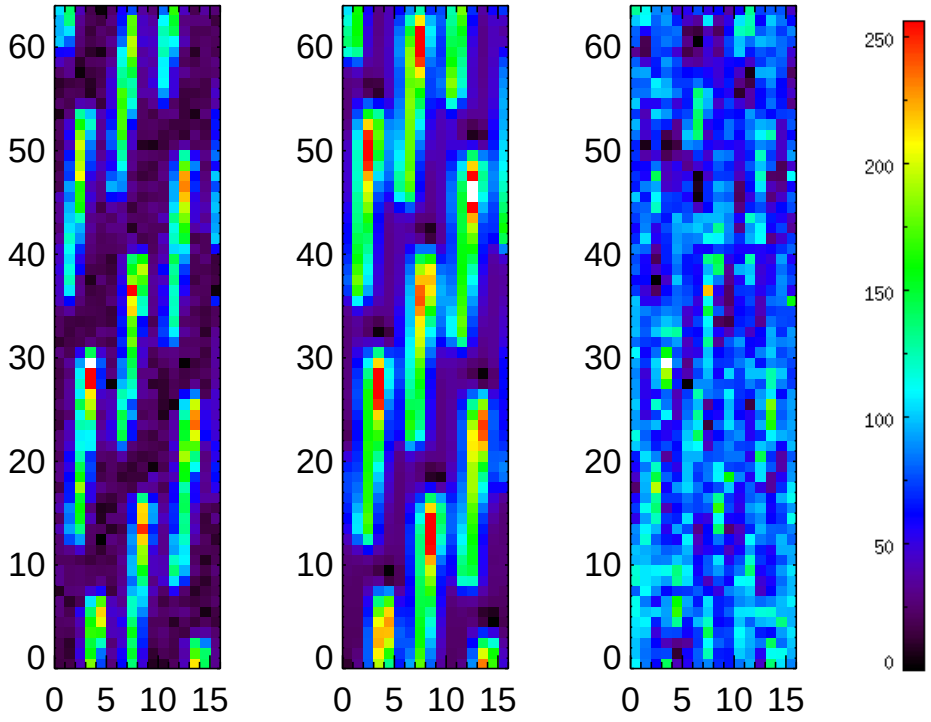

(a) Data (b) Model (c) Residual

Figure 2.15 **a)** Detector subsection with stellar spectra from standard star. **b)** Model image of the detector given a dithered spectral extraction from the data image, the microlens PSF separated at 0.01 pixels, and wavelength calibration adjusted for flexure offset. **c)** Residual frame of the model after scaling to match flux.

In order to determine how well the routine converges to a true flexure offset, science data is used in conjunction with an arc lamp observation at the same telescope elevation taken just prior to the science target. The modeling and cross correlation is run on the star PZ Tel data taken at Gemini-South on May 11th 2014 with varying initial offsets from the wavelength calibration to test for convergence. Table 2.3 shows the offsets determined by the modeling and cross correlation routine for an Ar Arc lamp taken just prior to an observation of PZ Tel in the H-band. The XY-offset is found for the arc lamp more precisely by matching the extracted emission lines with their rest wavelength. These offsets are assumed to be the true flexure offset from the wavelength calibration because we know the spectrum precisely. For the science image of PZ Tel, the X-offset converges well (-0.46 vs. -0.41 pixels), but the Y-offset still has some variation due to the changing spectral shape (-0.07 vs. -0.27 pixels). Using stricter convergence criteria tends to make the solution divergent and may be a limitation on how well the spectra can be extracted and subsequently modeled.

2.4 Summary

The final result of the methods outlined here can be seen in comparison with the rectangle aperture method in Figure 2.16 and Figure 2.17 on a K2 flat field image. Figures 2.16 and 2.17 are scaled to the same flux range. PSF method have noticeably higher flux extraction in part due to 2D cross correlation finding the flexure offset prior to extraction. Given no initial offset, the routine found an offset of 0.77 pixels in x and -2.45 pixels in y. Figure 2.16 illustrates how the ghosting of flux at the end of the band (2.107 μm in K2) is reduced using the inversion method to decorrelate contaminating flux from other lenslets. Figure 2.17 illustrates the use of bad pixel masking during the reduction which minimizes extraneous values in an image slice, seen as fewer dark lenslets. Furthermore, the "checkerboard" aliasing pattern from alternating sub-pixel positioning for adjacent lenslets is reduced. A real stray light feature caused by a caustic aberration in Figure 2.16c can be seen in the microlens inversion extraction, but not in the box aperture method. This is likely due to the systematic noise induced by the aperture method when compared to properly weighting a PSF extraction to resolve fainter features. In all of these Figures, the gradient from top to bottom in is due to thermal background emission, and the darker region along the top is from an internal cold stop baffle that blocks the thermal

Table 2.3 The global average XY-offset due to flexure are found for the following observations. The wavelength calibration is given artificial flexure offsets (XY-initial) to test for convergence with different starting parameters. Offsets are in pixels, while telescope orientation is in degrees. The telescope elevation is shown to be very close, such that they should have the same flexure offset. The arc lamp is found to have the true offset by matching the emission line spectra. The Y-offset does not converge to a single value as well as the X-offset, but taken as an average, is quite close to the accepted values from the Ar arc lamp.

Target (Band)	X-Offset (px)	Y-Offset (px)	X-Initial (px)	Y-Initial (px)	Elevation (°)
Ar Arc (H)	**-0.46**	**-0.07**	0	0	66.1
PZ Tel (H)	-0.42	-0.2	0	0	65.4
⋮	-0.41	-0.59	-1	-0.5	⋮
⋮	-0.42	0.18	-1	0.5	⋮
⋮	-0.42	0.12	0.5	0.5	⋮
⋮	-0.40	-0.88	0.5	-1	⋮
Mean Offsets	**-0.41**	**-0.27**	All	All	65.4

background near that edge of the detector. This is not vignetting or a low flat-field response along that edge. When the methods outlined here have been refined, the preferred method for science-quality results will use these flux extraction techniques for PSF reduction and spectral/polarimetric characterization of targets to minimize systematic error and noise propagating from the detector to the data cubes.

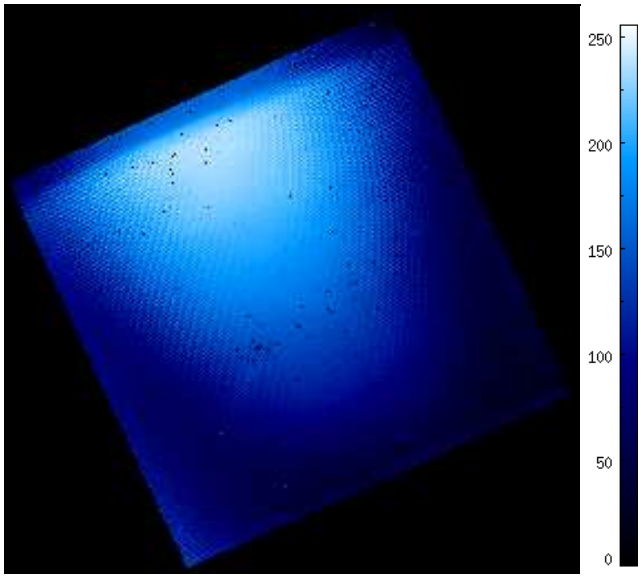

(a) Box Aperture Method

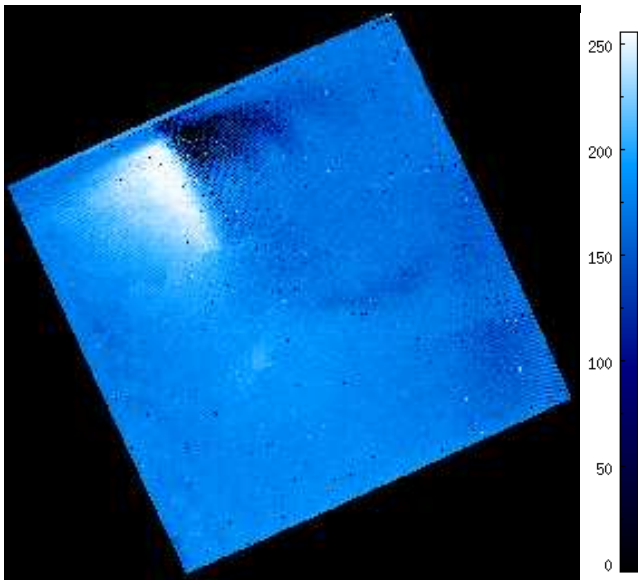

(c) Microlens Inversion Method

Figure 2.16 : Final data cube slices comparing the box aperture with the microlens inversion method on the same K2 band flat field image at 2.107 μm (i.e., the blue end of the band). Both figures are scaled to the same flux range as Figure 2.17. The "checkerboard" pattern is quite noticeable in the box aperture method. There is also significant ghosting in Figure 2.16a from neighbouring lenslets contaminating the extraction, which is reduced to a smaller region in Figure 2.16c with the microlens inversion. A real faint noise source caused by a stray light feature in the IFS is only discernible by eye through the microlens inversion technique in Figure 2.16c.

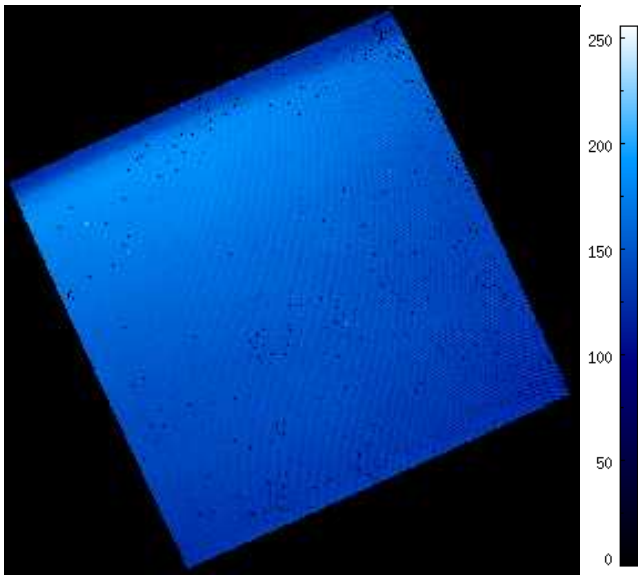

(a) Box Appeture Method

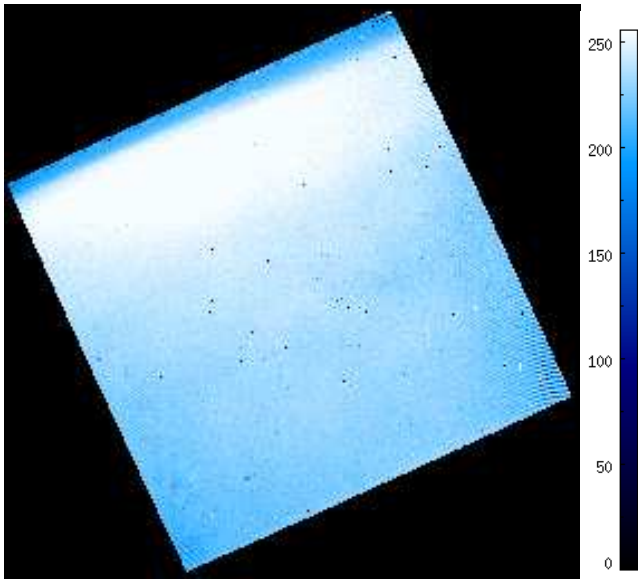

(c) Microlens Inversion Method

Figure 2.17 : Final data cube slices showing the same K2 band detector flat field images as Figure 2.16. The figures both show the wavelength slice at 2.228 μm (i.e. central region of the band) and are scaled to the same flux range as Figure 2.16. The microlens inversion slice shows an increase in flux extraction, reduced bad lenslet pixelization, and reduced "checkerboarding" from alternating sub-pixel positions.

Chapter 3

Insights on the λ Boo Phenomenon Through Herschel

The λ Boo stars are Population I, type A0-F3 stars (1.5-2.5 solar masses) of various ages with strongly depleted alpha and Fe-peak element abundances but relatively normal solar abundances of C, N, O, and S. The α-elements include Ne, Mg, Si, Ar, Ca and Ti. They are grouped because they form from α-capture, whereby Helium-4 is captured in a ladder of fusion reactions (Woosley & Weaver, 1995). Fe-peak elements are V, Cr, Mn, Fe, Co and Ni which are heavy metals that are near Fe in atomic number, where fusion processes no longer produce an energy surplus but instead require energy from the environment, to cause a build up in abundance. The primary distinction between the heavy elements, which are underabundant, and C, N, O, and S is the sublimation temperature on dust grains typical of a planetary environment (Lodders, 2003). These elements are also commonly observable in optical spectra. C, N, O, and S are predominately in the gas state when in vacuum at $\sim$100 Kelvin. Around our sun, this would be about half the typical equilibrium temperature on Mars. The heavy metals on the other hand require 1000 Kelvin or greater to sublimate, a condition only met within Mercury's orbit in our solar system. Therefore through preferential accretion of gas, an abundance anomaly could be formed where C, N, O, and S are accreted onto the star in the gas state while the heavier elements are locked away in dust grains which are blown out of the system due to radiation pressure (Venn & Lambert, 1990). This abundance pattern based on sublimation temperature allows these stars to be distinguished from other metal weak stars such as Pop II or F-weak stars to constitute a class of their own (Paunzen et al., 2014).

Multiple theories have been proposed to explain the λ Boo phenomenon, but none have risen to complete satisfaction. External mechanisms which have been proposed include debris disks and ISM interactions, which would provide the source of matter for a post formation accretion. Through the use of *Herschel* observations, these two scenarios can be distinguished by modeling differences in the typical dust properties observed in order to provide insight into the λ Boo phenomenon.

3.0.1 Knowledge to-date on the Phenomenon

There are 34 confirmed λ Boo stars which makes them less than 2% of all stars within their spectral range (Paunzen, 2004). While λ Boo stars are particularly metal deficient, 20% of A stars are actually metal rich in Fe-peak elements, likely due to their post-solar formation age. Estimates on the number of λ Boo stars which have an IR-mm excess range from 23% of the whole sample, which is typical of A-stars, to 70% from a *Spitzer*-only sample (Paunzen et al., 2003; Su et al., 2006). Therefore the phenomenon has been associated with an IR photospheric excess. Modifying the most conservative estimate of 23% by including disks determined may have an excess and exclude stars with only ISO upper limits, the estimate easily exceeds 50% (6/26 vs 8/15). In fact the system HD 11413, which was previously contentious, is now shown to have an excess due to *Herschel* observations. Therefore the constraints placed by near-IR excess detections are not conclusive given that more sensitive far-IR observations can more readily detect the cold disks.

A second property of λ Boo stars is that they are more likely to pulsate in the instability strip[1] than normal A-stars (Paunzen, 2004). This is often called the δ Scutti phenomenon and is due to the increasing/decreasing of the opacity of the ionized helium boundary layer. This oscillation in ionizing helium occurs because the ionization temperature is within the internal temperature and pressure range of a main-sequence A star (De Boer & Seggewiss, 2008). λ Boo stars are also characterized by higher overtone modes rather than lower mode oscillations typical of δ Scutti stars. There has been no correlation with the Period-Luminosity-Colour relation of δ Scutti stars and observed metallicity, which might distinguish λ Boo stars from the δ Scutti phenomenon (Paunzen, 2004).

Theories for what causes the λ Boo phenomenon fall primarily into two categories:

[1]Nomenclature for a region in a Hertzsprung-Russell Diagram (which plots luminosity vs. surface temperature of a star) where pulsating stars are commonly found.

those external to the photosphere and those internal to the photosphere. External mechanisms include debris disks, ISM interactions, and close-in binaries. The debris disk and ISM interaction both pollute the surface with gas but blow out metal-rich grains, leaving an apparently C, N, O, and S rich surface (Paunzen, 2004). These two external mechanisms cannot be distinguished with SED characterization alone, but can be differentiated based on the effects of grain size, since the ISM grains are typically much smaller than grains in debris disks. It has also been argued that, for close binaries, the λ Boo phenomenon is not real and is an artifact of not resolving the stars separately (Faraggiana et al., 2004). HD11413 was found to be a composite spectra binary via cross correlation with a synthetic spectrum. This method is prone to systematic error and was not a definitive RV detection of a binary. Griffin et al. (2012) did a multi-year spectroscopic survey of λ Boo stars to detect RV shifts and found none to have composite spectra binaries. Some of those stars are considered here including HD 125162, HD 183324, and HD 221756.

For the internal mechanisms, the mass-loss mechanism which explains the AmFm phenomenon could explain the λ Boo phenomenon if the mass-loss rate were increased ($> 10^{-13} M_{\odot}$/yr) (Michaud & Charland, 1986). AmFm stars is a descriptor for a class of A and F type stars found to have chemical peculiarities on the surface due to a radiatively driven stellar wind (Michaud et al., 1983). Since the radiative pressure is most effective for heavy metals, it leads to a similar abundance pattern as λ Boo stars. The AmFm phenomenon however, is not observed in stars with rotational speeds above 90 km/s due to meridional circulation[2] mixing the underabundances with the lower layers of the star. Since λ Boo stars on average rotate at 120 km/s $v \sin(i)$, the mechanism is not plausible. However, λ Boo stars also exhibit unique pulsational properties that do require an internal mechanism and thus cannot be ruled out. It may be that the pulsations are linked to a diffusion mixing process which causes the abundance pattern on the surface that is not yet understood (Paunzen, 2004).

Interestingly, the meridional circulation would also negate an accretion abundance pattern in $\sim 10^6$yrs and yet λ Boo stars are observed at various ages. This then requires the λ Boo mechanism to operate during the entire main sequence, which gives some additional support to the external mechanisms. ISM interactions can occur randomly with age and while debris disks form out of protostellar material and deplete with age, they have still been found around white dwarfs (Matthews et al.,

[2]Convection due to stellar rotation causing the star to be oblate and therefore have cool equator and hot poles.

2014).

3.0.2 *Herschel Space Observatory*

The *Herschel Space Observatory* is a European Space Agency (ESA) mission for a Far Infrared and Sub-millimeter observatory with a monolithic 3.5 meter mirror orbiting at the second Earth-Sun lagrangian point (L2). The wavelength range of 55 to 670 μm is opaque from the ground which necessitates space-based observations. The mission lasted from May 2009 to April 2013 when it finally ran out of coolant for the instrument suite. One of the instruments on board was the Photodetecting Array Camera and Spectrometer, or PACS. PACS was designed as an imaging photometer and integral field spectrograph.

In total 8 λ Boo stars were observed and analyzed with PACS in this thesis. Two were observed as part of the DEBRIS Key-Time Programme (HD 125162, HD 110411) and 6 were observed as a targeted PI proposal (HD 11413, HD 30422, HD 31295, HD 198160, HD 221756, HD 183324). All 8 have broadband photometry at 100 and 160 μm. With these observations, we can break the SED degeneracy between an ISM bowshock and a debris disk. Measuring the temperature and radial extent of the emission differentiates ISM dust from debris disk dust due to a variation in mean grain size affecting the equilibrium temperature. Booth et al. (2013) studied HD 125162 and HD 110411 in the context of A-stars in the DEBRIS survey and found them to host well-resolved debris disks. I therefore consider only the remaining 6 sources to test whether the excess emission originates from the ISM or debris disk. Those two sources however, are investigated with the whole sample when determining the feasibility of PR-drag in Section 3.5.

3.1 Angular Size of Far-IR Emission

The outer radial extent of excess emission can be constrained using *Herschel* PACS observations by measuring the Gaussian FWHM of the unresolved point sources. These measurements can then be compared with models of ISM bowshocks to determine if the emission is exterior or interior to these locations. If the ISM bowshock extent is larger/smaller than the measured emission than a debris disk model is favoured because debris disk emission would arise relatively close and compact to the star.

The *Herschel* PACS observations were reduced in a standard manner (Booth et al., 2013; Kennedy et al., 2012). All images were rotated for north up orientation. All of the sources appear as point sources in raw data images, but some are resolved. Each target is found at the centre of the image and a box of 20×20 pixels is selected from the full image and fit with MPFIT2DPEAK in IDL with a Gaussian profile. At 100 μm, a single image pixel is equivalent to 1 arsecond squared on the sky while at 160 μm a single pixel is 2 arcseconds squared. The */tilt* keyword is used to rotate the Gaussian for oblong shapes. The largest FWHM is then used as a measurement of the outer radius of the emission ($\theta_{measured}$). The true on sky extent of the emission (θ_{sky}) is calculated with simple Gaussian deconvolution with the Herschel PACS PSF, as shown in Equation (3.1).

$$\theta_{sky} = \sqrt{\theta^2_{measured} - PSF^2_{fwhm}} \tag{3.1}$$

This is repeated for both 100 and 160 μm where the maximal FWHM of the PSF is 6.89 and 10.65 arcseconds, respectively. The results of this analysis can be seen in Table 3.1, where the R_{outer} is the outer limit on the radial extent of the emission in Astronomical Units (AU) projected at the distance to the star.

In order to estimate the error in the outer radial extent, Gaussian fit parameters are changed until the residual sum of squares has changed by 10% from the best fit parameter. The FWHM value error is propagated through the deconvolution to determine the error in projected AU from the star. The error in the Hipparcos distance measurement is considered negligible to get the projected radius. Some error measurements result in PSF FWHM which are less then the instrumental FWHM which is non-physical, but suggests that the emission is not resolved and can only place an upper limit on the radial extent of emission.

γ Draconis was reduced and used in conjunction with these observations to serve as a PSF reference star. In addition to measuring the radial extent of emission, the PSF reference star can be scaled to the peak emission and subtracted from the data images to test for coherent structure above the noise around the point source. In Figure 3.1 it can be seen that HD31295 is well resolved, exhibiting a symmetric disk structure with the disk ansae[3] having peak emission to either side of the star. It is

[3]Ansae are the largest radial extent of a ring projected at some inclination.

Table 3.1. Size of Emission Around λ Boo Stars at 100 & 160 μm

Star (HD)	100 μm $\theta_{measured}$ ($''$)	100 μm θ_{sky} ($''$)	100 μm R_{outer} (AU)	160 μm $\theta_{measured}$ ($''$)	160 μm θ_{sky} ($''$)	160 μm R_{outer} (AU)
11413	8.08 ± 0.40	4.22 ± 0.77	162 ± 30	12.75 ± 1.46	7.00 ± 2.83	270 ± 109
30422	7.95 ± 0.49	3.97 ± 1.02	111 ± 29	12.31 ± 2.07	6.17 ± 4.83	173 ± 135
31295	9.98 ± 0.35	7.22 ± 0.49	129 ± 9	15.22 ± 0.89	10.87 ± 1.25	193 ± 22
183324†	7.87 ± 0.71	3.80 ± 1.57	116 ± 48	21.48 ± 4.57	18.65 ± 5.32	$570 \pm 163^{\dagger}$
198160	7.11 ± 0.68	1.75 ± 1.82	$66 \pm 69^{\star}$	11.94 ± 3.30	5.40 ± 5.45	$206 \pm 208^{\star}$
221756†	7.05 ± 1.15	1.49 ± 2.22	$59 \pm 89^{\star}$	17.82 ± 3.67	13.05 ± 4.67	$524 \pm 187^{\dagger}$

†Sources are likely contaminated with high redshift, background galaxies.

*Measurements at PSF resolution limit.

Note. — Table shows the angular size of emission assuming convolved Gaussians to constrain the spatial scale of far-IR emission. Angles are in arcseconds and radii are in AU. The radii of the emission (R_{outer}) are the projected sizes given the known distance to each star from Hipparcos.

important to note that bowshock features will typically be asymmetric due to the peak emission being at the bow apex. HD11413 and HD30422 also have faint structures which can be seen to either side of the star. HD198160 is the most point-like. This is likely due to its binarity truncating the outer edge of the debris disk. The binary pair is separated by 2.4 arcseconds (or 182 AU projected on the sky) and is a resolved pair of equal magnitude stars of likely the same mass (Jasinta et al., 1999). If the emission were the result of a bowshock it would likely be much larger in scale to encompass both stars, which provides ancillary evidence that the excess emission observed here is from a debris disk and not a bowshock. HD183324 and HD221756 are seen to have adjacent background sources, likely high-redshift galaxies, in both 100 μm and 160 μm images. There are no far-IR galaxy catalogs at the observed depth of this data, so verifying this would require follow up observations and characterization to verify this common hypothesis within the *Herschel* observing community. At 160 μm the problem is even worse; due to the poorer resolution, sources are blended, resulting in a false disk-like residual. In all of the images, there is no preference for the excess emission around the star to be at the leading edge of the proper motion (white arrows), as would be the case if it originated from a bowshock.

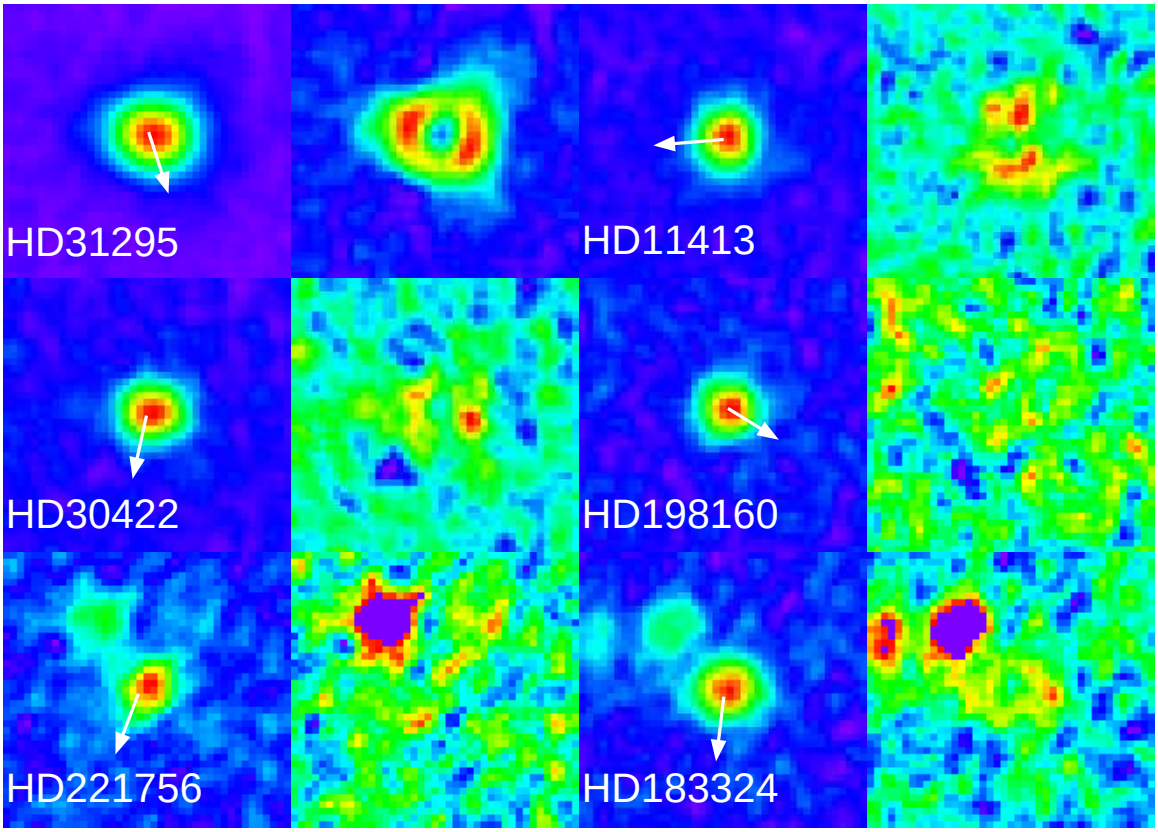

Figure 3.1 100 μm images of the 6 targeted stars. The FOV in each image is 20×20 and each image is individually scaled linearly to the minimum and maximum values. Each star is shown in raw data on the left and residual after PSF subtraction on the right. White arrows indicate the direction of proper motion. Vectors are normalized to uniform length to indicate direction and not velocity. There is no preference for emission to be in the direction of motion. For HD183324 and HD221756 the background galaxies have been masked and re-scaled to highlight the emission associated with the star.

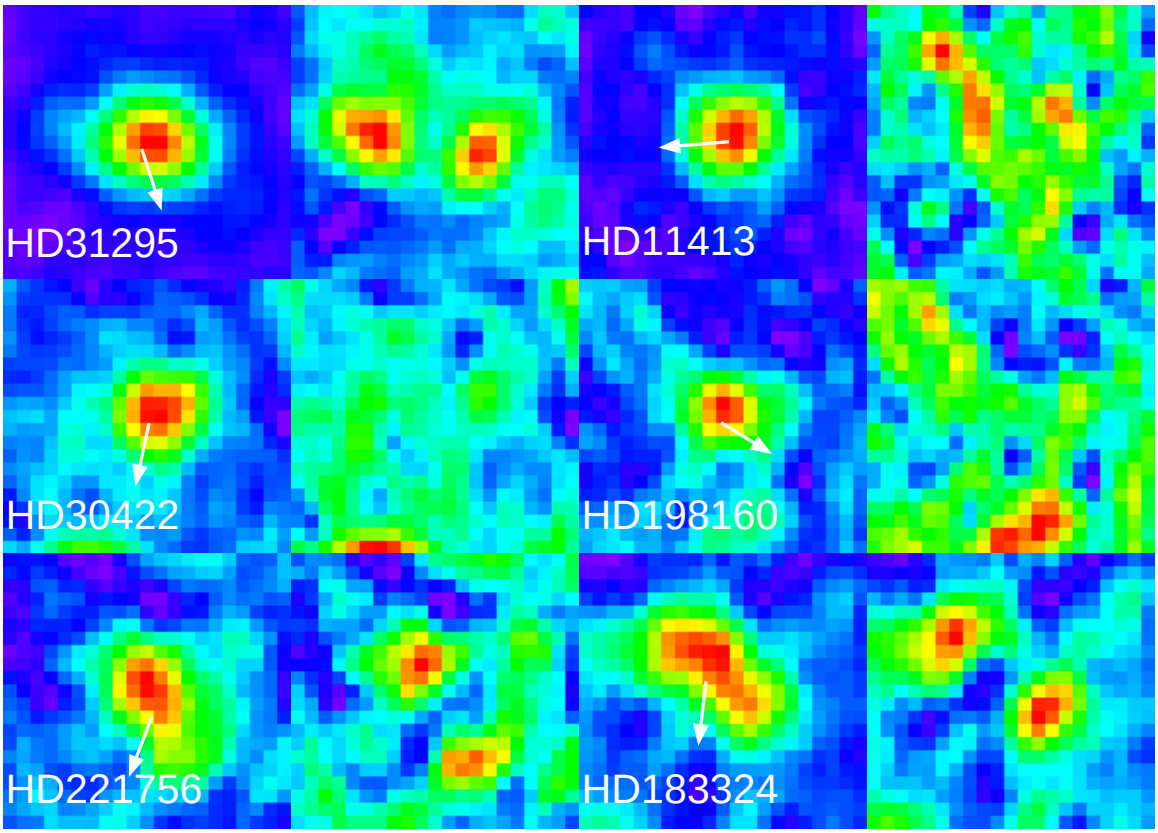

Figure 3.2 160 μm images of the 6 targeted stars. The FOV in each image is 20×20 and each image is individually scaled linearly to the minimum and maximum values. Each star is shown in raw data on the left and residual after peak-scaled PSF subtraction on the right. White arrows indicate the direction of proper motion. Vectors are normalized to uniform length to indicate direction and not velocity. For HD183324 and HD221756 the background galaxies have blended with the excess stellar emission and likely give a false disk-like residual. The proper motions can be seen to point parallel to the adjacent emission, indicating they are not from a shock front.

3.2 Spectral Energy Distribution of λ Boo stars

The peak of emission from debris disks is typically in the 100 μm regime given a typical blackbody of 50 to 100 Kelvin. Therefore these *Herschel* observations are ideally suited to establish the temperature of the excess emission.

For the 100 μm emission the sources were sufficiently separated from contaminating sources that aperture photometry was the best method to extract the stellar and excess emission associated with the star. An aperture radius of 18 pixels was used for all 6 target stars. All fluxes were calibrated by *Herschel's* encircled energy function, or EEF, for a particular band to account for flux lost to the far wings due to *Herschel's* broad PSF (Balog et al., 2014). Similarly apertures were used on the 160 μm data except for HD 183324 and HD 221756 where background galaxies likely contaminate the extraction. In those cases, PSF extraction was used to decorrelate emission associated with the star and the background (much in the same way flux is decorrelated on GPI's microspectra, as outlined in Chapter 2). It can be seen that the two sources are distinctly separated and only appear connected via overlapping wings of the PSFs. The position of the flux associated with the star is derived by the 100 μm peak position. PSF fitted fluxes are corrected by a multiplicative factor derived from a statistical offset (found in the DEBRIS survey) between aperture and PSF measurements. The flux measurements can be seen in Table 3.2 to show that all of the stars have a significant flux well above that predicted for a stellar photosphere.

The measurements in Table 3.2 can be used in conjunction with archival photometry to construct a multi-wavelength SED from UV to sub-mm. When available, photometry from optical surveys (Hauck & Mermilliod, 1998), 2MASS (Cutri et al., 2003), *WISE* (Wright et al., 2010), *Spitzer* (Su et al., 2006), *Akari* (Ishihara et al., 2010), and JCMT (SONS survey) was used to fit a stellar model and an additional modified black body spectrum. The black body equation can be seen in Equation 3.2 where h is Planck's constant, c is the speed of light, and k is Boltzmann's constant. The only independent variable over a given wavelength range is the temperature which can vary to fit the flux of the observations (Wyatt, 2008).

$$B(\lambda, T) = \frac{2hc}{\lambda} e^{\frac{-hc}{k\lambda T}} + 1 \tag{3.2}$$

Dust grains are inefficient emitters and require a modified Rayleigh Jeans tail power law to match observations at wavelengths greater than $\sim$200 μm. In that case β and λ_0 parameterize the slope and wavelength of where the modified blackbody

Table 3.2. Flux Measurements of λ Boo Stars at 100 μm and 160 μm.

Star	100 μm (mJy)		160 μm (mJy)	
(HD)	Measured	Photospheric	Measured	Photospheric
11413	55.8 ± 2.6	2.8 ± 0.4	40.6 ± 2.3	1.1 ± 0.2
30422	40.2 ± 3.8	2.1 ± 0.4	16.4 ± 1.5	0.8 ± 0.1
31295	391.6 ± 14	6.9 ± 0.2	190.7 ± 8.4	2.7 ± 0.9
183324	25.4 ± 1.1	2.5 ± 0.1	17.2 ± 3.3	1.0 ± 0.1
198160	30.7 ± 1.2	3.5 ± 0.1	14.3 ± 1.7	1.3 ± 0.1
221756	24.1 ± 1.1	3.2 ± 0.1	12.5 ± 2.0	1.2 ± 0.1

Note. — Photometry of the excess emission around the targeted stars at 100 μm and 160 μm. All fluxes are in milli-Janskys. For comparison, the predicted photospheric fluxes from the star alone are shown in adjacent columns and are based on ATLAS9 stellar models (Castelli & Kurucz, 2004) fit to optical and NIR photometry where dust emission is negligible.

intensity begins to fall off faster than a normal blackbody.

$$B_{modified} = B(\lambda, T) \times \left(\frac{\lambda}{\lambda_0}\right)^{\beta} \; ; \; when \; \lambda > \lambda_0 \tag{3.3}$$

In the case of HD 31295, two blackbody functions were fit to the SED in order to account for the IR as well as the sub-mm excess. In most cases a debris disk is parameterized by a single temperature due to the dust typically being a narrow annulus around the star. In the case of a two-body fit, it is presumed that a second, inner belt exists within the system. This would not be unrealistic given our solar system is a two-belt system with a warm asteroid belt between Mars and Jupiter's orbits and a cold Kuiper belt beyond Neptune's orbit. The SED fits for the central stars and IR excesses can be seen in Figures 3.3-3.10 below.

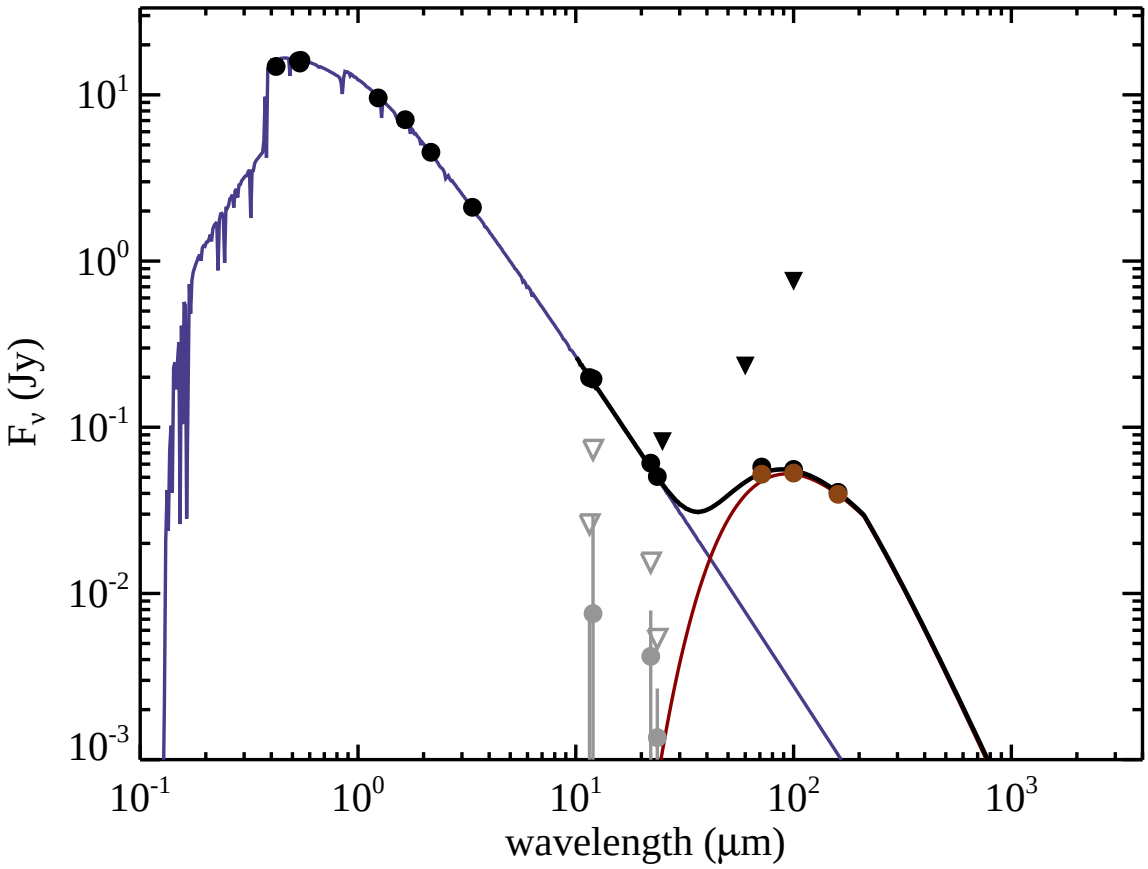

Figure 3.3 SED of HD 11413. The blackbody fit of the excess is for a temperature of 55 K with an effective disk radius at 118 AU. The blue line is the model stellar spectrum, the brown line is the disk blackbody SED, and the black line is the star+disk SED. Measured fluxes are in black dots, disk-only fluxes are in brown, and residual stellar fluxes are in grey. Inverted triangles are upper limits.

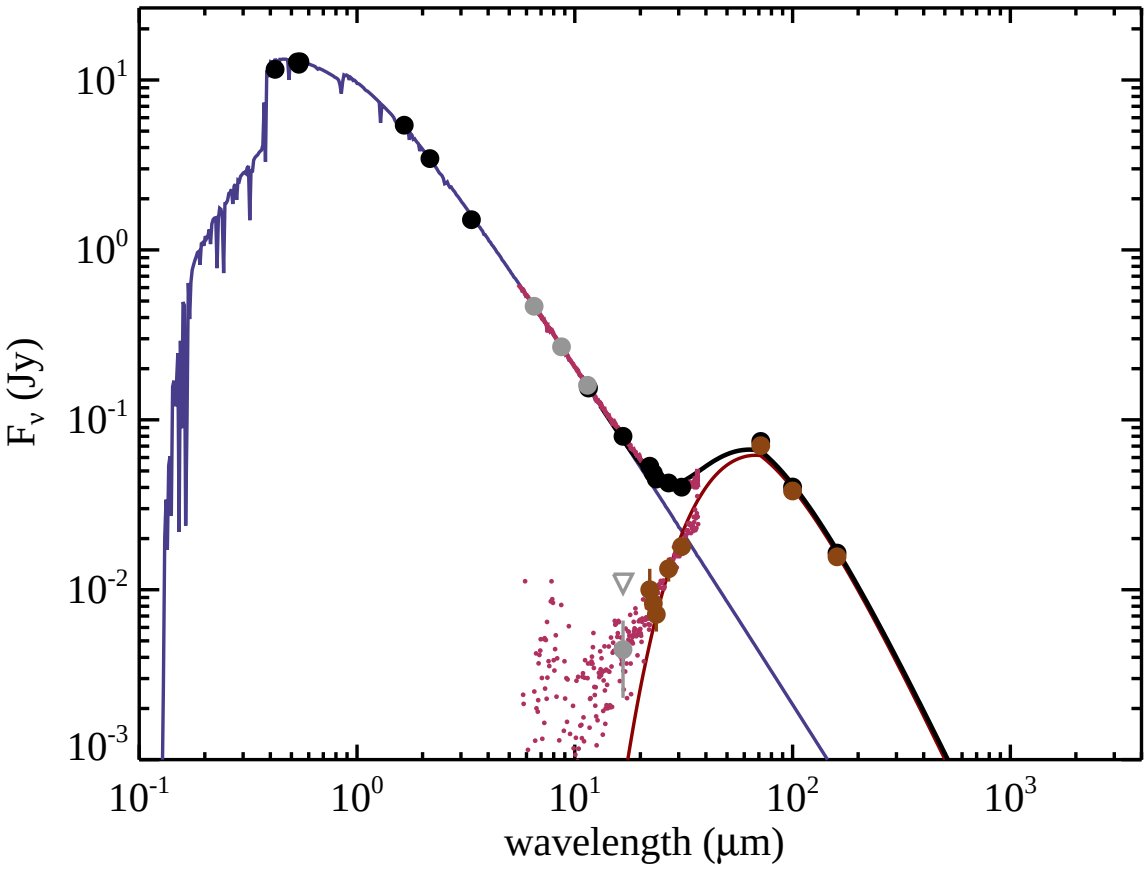

Figure 3.4 SED of HD 30422. The blackbody fit of the excess is for a temperature of 75 K with an effective radius of 41 AU. The blue line is the model stellar spectrum, the brown line is the disk blackbody SED, and the black line is the star+disk SED. Measured fluxes are in black dots, disk-only fluxes are in brown, and residual stellar fluxes are in grey. Spitzer IRS spectra are in purple. Inverted triangles are upper limits.

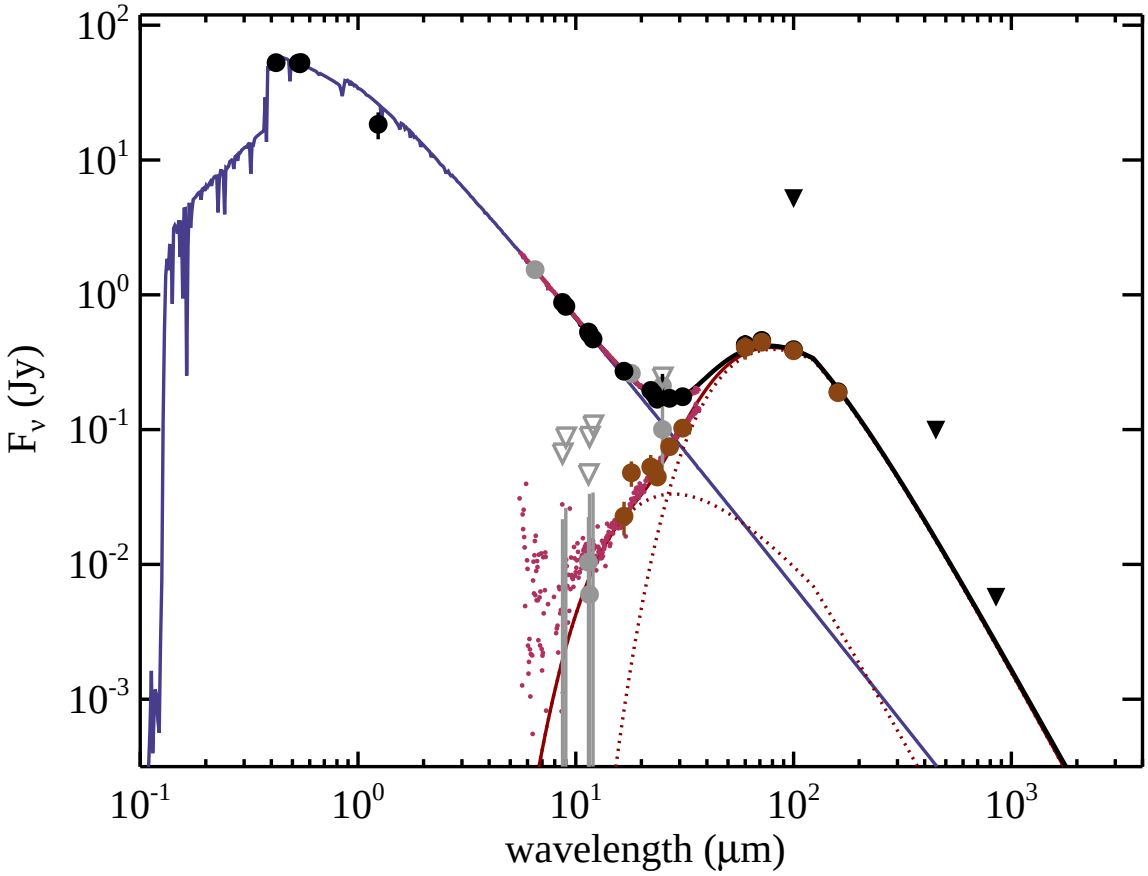

Figure 3.5 SED of HD 31295. The blackbody fit of the excess is for a temperature of 63 K and effecitve disk radius of 74 AU. A warm component SED was also fit for a temperature of 183 K and an effective disk radius of 9 AU. The blue line is the model stellar spectrum, the brown line is the disk blackbody SED, and the black line is the star+disk SED. Measured fluxes are in black dots, disk-only fluxes are in brown, and residual stellar fluxes are in grey. Spitzer IRS spectra are in purple. Inverted triangles are upper limits.

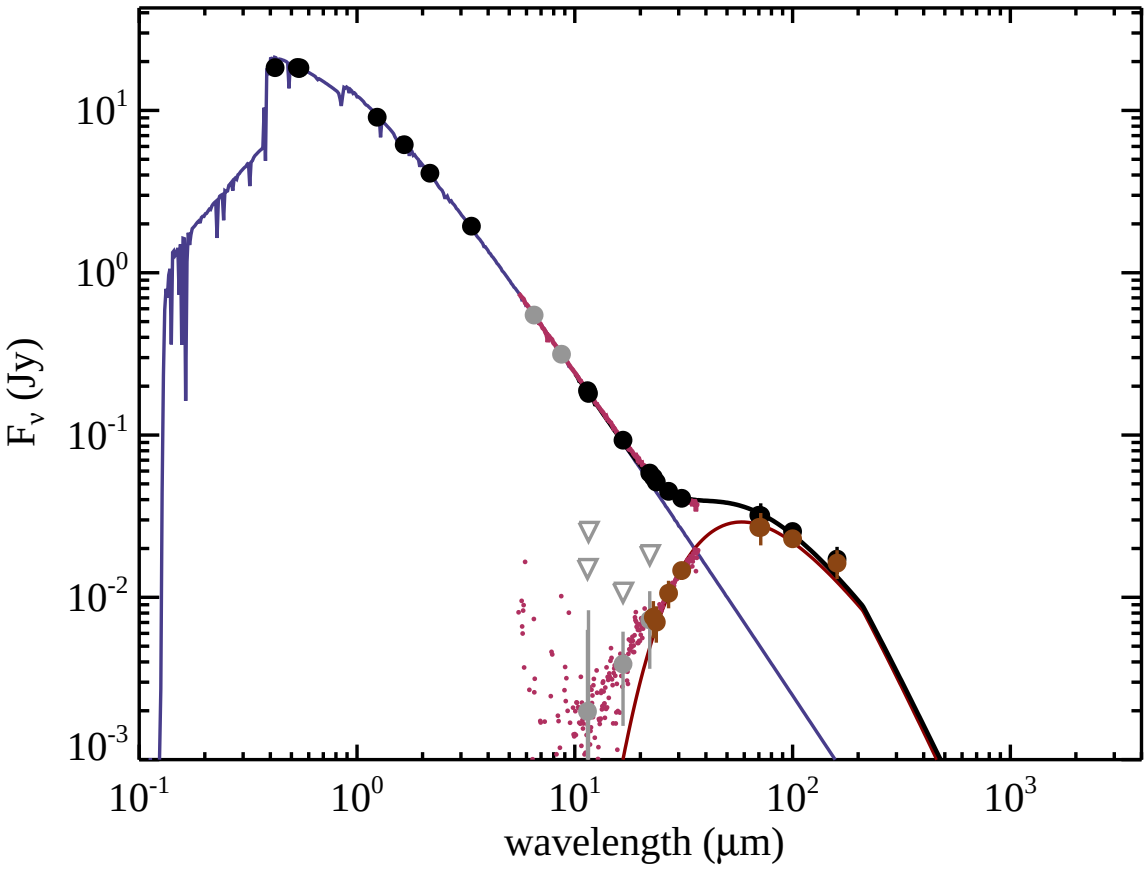

Figure 3.6 SED of HD 183324. The blackbody fit of the excess emission is for a temperature of 87 K and an effective radius of 40 AU. The blue line is the model stellar spectrum, the brown line is the disk blackbody SED, and the black line is the star+disk SED. Measured fluxes are in black dots, disk-only fluxes are in brown, and residual stellar fluxes are in grey. Spitzer IRS spectra are in purple. Inverted triangles are upper limits.

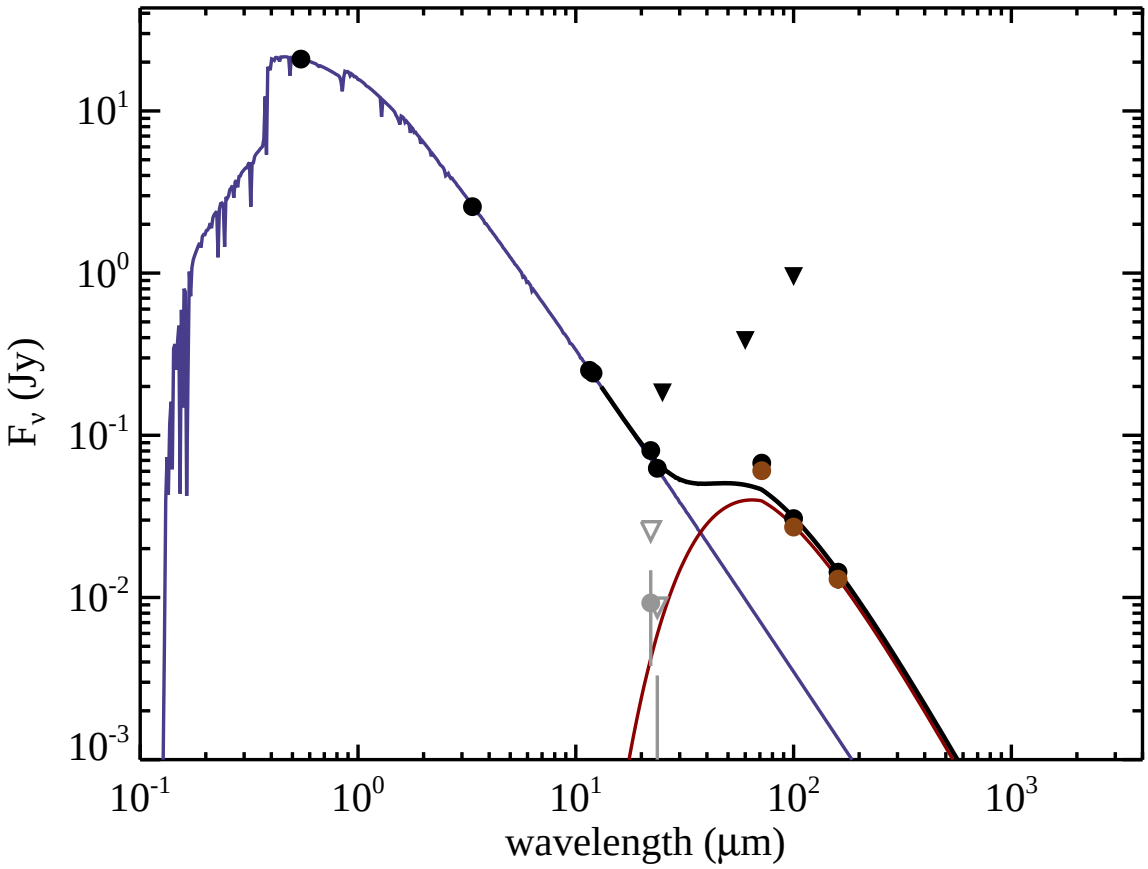

Figure 3.7 SED of HD 198160. The blackbody fit of the excess emission is for a temperature of 79 K and an effective radius of 41 AU. The blue line is the model stellar spectrum, the brown line is the disk blackbody SED, and the black line is the star+disk SED. Measured fluxes are in black dots, disk-only fluxes are in brown, and residual stellar fluxes are in grey. Inverted triangles are upper limits.

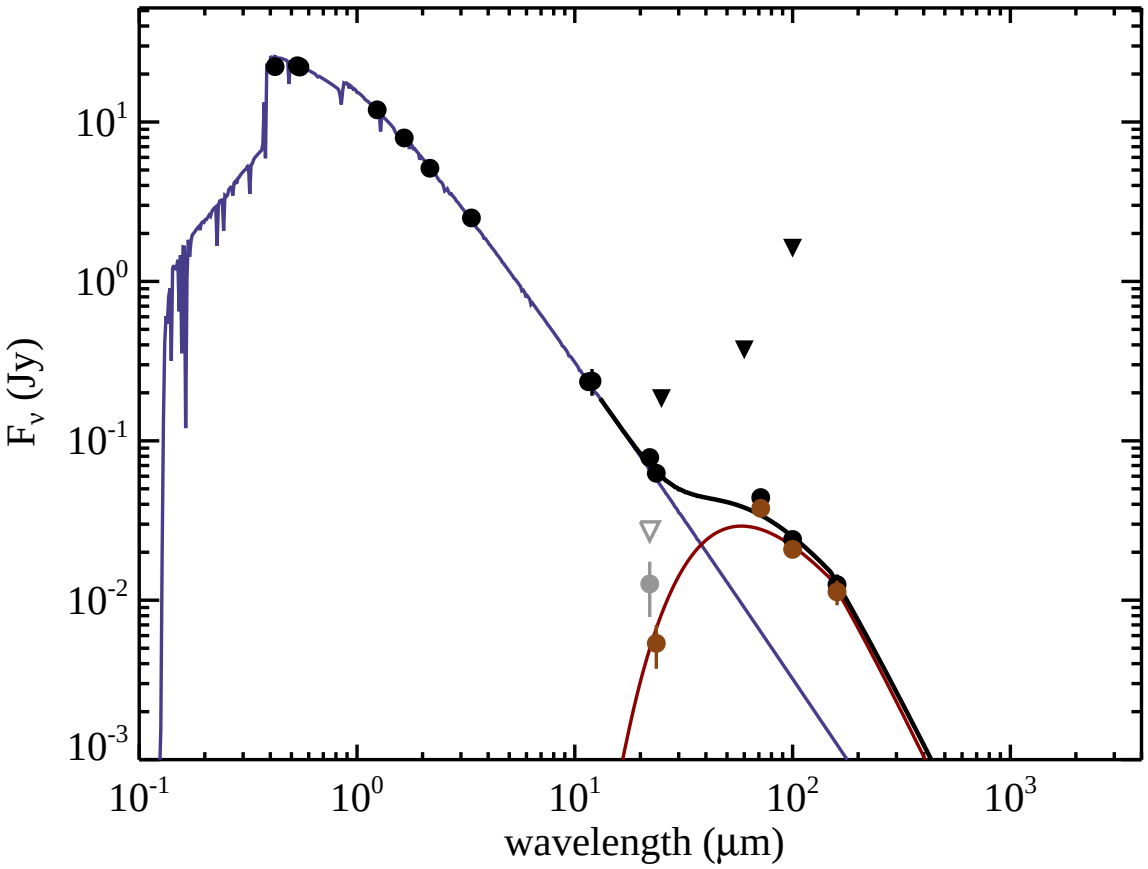

Figure 3.8 SED of HD 221756. The blackbody fit of the excess emission is for a temperature of 88 K and an effective radius of 57 AU. The blue line is the model stellar spectrum, the brown line is the disk blackbody SED, and the black line is the star+disk SED. Measured fluxes are in black dots, disk-only fluxes are in brown, and residual stellar fluxes are in grey. Inverted triangles are upper limits.

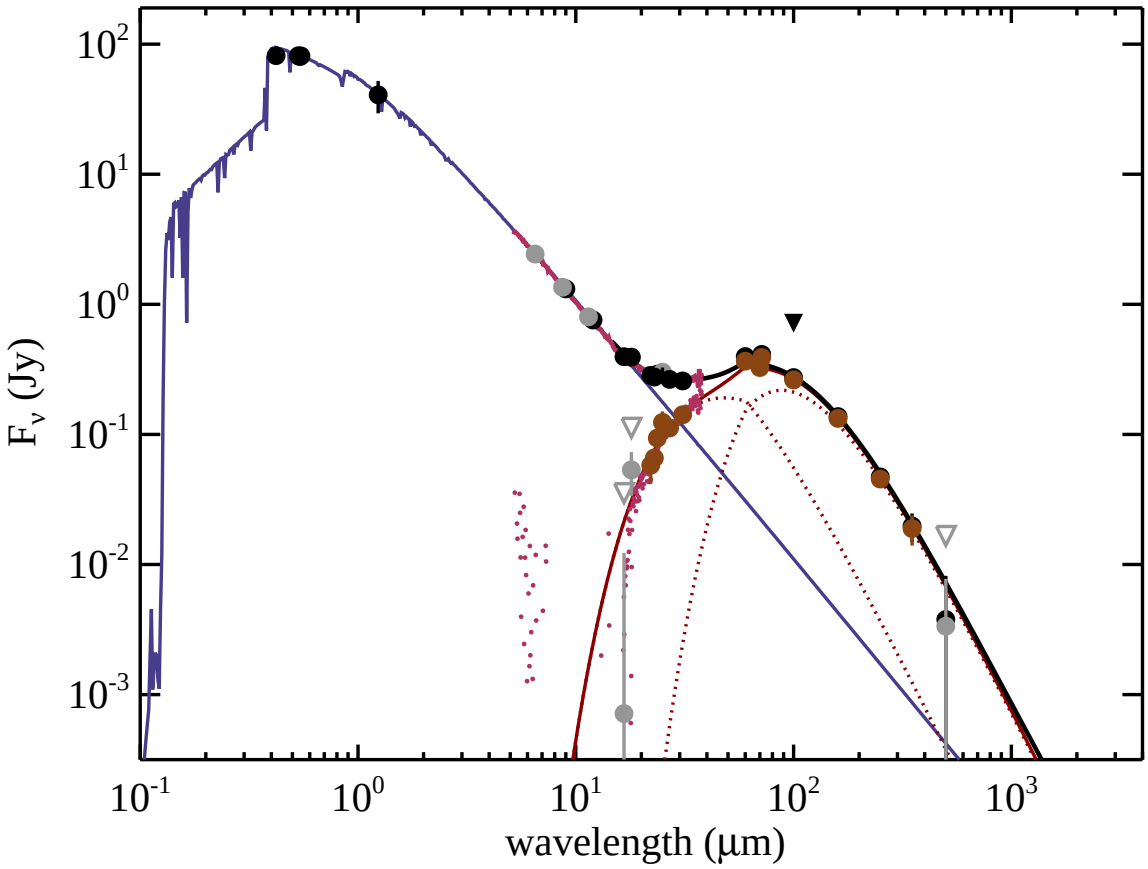

Figure 3.9 SED of HD 125162 (or λ Boo). The blackbody fit of the excess emission is for a temperature of 37 K and an effective radius of 235 AU. A warm component SED was also fit for a temperature of 106 K and an effective disk radius of 28 AU. The blue line is the model stellar spectrum, the brown line is the disk blackbody SED, and the black line is the star+disk SED. Measured fluxes are in black dots, disk-only fluxes are in brown, and residual stellar fluxes are in grey. Spitzer IRS spectra are in purple. Inverted triangles are upper limits.

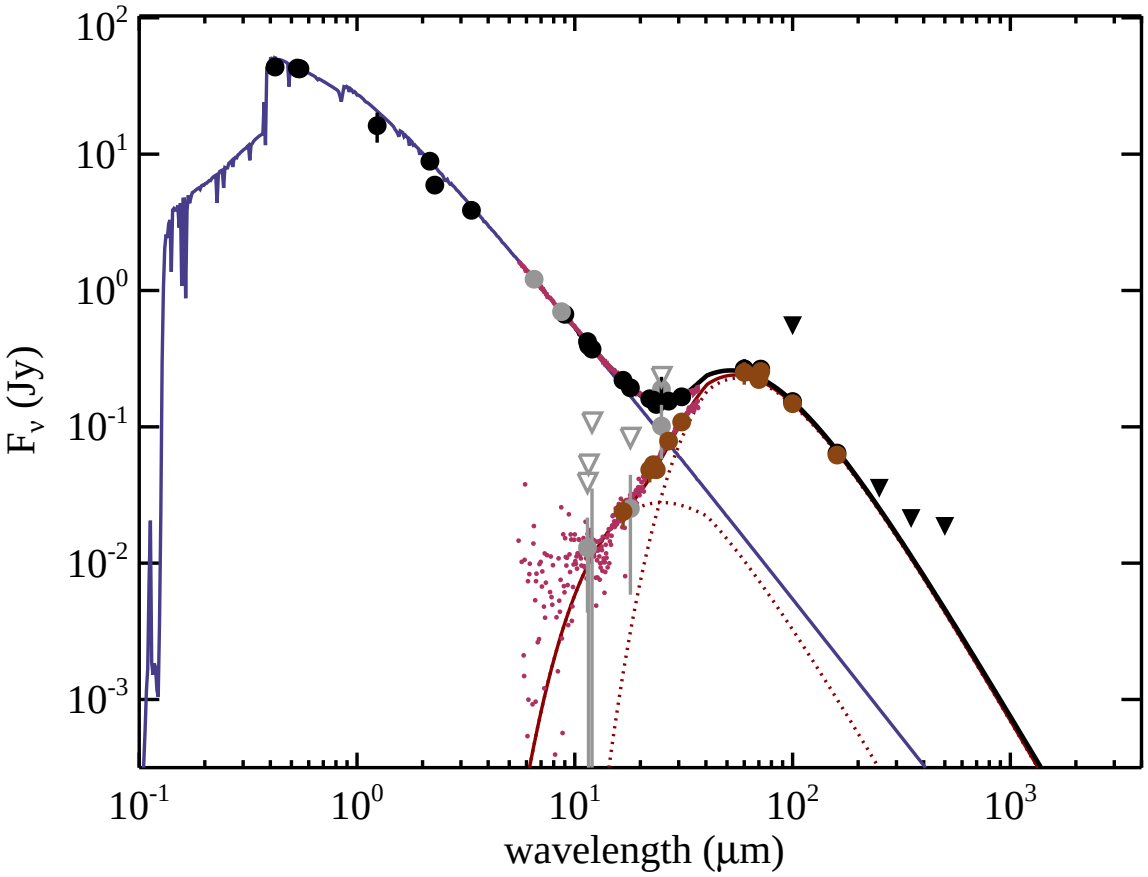

Figure 3.10 SED of HD 110411 (or ρ Vir). The blackbody fit of the excess emission is for a temperature of 68 K and an effective radius of 60 AU. A warm component SED was also fit for a temperature of 203 K and an effective disk radius of 7 AU. The blue line is the model stellar spectrum, the brown line is the disk blackbody SED, and the black line is the star+disk SED. Measured fluxes are in black dots, disk-only fluxes are in brown, and residual stellar fluxes are in grey. Spitzer IRS spectra are in purple. Inverted triangles are upper limits.

Table 3.3. Table of Stellar Parameters from SED Fit

Star (HD)	L_* ($L_\odot$)	T_{eff} (K)	M_* ($M_\odot$)
11413	20.5 ± 0.34	7818 ± 38	1.82
30422	8.72 ± 0.17	7948 ± 54	1.88
31295	14.7 ± 0.47	8666 ± 95	2.29
188324	15.7 ± 0.28	8605 ± 53	2.25
198160	23†	7905 ± 98	2.4†
221756	32.2 ± 0.60	8391 ± 46	2.11
125162	17.1 ± 0.31	8606 ± 52	2.25
110411	13.2 ± 0.25	8835 ± 58	2.41

†HD198160 has an indeterminate luminosity and mass because of the combined luminosity of the binary pair of stars.

Note. — Stellar properties of Lambda Boo stars. The stellar luminosity and mass are in solar units. The effective temperature is in Kelvin.

Based on these SED fits the basic parameters of the star and disk can be derived. The fluxes in the optical wavelength range fit the star's model SED; in combination with a known parallax the stellar properties seen in Table 3.3 can derive total luminoscity from apparent flux. If we assume the dust emits as a blackbody in a uniform toroidal ring then the equilibrium temperature of the disk will scale with disk radius and stellar luminosity. Using Equation 3.4, where T is the excess blackbody temperature in Kelvin and L_* is in solar luminosity, gives R_{disk} in AU (Wyatt, 2008).

$$R_{disk} = \frac{278.3}{T^2}\sqrt{L_*} \tag{3.4}$$

Disk parameters calculated from the SED are listed in Table 3.4.

Table 3.4. Table of Disk Parameters from SED Fit

Star	"Warm" Component			"Cold" Component		
(HD)	T_{disk} (K)	f ($\times 10^{-5}$)	R_{disk} (AU)	T_{disk} (K)	f ($\times 10^{-5}$)	R_{disk} (AU)
11413	···	···	···	55 ± 2	2.42 ± 0.33	118 ± 10
30422	···	···	···	75 ± 1	4.51 ± 0.47	41 ± 2
31295	182 ± 42	1.55 ± 1.61	9 ± 4	63 ± 3	6.09 ± 0.70	74 ± 6
188324	···	···	···	87 ± 2	1.79 ± 0.13	40 ± 2
198160	···	···	···	79 ± 6	1.98 ± 0.63	41 ± 6
221756	···	···	···	88 ± 4	1.50 ± 0.16	57 ± 5
125162	106 ± 6	2.95 ± 1.05	28 ± 3	37 ± 5	1.42 ± 1.21	235 ± 67
110411	203 ± 70	1.61 ± 0.28	7 ± 5	68 ± 13	4.77 ± 0.56	60 ± 22

Note. — Inferred disk temperatures from the modified blackbody fit (Eq. 3.3). The fractional luminosity of the excess emission is given as *f*. In the cases where two fits were required the "cold" component is utilized as it typically has the higher fractional luminosity (and therefore mass) in the system. The radius of the disk is in AU and is calculated from Equation 3.4. These distance measurements are approximations averaged over composition and dust grain size and scaled based on the temperature of the excess.

3.3 Bow Shock Models

When a star passes through a pocket of ISM dust it creates a bowshock in the direction of its relative motion. Martínez-Galarza et al. (2009) developed the following model (described by Equations 3.5 and 3.6) for an ISM shock front based on the required physics. The average distance the shock front is from the star (r_{ave}(a)) is a function of the ratio of solar radiation pressure pushing the dust outward relative to the gravitational force pulling it in (β(a)). The parameters of the star such as mass (M_*) and luminosity (L_*) relative to solar can be well determined by SED fits. Modest assumptions about the dust grains such as size (a) in μm, density (ρ) in g/cm^{-3}, and absorption efficiency (Q_{ave}) determine how effective the radiation pressure is. It also follows that the bow shock size is proportional to the inverse square of the relative velocity, such that a fast moving star will compress a shock front closer to the star itself. In order to determine the distance of a bowshock from a star, and in turn its angular separation and temperature, we first must constrain its relative velocity, v_{rel} (Martínez-Galarza et al., 2009; Artymowicz & Clampin, 1997):

$$r_{ave}(a) = \frac{2(\beta(a) - 1)\ M_*\ G}{v_{rel}^2} \tag{3.5}$$

$$\beta(a) = 0.57\ Q_{ave}(a)\ \frac{L_*}{M_*}\ a^{-1}\ \rho^{-1} \tag{3.6}$$

Since all of our target stars are within 100 pc, *Hipparcos* measurements of proper motions have been determined (van Leeuwen, 2007). Radial velocities along the line of sight have also been measured from offsets in spectroscopic line measurements (Gontcharov, 2006). The measurements are compiled in Table 3.5. Using these velocities, the actual motion of the star within the Galaxy can be measured using a matrix transformation knowing the location of the Galactic centre and the projected velocities relative to earth (Johnson & Soderblom, 1987). U, V, and W are all positive towards Galactic centre, mean Galactic rotation, and North Galactic pole, respectively. The effect of the observer's motion is removed by subtracting the local sidereal velocity. The final relative velocities are calculated in Table 3.6.

Since the ISM cloud itself can also have velocity relative to the star, we add in quadrature an additional velocity term of 7 km/s as an estimate of the actual cloud

Table 3.5. Table of Observed Stellar Velocities

Star(HD)	RA(°)	Dec(°)	μ_{ra}(mas/yr)	μ_{dec}(mas/yr)	v_{rad}(km/s)	Parallax(″)
11413	27.7268	-50.2061	-48.27 ± 0.24	-4.42 ± 0.30	3.0 ± 0.7	12.96 ± 0.30
30422	71.6073	-28.0874	-3.82 ± 0.23	17.58 ± 0.33	14.4 ± 1.0	17.80 ± 0.33
31295	73.7239	10.1508	41.49 ± 0.26	-128.73 ± 0.16	11.1 ± 1.2	28.04 ± 0.25
183324	292.2541	1.9504	-1.01 ± 0.35	-32.83 ± 0.22	12.0 ± 4.3	16.34 ± 0.36
198160	312.9105	-62.4293	83.74 ± 0.45	-46.35 ± 0.59	-16.0 ± 7.4	13.10 ± 0.64
221756	353.6564	40.2364	-17.14 ± 0.17	-46.69 ± 0.15	13.1 ± 0.6	12.45 ± 0.26

Note. — Right ascension and declination are in the J2000 epoch. μ_{ra} and μ_{dec} are the proper motions of RA and Dec in milliarcseconds per year. Parallax is measured in arcseconds. All measurements were compiled utilizing SIMBAD for Hipparcos and radial velocity data. (van Leeuwen, 2007; Gontcharov, 2006)

Table 3.6. Table of Galactic Stellar Velocities

Star(HD)	U	V	W	v_{gal}	v_{rel}
11413	-23.01 ± 0.03	22.05 ± 0.27	0.35 ± 0.22	31.78 ± 0.30	32.6
30422	2.61 ± 0.27	8.05 ± 0.06	-2.38 ± 0.68	8.79 ± 0.74	11.2
31295	-3.97 ± 1.23	-9.62 ± 0.07	-3.33 ± 0.14	10.93 ± 1.24	13.0
183324	-22.72 ± 10.98	13.87 ± 2.70	0.80 ± 4.82	26.63 ± 12.30	27.5
198160	27.26 ± 27.92	5.21 ± 21.97	-3.98 ± 4.94	28.04 ± 35.87	28.9
221756	-24.93 ± 0.07	0.25 ± 0.26	-2.89 ± 0.03	25.09 ± 0.28	26.05

Note. — The Galactic velocities for the target stars measured by proper motions and line-of-sight velocities. All velocities are in km/s. The heliocentric speed through the Galaxy is given by v_{gal}. The average relative velocity with a cloud is given as v_{rel}, assuming local ISM clouds travel ∼7 km/s (Artymowicz & Clampin, 1997). It can be seen that in most cases the measurement uncertainty of the stellar motion is much less then the systematic error in estimating the ISM cloud's velocity of ±7 km/s.

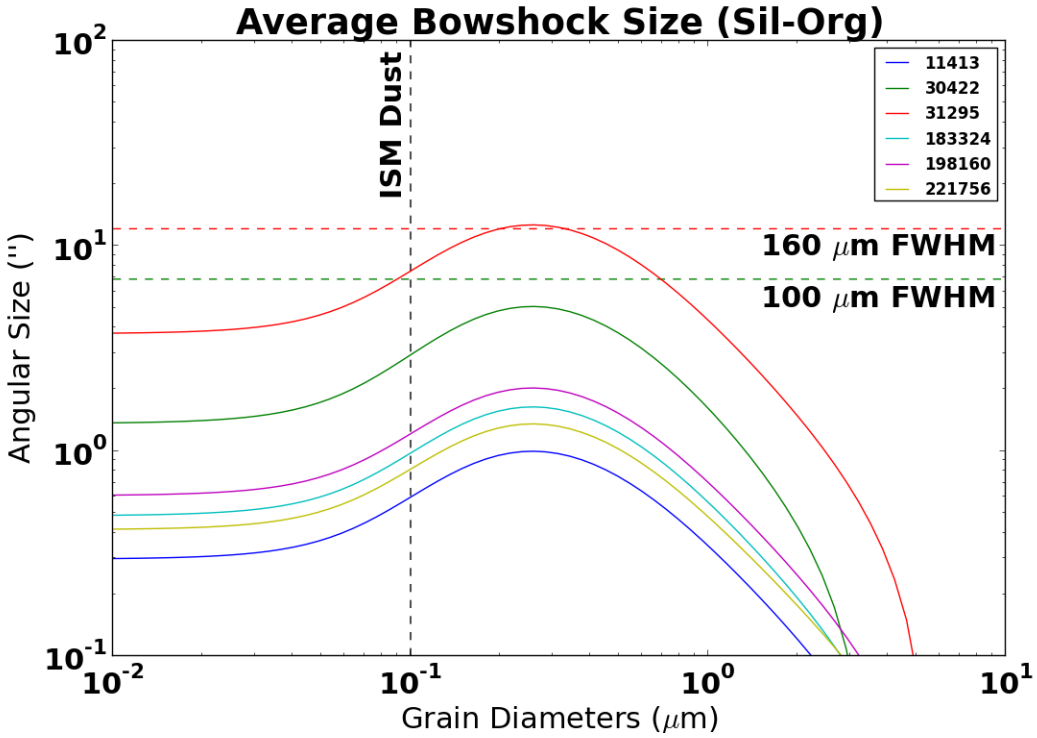

Figure 3.11 The angular size of a bow shock as a function of dust grain size given a silicate-organic composition. Typical ISM dust grain size is marked with a vertical line. The FWHM of Herschel PACS at 100 and 160 μm are shown for reference as horizontal lines.

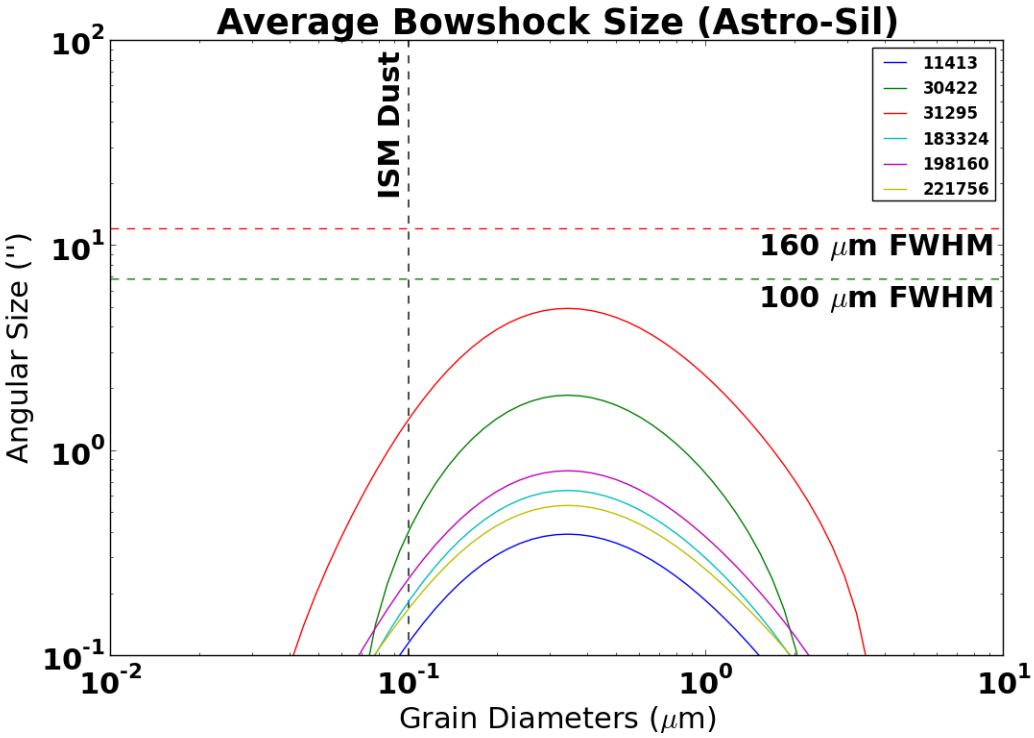

Figure 3.12 The angular size of a bow shock as a function of dust grain size given an astro-silicate composition. Typical ISM dust grain size is marked with a vertical line. The FWHM of Herschel PACS at 100 and 160 μm are shown for reference as horizontal lines.

to star relative velocity Artymowicz & Clampin (1997). In some cases this could be as much as ± 7 km/s but would require precise alignment of the two velocity vectors which is unlikely. In most cases the stellar velocity is much higher then the ISM velocity and only modestly affects the cloud-star relative velocity. By assuming ρ is 3.3 $g\ cm^{-3}$ (typical of the ISM) and the mass and luminosity from the SED fits, β can be calculated as a function of grain size, giving the average bow shock distance from the star via Equation 3.5. This distance is divided by the distance to the star to get the angular size and is compared with the PSF FWHM of *Herschel* PACS in Figure 3.11 and 3.12. Since the absorption efficiency (Q_{ave}) can vary based on grain composition, both organic silicates and astrosilicates are tested.

It can be seen in Figure 3.12 that the only system which could have a resolved image of a bowshock would be HD31295. This stands to reason as it is the closest of the 6 target stars and angular resolution is largely a function of distance to the star. Since the star is well resolved to have symmetric features at both 100 and 160 μm, we can say that HD31295 is in fact not interacting with an ISM dust cloud. The observed features are inconsistent with a bowshock as we would resolve an asymmetry (See Figures 3.1 and 3.2). For the other stars, *Herschel* cannot resolve a bow shock feature. This problem is even worse considering a pure astrosilicate composition such that the bowshock will be 10-25 AU around the star (Figure 3.11). This however does discredit an ISM bowshock of pure astrosilicates because the temperature of the dust would be ∼150-200 K at the modeled r_{ave}, which is outside the measured SED temperatures of 50-90 K (See Figure 3.14). However, while HD31295, HD125162, and HD110411 are fit with a double black body that shows there is dust emission over a range of temperature, we interpret those as inner debris disks (See Figures 3.5, 3.9, and 3.10). These systems are also the best resolved and would therefore exhibit asymmetric structure if they were from bowshocks, which they do not. Furthermore, Martínez-Galarza et al (2009) calculate the outer radius of the ISM nebula heated by the shock where diffuse emission could be observed. For 4 out of 6 of these stars the values calculated were ∼1500 AU from the star. We can constrain the diffuse emission outside 150 AU down to a few mJy noise limit. Therefore it is again unlikely that the emission is associated with an ISM bowshock.

3.4 ISM vs Debris Disk Dust

By combining the derived temperatures and spatial scale it is in principle possible to distinguish between the two models of an ISM bowshock and a debris disk. The typical dust grains of the ISM are of order 0.1 microns while debris disks are typically $\sim$ 10 microns in size. This variation in size is due to ISM dust stemming from stellar winds and supernova, while debris disk dust comes from collisional cascade of planetismals. Since the blowout size of dust grains is in the order of a few microns around A-stars, grains smaller then this will be ejected from the system on hyperbolic orbits leaving behind larger grains (Kirchschlager & Wolf, 2013). The processing of dust in the protostellar disk will lead to removal or coagulation of small grains into larger grains. In meteorite samples, pre-solar grains are typically less then a micron, but larger grains of a few microns can still be found (Davis, 2011). The isotopic ratios of these pre-solar grains are what indicate their origin from AGB stars which eject dust into the ISM. The variation in grain size leads to a change in the equilibrium temperature of dust at a given radius from the star. Small dust grains will have a higher temperature compared to larger dust grains at a set distance from the star. The temperature of a dust gain of size, s, at a radius from the star, r, is given below (Wyatt et al., 1999):

$$T(s,r) = \frac{<Q_{abs}>_{T_*}}{<Q_{abs}>_{T(s,r)}} T_{bb} \tag{3.7}$$

$$T_{bb} = \frac{278.3}{\sqrt{r}} L_*^{0.25} \tag{3.8}$$

$<Q_{abs}>$ is the absorption efficiency averaged over either the stellar spectrum (denoted with T_*) or the blackbody spectrum at a given dust temperature (denoted with $T(s,r)$). Since $T(s,r)$ is on both sides of the equation it requires iterative solving to converge the temperature on either side. Solving $T(s,r)$ for both 0.1 and 10 μm around each star and plotting as a function of radius allows comparison with the measurements of the temperatures and outer radial extent of the emission. As can be seen in Figures 3.13 and 3.14, the temperature-distance curves for each star for small dust grains are outside the observed temperatures and radii, while larger grains cross through the region constrained by the measurements of the excess emission. Since *Herschel* PACS data has higher resolution at 100 μm and has less contamination from background sources, we use those radii measurements to constrain the excess

emission. In Figure 3.13, a mixture of organic silicates was used as the composition for determining the absorption effeciencies, which is typical of debris disks (Augereau et al., 1999). In Figure 3.14, a mixture of astrosilicates typical of the ISM was used (Draine & Lee, 1984). However, Martínez-Galarza use a 50/50 mix of those compositions to model the bowshock emission in λ Boo stars (Martínez-Galarza et al., 2009). Therefore, if that composition was used the same temperature-distance curves would lie between the two extreme cases. We therefore conclude that the excess emission from the stars stems from debris disks rather than bowshocks with an ISM pocket.

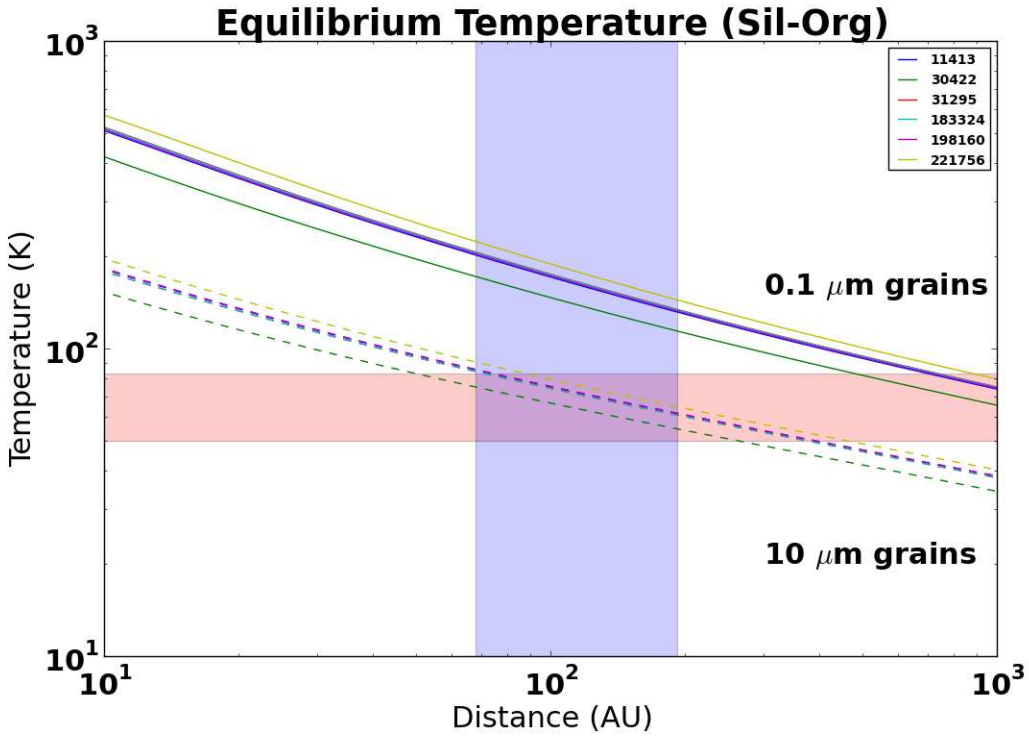

Figure 3.13 Plots of Equation 3.7 for 10 μm grains (dotted) and 0.1 μm (solid) typical of a mean dust grain size for a debris disk and ISM, respectively. A dust composition of silcate-organics is used in calculating the absorption efficiency. In red is the temperature range based on the SED fits from Table 3.4. In blue is the outer radial extent of the emission from Table 3.1 from 68-172 AU. Error bars have been included on the total range, but excluding systems which are at the PACS resolution limit. ISM size grains are well outside constraints provided by observations while the debris disk dust is well matched.

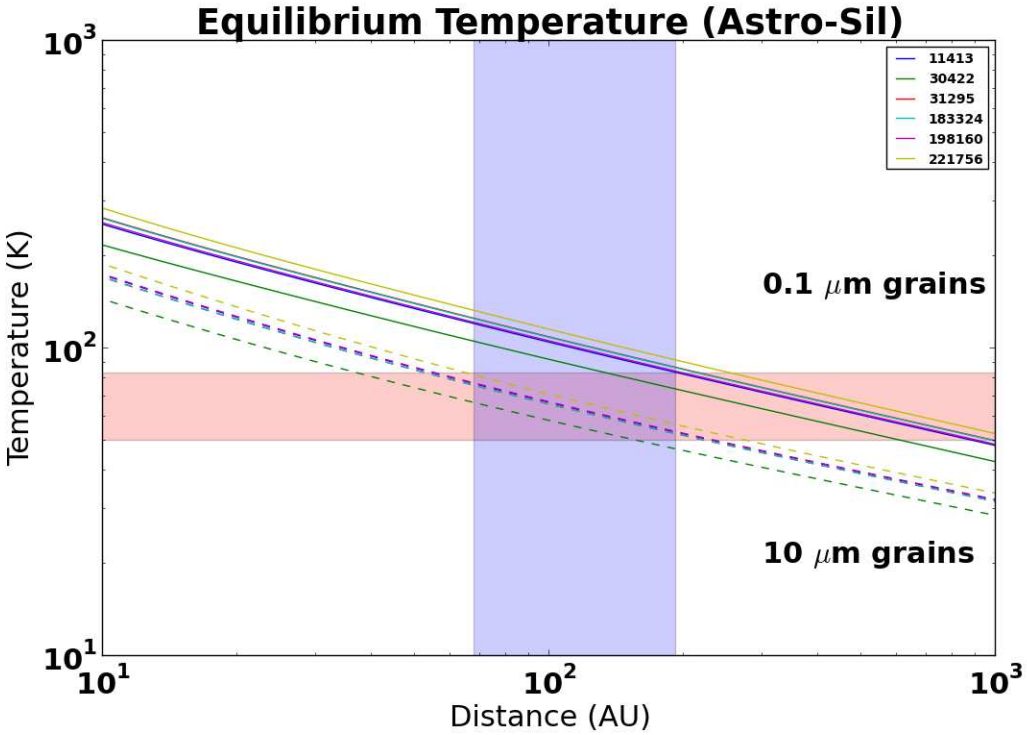

Figure 3.14 Plots of Equation 3.7 for 10 μm grains (dotted) and 0.1 μm (solid) typical of a mean dust grain size for a debris disk and ISM, respectively. A dust composition of astrosilicates is used in calculating the absorption efficiency. In red is the temperature range based on the SED fits from Table 3.4. In blue is the outer radial extent of the emission from Table 3.1. 0.1 μm grains of astrosilicate composition are relatively more plausible compared to the organic silicates in Figure 3.13, but still fall outside the measured constraints. Again debris disk size dust falls within the accepted values regardless of composition.

3.5 Can PR-drag Explain Secondary Accretion?

Poynting-Robertson-drag is the mechanism by which dust grains lose momentum and therefore spiral in towards the star. When dust is preferentially being irradiated in the direction of motion, due to its orbital path, it imparts a "drag" force causing momentum loss from incident photons. Van Lieshout et al (2014) worked out several analytic approximations for the accretion rate of dust due to PR-drag into the inner solar system by a collisionally active debris disk. In general, the model is ideal for explaining the differentiated accretion needed to explain the λ Boo phenomenon. Dust is accreted from a debris disk acting as a reservoir of dust. The dust enters the inner stellar system as large grains where it begins to sublimate volatile elements into gas, which is accreted onto the star. The dust grains then decrease in size as they sublimate their volatile mass. The smaller, metal rich dust grains are then more susceptible to radiation pressure and are blown out of the system (See Figure 3.15). The maximum accretion rate in units of $M_{\oplus}$/yr of large dust grains down to a radius (r) of zero is as follows:

$$max[\dot{M}_{PR}(r=0)] = 5.6 \times 10^{-13} * \frac{\sqrt{M_*}\, L_*}{\sqrt{R_{disk}}}\, Q_{pr}\, \frac{\beta}{0.5} \tag{3.9}$$

Q_{pr} is the radiation pressure efficiency on the dust and β is the ratio of radiation pressure to gravity. These are fundamental properties of the grain which vary with dust grain size and composition. However, we will assume that we want the maximum possible accretion rate. We therefore set $\beta = 0.5$ (as a numerically maximum possible value for bound grains) and $Q_{pr} = 2$ (as it can be physically confined between 0 to 2) van Lieshout et al. (2014). This simplifies the equation to stellar and disk parameters which have been measured for our target stars.

$$\dot{M}_{max} = 1.12 \times 10^{-12} * \frac{\sqrt{M_*}\, L_*}{\sqrt{R_{disk}}} \tag{3.10}$$

Based on the measurements from Table 3.3 and 3.4, the maximum accretion rate of dust are compiled in Table 3.7. They lie in the range of $2 - 10 \times 10^{-12}$ $M_{\oplus}$/yr. Gas-to-dust ratios of comets in our solar system range from 0.1 to 1 (Singh et al., 1992). Again for the maximum realistic accretion rate, these accretion estimates are reduced by a factor of 2 for the accretion rate of just volatile gas, assuming the sublimation timescale is negligible. Based upon gas accretion models, accretion rates below 0.33 $M_{\oplus}$/yr prevent dust from being entrained in the gas, which allows for the

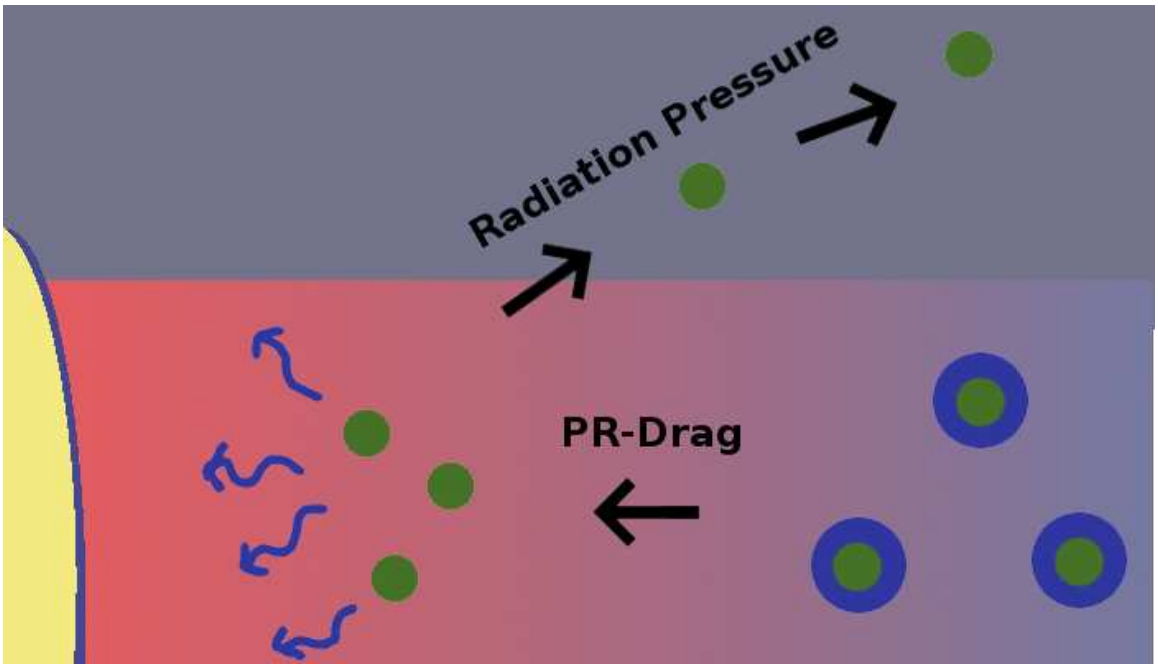

Figure 3.15 A cartoon depicting a model for secondary accretion via a debris disk. Large grains with volatile elements C, N, O, and S are frozen out on metal rich grains. When PR-Drag brings them into the inner solar system, they sublimate the volatile ices. The gas accretes onto the star while the now smaller dust grains experience a higher radiation pressure relative to gravity ($\beta > 0.5$) and are blown out on hyperbolic orbits.

Table 3.7. Maximum Accretion Rates Due to PR-drag

Star (HD)	$\dot{M}_{max}$ ($\times 10^{-12}$ $\frac{M_\oplus}{\mathrm{yr}}$)
11413	3.0
30422	2.2
31295	8.8
188324	4.3
198160	N/A
221756	7.2
125162	5.6
110411	9.0

Note. — The maximum accretion rates due to PR-drag in each system based on stellar and disk measurements of Table 3.3 and 3.4 using Equation 3.10. HD198160 is a binary star and therefore has radiation effects from both stars which are not adequately approximated in this model.

differentiation of metals in the inner AU of the system consistent with the atmosphere (Waters et al., 1992). Furthermore, collisions will often create eccentric orbit dust which will accrete and thus not allow for the species differentiation with sublimation temperature. The minimum radius for dust to circularize in a disk is proportional to the square root of luminosity (van Lieshout et al., 2014). For our target stars this is around 2 AU and is therefore well inside of where the debris disks are located.

Based upon stellar atmospheric models, the estimated mass of gas required on the surface of a λ Boo star is 0.33 $M_\oplus$ (Waters et al., 1992; Turcotte, 2002a,b). A simple inversion of the maximal accretion rate of 10×10^{-12} $M_\oplus$/yr, shows that it will take 33 Gyr for that amount of gas mass to accumulate on the surface. Given the age of the universe is about $\sim$ 13 Gyr, this accretion model as a mechanism of accretion for λ Boo stars is in fact impossible. Given that the age of a main sequence A star is $\sim$2 Gyr, the minimum accretion rate for that amount of mass would need to be

$\sim 10^{-9} M_{\oplus}$/yr for the phenomenon to occur at some point within the stars' lifetimes. Again this is also based on the assumption that there is no dissipation effects on the surface when in fact there are (i.e. meridional circulation). The minimum plausible estimate is 2 orders of magnitude higher then the estimated accretion rates for these stars given the PR model.

This PR-drag mechanism would be universal to debris disks and may explain why not all debris disk hosting stars are λ Boo stars. Therefore, some other rare accretion mechanism must play a role in causing the abundance anomaly, if the phenomenon is indeed caused by an external mechanism.

Chapter 4

Conclusions

The overall results of this thesis lies primarily in laying the ground work for further study. The full impact of the analysis won't be known until GPI observations have been taken and causal investigations into the λ Boo phenomenon can be done. Yet, a firm understanding of the fundamental observations made starting from the detector, whether on GPI or *Herschel*, is crucial to pursuing and achieving a scientific impact.

4.1 GPI Data Reduction

Through the analysis of the polarization spots on GPI flat field data, it was found that the diversity of the spots and distortions within the FOV require more thorough analysis to achieve the maximum contrast. Reducing systematic errors and not relying on basic assumptions about uniformity will improve the GPI data cubes, increase its precision, and in turn the discovery parameter space for debris disks and planets. Ultimately, the polarization spots were not a viable option to generate a reference library of PSFs to do a more thorough extraction. This led to the work by Ingraham et al. (2014) to use the Anderson and King method from *HST* WFC2 to generate high resolution PSFs. Furthermore, generating accurate calibration files of the spots was necessary for FOV effects to get subpixel accuracy for knowing where to apply the extraction algorithms (Wolff et al., 2014).

The extraction algorithmn using the least-square inversion method has thus far presented the most efficient extraction method for GPI data. The true performance improvement is yet to be known because metrics to measure the extraction efficiency

which are fair and applicable to both methods are presently under development. Furthermore, the method is limited by the quality of each of its parts. The high-resolution PSF model and the calibration files for the lenslet light locations on the detector are still being optimized. To date, there are only qualitative measures of improvement to the box-aperture method of the GPI pipeline described in Chapter 2.

The ability to solve the problem of GPI's flexure through data reduction of the science data itself does stand to have a sizable impact which can be quantified. The effectiveness of this is best seen in the context of the GPI exoplanet survey (GPIES) as a whole. Gemini Observatory has granted the GPI team 600 hours of observing time. The present paradigm to solve flexure is to take make a calibration file for each target at the beginning and end of observations and assume some basic model of image shift with time. This typically would take 6 minutes out of about an hour per target. This nominally means you would observe $\sim$ 600 targets. If you instead save 6 minutes per target you can save 3600 minutes throughout the whole survey from not having to waste time taking calibration files during the night. This is effectively 60 more hours or 60 more targets you could observe during the survey. In the long run, a small efficiency improvement such as this could have a big impact. One of the scientific questions GPIES is determining is the rate of detection for exoplanets, but if we say that 1/50 stars observed with GPI results in an imaged exoplanetary system then that efficiency increase will lead to the detection of another exoplanet/debris disk system.

4.2 *Herschel* Study of λ Boo Stars

Through the detailed analysis of the PACS images and careful analysis of the two competing models of external accretion, it can be seen that λ Boo stars are likely not caused by ISM accretion. The debate between the cause of photospheric excess may be answered as debris disk in origin, but the cause of the phenomenon is yet to be identified. The next step is to accept the paradigm of a debris disk as a causal relation to the stellar abundance anomaly and to try to ascertain how the accretion mechanism might function. This requires detailed modeling of the stellar surface to investigate if the required accretion rate is plausible for the debris disk we observe. It may also be true that the correlation to debris disk is not causal and may be a

coincident result of the phenomenon. Something to consider is that large impacts of planetary bodies could provide the volatile gases for accretion onto the star at a higher rate then PR-drag and the debris disk is a symptom of dynamical stirring coinciding with planetary migration. Furthermore, if λ Boo stars are a debris disk pheonomenon then why are not all debris disk stars λ Boo stars? This will have to be answered by a statistical, spectroscopic study of stars with and without debris disks to see if there are correlations. This work will be undertaken during my PhD thesis.

Bibliography

Anderson, J. & King, I. R. 2000, PASP, 112, 1360

Artymowicz, P. & Clampin, M. 1997, Astrophysical Journal, 490, 863

Augereau, J. C., Lagrange, A. M., Mouillet, D., Papaloizou, J. C. B., & Grorod, P. A. 1999, Astronomy and Astrophysics, 348, 557

Balog, Z. et al. 2014, Experimental Astronomy, 37, 129

Beichman, C. A. et al. 2006, Astrophysical Journal, 652, 1674

Booth, M. et al. 2013, Monthly Notices of the RAS, 428, 1263

Broekhoven-Fiene, H. 2012, PhD thesis, University of Victoria (Canada)

Castelli, F. & Kurucz, R. L. 2004, ArXiv Astrophysics e-prints

Chilcote, J. et al. 2014, ArXiv e-prints

Chilcote, J. K. et al. 2012, in Society of Photo-Optical Instrumentation Engineers (SPIE) Conference Series, Vol. 8446, Society of Photo-Optical Instrumentation Engineers (SPIE) Conference Series

Conover, W. J. W. J. 1980, Practical nonparametric statistics, Wiley series in probability and mathematical statistics (New York, Chichester: Wiley), previous edition: 1971

Cutri, R. M. et al. 2003, VizieR Online Data Catalog, 2246, 0

Davis, A. M. 2011, Proceedings of the National Academy of Science, 108, 19142

De Boer, K. & Seggewiss, W. 2008, Stars and Stellar Evolution (EDP Sciences)

Dent, W. R. F. et al. 2014, Science, 343, 1490

Dominik, C., Blum, J., Cuzzi, J. N., & Wurm, G. 2007, Protostars and Planets V, 783

Draine, B. T. & Lee, H. M. 1984, Astrophysical Journal, 285, 89

Faraggiana, R., Bonifacio, P., Caffau, E., Gerbaldi, M., & Nonino, M. 2004, Astronomy and Astrophysics, 425, 615

Fischer, D. A. & Valenti, J. 2005, Astrophysical Journal, 622, 1102

Gomes, R., Levison, H. F., Tsiganis, K., & Morbidelli, A. 2005, Nature, 435, 466

Gontcharov, G. A. 2006, Astronomy Letters, 32, 759

Greaves, J. S., Fischer, D. A., & Wyatt, M. C. 2006, Monthly Notices of the RAS, 366, 283

Griffin, R. E., Gray, R. O., & Corbally, C. J. 2012, A&A, 547, A8

Haisch, Jr., K. E., Lada, E. A., & Lada, C. J. 2001, Astrophysical Journal, Letters to the Editor, 553, L153

Hauck, B. & Mermilliod, M. 1998, Astronomy and Astrophysics, Supplement Series, 129, 431

Hernández, J. et al. 2007, Astrophysical Journal, 662, 1067

Hillenbrand, L. A. et al. 2008, Astrophysical Journal, 677, 630

Hughes, A. M., Wilner, D. J., Kamp, I., & Hogerheijde, M. R. 2008, Astrophysical Journal, 681, 626

Ingraham, P. J. et al. 2014a, in Society of Photo-Optical Instrumentation Engineers (SPIE) Conference Series, Vol. 9147, Society of Photo-Optical Instrumentation Engineers (SPIE) Conference Series

Ingraham, P. J., Ruffio, J.-B., Perrin, M. D., Wolff, S., Draper, Z., Maire, J., Marchis, F., & Fesquet, V. 2014b, in Society of Photo-Optical Instrumentation Engineers (SPIE) Conference Series, Vol. 9147, Society of Photo-Optical Instrumentation Engineers (SPIE) Conference Series

Ishihara, D. et al. 2010, Astronomy and Astrophysics, 514, A1

Jasinta, D. M. D., Raharto, M., & Soegiartini, E. 1999, Astronomy and Astrophysics, Supplement Series, 134, 87

Johnson, D. R. H. & Soderblom, D. R. 1987, Astronomical Journal, 93, 864

Kalas, P., Graham, J. R., & Clampin, M. 2005, Nature, 435, 1067

Kennedy, G. M. et al. 2012, Monthly Notices of the RAS, 421, 2264

Kirchschlager, F. & Wolf, S. 2013, Astronomy and Astrophysics, 552, A54

Lafrenière, D., Marois, C., Doyon, R., Nadeau, D., & Artigau, É. 2007, ApJ, 660, 770

Larkin, J. E. et al. 2014, in Society of Photo-Optical Instrumentation Engineers (SPIE) Conference Series, Vol. 9147, Society of Photo-Optical Instrumentation Engineers (SPIE) Conference Series

Lodders, K. 2003, Astrophysical Journal, 591, 1220

Macintosh, B. et al. 2014, Proceedings of the National Academy of Science, 111, 12661

Maire, J. et al. 2010, in Society of Photo-Optical Instrumentation Engineers (SPIE) Conference Series, Vol. 7735, Society of Photo-Optical Instrumentation Engineers (SPIE) Conference Series

Maldonado, J., Eiroa, C., Villaver, E., Montesinos, B., & Mora, A. 2012, Astronomy and Astrophysics, 541, A40

Marois, C., Correia, C., Galicher, R., Ingraham, P., Macintosh, B., Currie, T., & De Rosa, R. 2014, ArXiv e-prints

Marois, C., Lafrenière, D., Doyon, R., Macintosh, B., & Nadeau, D. 2006, Astrophysical Journal, 641, 556

Marois, C., Macintosh, B., & Véran, J.-P. 2010, in Society of Photo-Optical Instrumentation Engineers (SPIE) Conference Series, Vol. 7736, Society of Photo-Optical Instrumentation Engineers (SPIE) Conference Series

Marshall, J. P. et al. 2014, Astronomy and Astrophysics, 565, A15

Martínez-Galarza, J. R., Kamp, I., Su, K. Y. L., Gáspár, A., Rieke, G., & Mamajek, E. E. 2009, Astrophysical Journal, 694, 165

Matthews, B. C., Krivov, A. V., Wyatt, M. C., Bryden, G., & Eiroa, C. 2014, ArXiv e-prints

Michaud, G. & Charland, Y. 1986, Astrophysical Journal, 311, 326

Michaud, G., Tarasick, D., Charland, Y., & Pelletier, C. 1983, Astrophysical Journal, 269, 239

Moór, A. et al. 2011, Astrophysical Journal, Letters to the Editor, 740, L7

Nielsen, E. L. et al. 2013, Astrophysical Journal, 776, 4

Paunzen, E. 2004, in IAU Symposium, Vol. 224, The A-Star Puzzle, ed. J. Zverko, J. Ziznovsky, S. J. Adelman, & W. W. Weiss, 443–450

Paunzen, E., Iliev, I. K., Fossati, L., Heiter, U., & Weiss, W. W. 2014, Astronomy and Astrophysics, 567, A67

Paunzen, E., Kamp, I., Weiss, W. W., & Wiesemeyer, H. 2003, Astronomy and Astrophysics, 404, 579

Perrin, M. et al. 2014, in Society of Photo-Optical Instrumentation Engineers (SPIE) Conference Series, Vol. 9147, Society of Photo-Optical Instrumentation Engineers (SPIE) Conference Series

Perrin, M. D. et al. 2014, ArXiv e-prints

Raymond, S. N. et al. 2012, Astronomy and Astrophysics, 541, A11

Savransky, D., Thomas, S. J., Poyneer, L. A., & Macintosh, B. A. 2013, Applied Optics, 52, 3394

Singh, P. D., de Almeida, A. A., & Huebner, W. F. 1992, Astronomical Journal, 104, 848

Spiegel, D. S. & Burrows, A. 2012, Astrophysical Journal, 745, 174

Su, K. Y. L. et al. 2006, Astrophysical Journal, 653, 675

Turcotte, S. 2002a, Astrophysical Journal, Letters to the Editor, 573, L129

— 2002b, Astrophysical Journal, Letters to the Editor, 573, L129

van Leeuwen, F. 2007, Astronomy and Astrophysics, 474, 653

van Lieshout, R., Dominik, C., Kama, M., & Min, M. 2014, ArXiv e-prints

Venn, K. A. & Lambert, D. L. 1990, Astrophysical Journal, 363, 234

Vitense, C., Krivov, A. V., Kobayashi, H., & Löhne, T. 2012, Astronomy and Astrophysics, 540, A30

Waters, L. B. F. M., Trams, N. R., & Waelkens, C. 1992, Astronomy and Astrophysics, 262, L37

Wolff, S. G., Perrin, M. D., Maire, J., Ingraham, P. J., Rantakyro, F., & Hibbon, P. 2014, in Society of Photo-Optical Instrumentation Engineers (SPIE) Conference Series, Vol. 9147, Society of Photo-Optical Instrumentation Engineers (SPIE) Conference Series

Woosley, S. E. & Weaver, T. A. 1995, Astrophysical Journal, Supplement Series, 101, 181

Wright, E. L. et al. 2010, Astronomical Journal, 140, 1868

Wyatt, M. C. 2008, Annual Review of Astronomy and Astrophysics, 46, 339

Wyatt, M. C., Clarke, C. J., & Greaves, J. S. 2007a, Monthly Notices of the RAS, 380, 1737

Wyatt, M. C., Dermott, S. F., Telesco, C. M., Fisher, R. S., Grogan, K., Holmes, E. K., & Piña, R. K. 1999, Astrophysical Journal, 527, 918

Wyatt, M. C., Smith, R., Greaves, J. S., Beichman, C. A., Bryden, G., & Lisse, C. M. 2007b, Astrophysical Journal, 658, 569

Zuckerman, B. & Song, I. 2012, Astrophysical Journal, 758, 77